Evaluation of Mechanical Properties of Li_2S-P_2S_5-Based Glasses and Formation of Li Metal/Solid Electrolyte Interfaces in All-Solid-State Lithium Metal Batteries

Evaluation of Mechanical Properties of Li_2S-P_2S_5-Based Glasses and Formation of Li Metal/Solid Electrolyte Interfaces in All-Solid-State Lithium Metal Batteries

Atsutaka Kato

February 2018

Doctoral Thesis at Osaka Prefecture University

Evaluation of Mechanical Properties of Li_2S-P_2S_5-Based Glasses and Formation of Li Metal/Solid Electrolyte Interfaces in All-Solid-State Lithium Metal Batteries

Contents

1. General introduction

Rechargeable batteries are crucial in modern society for the wide range of applications such as consumer electronic devices. The applications of batteries have increased and the most attention has been paid to the development of smart grids and electric vehicles using rechargeable batteries [1–3]. With the growth of global industries, energy demand has increased remarkably. However, fossil fuels, which fulfill a large part of the energy consumption, will be exhausted in the near future. For creating a sustainable society, it is essential to replace the fossil fuels with renewable resources such as sunlight, wind, and geothermal heat. Rechargeable batteries are helpful to meet the electricity supply and demand generated from intermittent natural sources in smart grid systems [1]. Furthermore, the batteries charged by the natural energy can be used as power sources such as for electric vehicles, reducing the risk of global warming from CO_2 [4–6]. However, current commercial batteries do not satisfy the demands from these applications. The development of batteries with high energy density, long cycle life, and safety is urgently required.

Lithium-ion batteries are a good candidate to meet the demands because of the relatively high energy density, but current ones have some disadvantages. One is the safety issues. Organic liquid electrolytes in conventional lithium-ion batteries have a risk of fire at the time of thermal runaway caused by accidents such as overcharging or short-circuiting [7,8]. The risk is more serious for future large-scale applications for stationary energy storage in smart grids or electric vehicles. In addition, the energy density of general lithium-ion batteries with the configuration of C(graphite)/$LiCoO_2$ approaches the practical limit. An effective way toward solving the issues is to substitute inorganic solid electrolytes for organic liquid electrolytes [9,10]. All-solid-state batteries with non-flammable solid electrolytes enable us to reduce the safety risk [11–18]. Furthermore, they have a potential use of high voltage positive electrode materials [19–21], high capacity sulfur electrode [22–29], and Li metal negative electrode [13,15,17,18,29–46], which are promising candidates to construct high energy density batteries. As well as these advantages, solid electrolytes are superior to liquid electrolytes from several

points of view; high ion transportation number, simple reaction at electrode/electrolyte interface, wide electrochemical window, and high thermal stability [10–12,47]. A challenge for solid electrolytes is increasing ionic conductivities. Extensive researches have been done to develop solid electrolytes with high ionic conductivities.

Oxide-based solid electrolytes such as perovskite-type [48–50], NASICON-type [51,52] and garnet-type [53–57] ceramics have been reported to exhibit ambient temperature conductivities above 10^{-4} S cm^{-1}. However, oxide-based ceramic solid electrolytes require sintering process at high temperatures over 1000℃ to reduce the resistance at grain boundaries [48,58,59]. If solid electrolytes contact with electrode materials at such high temperature, undesirable side reactions will occur and generate large interfacial resistance between electrodes and electrolytes.

In contrast, sulfide-based solid electrolytes exhibit higher Li-ion conductivity compared with oxide-based ones due to higher polarizability of sulfide ions. Three types of sulfide-based solid electrolytes such as crystalline [13,35,47,60–65], glass and glass-ceramic materials [66–72] have been reported. Crystalline electrolytes such as $Li_{10}GeP_2S_{12}$ (LGPS) [62,73] and $Li_{9.54}Si_{1.74}P_{1.44}S_{11.7}Cl_{0.3}$ [47] have ionic conductivities of the order of 10^{-2} S cm^{-1} at ambient temperature, which are comparable to the conventional organic liquid electrolytes. The other crystalline electrolytes such as Li_6PS_5X (X= Cl, Br) [63–65] and $Li_7P_2S_8I$ [17] have also higher ionic conductivities than the order of 10^{-4} S cm^{-1}. Recently, new crystalline phases with high ionic conductivities have been explored by using theoretical calculations [74–76]. On the other hand, glass electrolytes are prepared by melt quenching or mechanical milling. The pelletized Li_2S-SiS_2 and Li_2S-P_2S_5 glasses prepared by pressing the glass powder at room temperature exhibit high conductivities over 10^{-4} S cm^{-1} [66]. The third components such as Li_xMO_y (Li_xMO_y = Li_4SiO_4, Li_3PO_4, Li_3BO_3 etc.) or lithium halides increase the conductivities to the order of 10^{-3} S cm^{-1} [14,66,70,77,78]. Glass-ceramic electrolytes are prepared by crystallization of the corresponding glasses at around their crystallization temperatures. The $70Li_2S \cdot 30P_2S_5$ (mol%) glass-ceramics exhibit much higher Li ion conductivities of the order of 10^{-2} S cm^{-1} than the glasses due to precipitation of highly conductive $Li_7P_3S_{11}$ crystal [69]. The other glass-

ceramic electrolytes such as $90(0.7Li_2S \cdot 0.3P_2S_5) \cdot 10LiBr$ [71] or $60Li_2S \cdot 25P_2S_5 \cdot 10Li_3N$ [72] with ionic conductivities of the order of 10^{-3} S cm^{-1} have also been reported.

With the progress of research about solid electrolytes with high ionic conductivities, the use of Li metal negative electrode is strongly desired for all-solid-state batteries in order to achieve high energy density batteries [79,80]. Li metal is the most attractive material as a negative electrode because of its extremely high theoretical capacity (3861 mAh g^{-1}) and its lowest negative electrochemical potential (-3.04 V vs. SHE). However, dendrite growth and low coulombic efficiency during charging and discharging are fatal problems for Li metal batteries using conventional organic liquid electrolytes [81–83]. Dendrite growth leads to short-circuiting, increasing the risk of fire. The use of inorganic solid electrolytes in Li metal batteries is effective to solve the problems [17,18,79,80]. Li metal batteries using solid electrolytes are divided into thin-film and bulk-type batteries. Thin-film batteries are prepared by accumulating solid electrolytes and electrode active materials on a substrate by RF magnetron sputtering or vacuum-evaporation [84]. These processes construct favorable interfaces between solid electrolytes and electrode active materials, including Li metal. Li metal batteries have achieved excellent cell performance in thin-film batteries. Thin-film batteries using lithium phosphorus oxynitride (LiPON) as solid electrolytes show long cycle life over 40,000 times without capacity fading because of their favorable interfaces [85]. However, energy storage in thin-film batteries is small because it is difficult to accumulate a large amount of electrode active materials by using sputtering and vacuum-evaporation processes. On the other hand, bulk-type batteries are prepared by stacking solid electrolyte powders and composite electrode powders of electrode active materials and solid electrolytes [68]. Metal foils in place of the composite electrodes are used as metal electrodes such as Li electrodes. The bulk-type battery is expected to have larger energy storage due to the addition of larger amounts of active materials to the cell. Table 1 shows areal capacities of bulk-type Li symmetric cells with sulfide and garnet-type solid electrolytes [13,30,33–36,86–103]. Unfortunately, present bulk-type cells using Li metal electrodes suffer from extremely low areal capacities of at most 1.5 mAh cm^{-2} because Li dendrites may grow upon cycling through pores, cracks, or grain boundaries in the solid

Table 1 Current densities, areal capacities, cycle number, and operating temperature of sulfide and garnet-type solid electrolytes

Electrolyte	Current density /mA cm^{-2}	Areal Capacity /mAh cm^{-2}	Cycle number	Temperature /°C	Refences
Li_3PS_4 glass	0.2	0.1	15	25	[86]
$80Li_2S·20P_2S_5$ glass-ceramic	0.064	0.19	5	25	[30]
$75Li_2S·24P_2S_5·1P_2O_5$ glass-ceramics	0.1	0.13	42	25	[87]
$60Li_2S·20P_2S_5·20LiI$ glass ceramics	0.1	0.1	75	25	[88]
β-Li_3PS_4	0.1	0.2	20	25	[13]
β-Li_3PS_4	0.1	0.2	20	80	[13]
β-Li_3PS_4	0.75	1.5	24	r.t.	[36]
$Li_7P_2S_8I$	0.2	0.2	800	r.t.	[35]
β-Li_3PS_4+$Li_7La_3Zr_2O_{12}$ composite	0.1	0.2	>100	25	[89]
β-Li_3PS_4+$Li_6ZnNb_4O_{14}$ composite	0.1	0.1	400	r.t.	[90]
$77.5Li_2S·22.5P_2S_5$ glass ceramics+polyimine composite	0.5	1	20	60	[91]
$Li_{3.334}Ge_{0.334}As_{0.666}S_4$+$LiBH_4$-LiI coating	0.1	0.1	10	25	[33]
$Li_{3.833}Sn_{0.833}As_{0.166}S_4$+$LiBH_4$-LiI coating	0.1	0.1	10	r.t.	[34]
$Li_7La_3Zr_2O_{12}$ (Al-substituted)	0.046	0.092	20	25	[92]
$Li_7La_3Zr_2O_{12}$ (Al-substituted)	0.049	0.098	5	25	[93]
$Li_7La_3Zr_2O_{12}$ (Al-substituted)	0.2	0.4	100	r.t.	[94]
$Li_7La_3Zr_2O_{12}$ (Ta-substituted)	0.1	0.41	10	25	[95]
$Li_7La_3Zr_2O_{12}$ (Ta-substituted)	0.1	0.3	12	60	[96]
$Li_7La_3Zr_2O_{12}$ (Ta-substituted)	0.3	0.15	5	25	[97]
$Li_7La_3Zr_2O_{12}$ (Ta-substituted)	0.5	0.25	5	25	[98]
$Li_7La_3Zr_2O_{12}$ (Ta-substituted)+Au coating	0.08	0.16	35	25	[99]
$Li_7La_3Zr_2O_{12}$ (Ta-substituted)+Au coating	0.25	0.5	35	50	[99]
$Li_7La_3Zr_2O_{12}$ (Nb,Ca-substituted)+Si coating	0.2	0.017	75	r.t.	[100]
$Li_7La_3Zr_2O_{12}$ (Nb,Ca-substituted)+Al coating	0.2	0.017	42	r.t.	[101]
$Li_7La_3Zr_2O_{12}$ (Nb,Ca-substituted)+Al_2O_3 coating	0.2	0.1	90	r.t.	[102]
$Li_7La_3Zr_2O_{12}$ (Nb,Ca-substituted)+ZnO coating	0.1	0.017	140	r.t.	[103]

electrolytes, inducing short circuits [32,80,104,105]. There are two key points for the application of Li metal to bulk-type all-solid-state batteries. One is the development of solid electrolytes from the viewpoint of mechanical properties. The other is the interface formation between Li metal and solid electrolytes.

Lithium-ion batteries with liquid electrolytes generally use the separators made of polyolefin polymers because of their oxidation and reduction resistance [106,107]. The separators must have porous structure in order to transport ions by impregnating liquid electrolytes, which is a possible pass for Li dendrites. As a solution to the problem, Kanamura *et al.* have reported that very stable Li dissolution/deposition cycles are obtained by using polyimide separators with a 3-dimentionally ordered microporous structure (3DOM) [108]. The uniform microporous structure of separators forms uniform current distribution, which prevents the formation of Li dendrites [109]. Polyimide separators also have high mechanical strength to maintain the microstructure. On the other hand, it is considered that dense and stiff solid electrolytes enough to physically block the dendrite growth can be used as separators for all-solid-state Li metal batteries. Three kinds of solid electrolyte separators have been mainly studied for all-solid-state Li metal batteries: polymer electrolytes, garnet-type oxide electrolytes, and sulfide electrolytes. Polymer electrolytes are so flexible that they are expected to accommodate volume change of Li metal during the dissolution/deposition reaction [81]. Many polymer electrolytes such as poly(ethylene oxide) (PEO) or PEO-based copolymers have been investigated [110–112]. However, conductivities of PEO-based electrolytes are not sufficient below 60°C. Thus, Li metal polymer batteries usually operate above 60°C, which leads to losing mechanical strength to prevent the growth of Li dendrites [113,114]. Garnet-type $Li_7La_3Zr_2O_{12}$ oxide electrolytes have high chemical stability against Li metal [115]. The elastic modulus is about 150 GPa [116]. It is inferred that garnet-type electrolytes are stiff enough to block the Li dendrites. Much attention has been paid to apply Li metal in all-solid-state batteries with garnet-type electrolytes. However, short circuit problems with the dendrite growth have not been solved. Most garnet-type electrolytes are polycrystalline ceramics. It has been reported that Li metal preferentially propagates through the grain boundaries and results in short-circuiting of

Li metal cells [104,105]. Sulfide electrolytes such as the Li_2S-P_2S_5 system are also tried to be used for all-solid-state Li metal batteries. In particular, it is considered that sulfide glass electrolytes are promising because they are much stiffer than polymer electrolytes and have much less grain boundaries unlike oxide ceramic electrolytes. However, few studies have focused on the mechanical properties of sulfide solid electrolytes; it is difficult to evaluate their mechanical properties because they are generally unstable in air. Recently, Sakuda *et al.* have succeeded in evaluating the elastic modulus and formability of highly Li-ion conducting Li_2S-P_2S_5 glass electrolytes. Li_2S-P_2S_5 glasses have a low Young's modulus (18-25 GPa) and excellent formability to be highly densified by pressing even at ambient temperature [117,118]. It is assumed that sulfide glass electrolytes with such a low elastic modulus can accommodate volume change of Li metal during Li dissolution/deposition reaction; thus such electrolytes can suppress the dendrite growth. The sulfide glass electrolytes with a lower elastic modulus may be more suitable. However, studies on mechanical properties of sulfide glass electrolytes are still insufficient. More extensive studies about the mechanical properties are required.

As the second key point, interface formation between Li metal and solid electrolytes is important to suppress the generation of Li dendrites. In the case of sulfide solid electrolytes, some reports show that interface modification improved electrochemical performance of all-solid-state Li cells [30,31]. Nagao *et al.* have reported that a uniform interface with a large contact area prepared by vacuum-evaporation of Li metal improves the reversibility of Li dissolution/deposition in bulk-type batteries [30]. In addition, it has been reported that interface modification by inserting indium thin films between Li metal and solid electrolytes is effective to reduce a risk of short-circuiting in $Li/Li_4Ti_5O_{12}$ cells [31]. On the other hand, some researchers have report that Li dissolution/deposition cycles in all-solid-state symmetric cells with garnet-type electrolytes are also improved by the interface modification with the insertion of metal or metal oxide thin films such as Au, Si, Ge, Al, Al_2O_3, and ZnO [99–103,119]. Moreover, in the case of garnet-type electrolytes, there are several studies on the interface formation in terms of operating temperatures of Li metal cells [95,120]. An advantage of inorganic solid electrolytes is that they have thermal stability even at above 60°C, which is

difficult to use in organic liquid electrolytes. It has been reported that an interfacial resistance between Li metal and garnet-type electrolytes decreases and electrochemical performance of Li metal cells improves at a high temperature at around 100°C [95,120]. As stated above, interface formation is closely associated with the performance of Li metal cells. However, the interface factors determining Li dissolution/deposition behaviors have not been clarified at this point. Structure of the solid electrolytes at the interface, morphology changes of Li metal, and interfacial resistances are important clues to design a favorable interface suppressing the Li dendrites.

The objectives of the present thesis focus on the above two approaches for the development of all-solid-state Li metal batteries with high energy density. One is the research for solid electrolytes with the mechanical properties capable of preventing the growth of Li dendrites. The other is the design of interface formation between Li metal and solid electrolytes in order to suppress the generation of Li dendrites. This thesis especially discusses Li_2S-P_2S_5-based sulfide glass electrolytes as a potential solid electrolyte for Li metal batteries. A comprehensive evaluation on mechanical properties such as an elastic modulus and formability of sulfide glasses are carried out. Glass is composed of glass formers and glass modifiers. Effects by changing them on mechanical properties were investigated. In addition, the elastic moduli of newly measured sulfide glasses and already reported ones are summarized in order to compare the mechanical properties of Li_2S-P_2S_5 glass with those of other chalcogenide and oxide glasses. Moreover, the relationship between the elastic modulus and formability was discussed. Bulk-type all-solid-state cells were evaluated in terms of elastic moduli of glass electrolytes. Second, for the design of interface formation between Li metal and solid electrolytes, bulk-type cells are fabricated using thin Li films prepared by vacuum-evaporation instead of Li foils, which are suitable to evaluate the uniform and wide physical contact interfaces between Li metal and powder-compressed solid electrolytes. Utilization of Li metal, morphology changes of Li metal at Li dissolution/deposition, structure of solid electrolytes at the interface, and interfacial resistances were investigated. Gold (Au) thin films are often used as current collectors for measuring conductivities of sulfide solid electrolytes and therefore Au has good compatibility

with sulfides. Effects of modification by inserting Au thin films to the interface between Li metal and solid electrolytes were also evaluated as a model of the interface modification. High operating temperature of all-solid-state Li metal batteries can improve the electrochemical performance. All-solid-state Li metal batteries were evaluated at high operating temperatures of batteries and the interface modification by Au thin films was also tried.

This doctoral thesis consists of four chapters indicated below:

Chapter 1

This chapter describes the background, the objectives and the contents of this thesis.

Chapter 2

In this chapter, solid electrolytes compatible with Li metal are explored from the viewpoint of their mechanical properties as mainly their elastic moduli and formability. First of all, elastic moduli and formability of a Li_2S-P_2S_5 glass system were evaluated. It is anticipated that the mechanical properties are different between glass and crystalline electrolytes. Formability of $75Li_2S \cdot 25P_2S_5$ (mol%) glasses, glass-ceramics, and crystals synthesized by solid phase reactions were compared. Mechanical properties of four types of sulfide glass systems are evaluated: Li_2S-P_2S_5 glasses with lithium halides as an additional component (Li_2S-P_2S_5-LiX (X = I, Br, Cl)), ones where P_2S_5 is totally or partially replaced by the other glass former (Li_2S-SiS_2, Li_2S-GeS_2, and Li_2S-P_2S_5-GeS_2), ones where sulfur is totally or partially replaced by oxygen (Li_2O-P_2O_5, Li_2S-Li_2O-P_2S_5, and Li_2S-P_2S_5-P_2O_5), and ones where Li_2S is totally replaced by Na_2S, Ag_2S, MgS, and SnS (R_xS_y-P_2S_5, R = Li, Na, Ag, Mg, Sn). Elastic moduli of their sulfide glass electrolytes were measured by an ultrasonic pulse echo method using highly dense pellets prepared by a hot press at around their glass transition temperature. The measured elastic moduli of sulfide glasses and already reported ones were summarized from the viewpoint of their mean atomic volumes. Their formability was evaluated by relative density and microstructure of powder-compaction pellets pressed at room temperature. The relationship

between elastic moduli and formability was discussed. It is assumed that the glass electrolytes with a low elastic modulus can accommodate volume changes of electrode active materials, including Li metal, during charging and discharging. All-solid-state cells were fabricated using solid electrolytes with different Young's moduli and Si electrodes as model active materials exhibiting large volume changes.

Chapter 3

The purpose of this chapter is the improvement of all-solid-state Li metal batteries by examining interface formation between Li metal and solid electrolytes. At first, all-solid-state Li symmetric cells were fabricated by vacuum-evaporation of Li metal on powder-compressed pellets of Li_3PS_4 glass electrolytes. It makes possible an ideal evaluation on the interface between Li metal and solid electrolytes with a uniform and wide contact area. The utilization of Li metal, morphology changes of Li metal, and the interfacial resistance were evaluated for the cells. First principle calculations suggest that Li_3PS_4 electrolytes thermodynamically decompose into Li_2S and Li_3P in contact with Li metal [121]. The structure changes of Li_3PS_4 electrolytes at the interface were investigated by XPS. In addition, it is suggested that the decomposition products are an electronic insulator, which passivates further decomposition reactions and stabilizes the interface kinetically [121]. SEM observation and impedance analyses were carried out for the Li/Li_3PS_4 interface after storage in a dry argon atmosphere for one year. Moreover, effects of modification by inserting Au thin films to the interface between Li metal and Li_3PS_4 electrolytes on the above evaluations came up for discussion. It is anticipated that electrochemical performance of Li metal cells will improve by increasing the operating temperature. The Li dissolution/deposition behavior of Li metal cells with Li_3PS_4 glass electrolytes was compared at 25°C and 100°C. The interface modification by Au thin films was also examined at 100°C.

Chapter 4

This chapter summarizes all the conclusions in this thesis.

Reference

[1] D. Larcher, J. M. Tarascon, *Nat. Chem.* **7** (2015) 19–29.

[2] J. M. Tarascon, M. Armand, *Nature*. **414** (2001) 359–67.

[3] S. Chu, A. Majumdar, *Nature*. **488** (2012) 294–303.

[4] A. Fotouhi, D. J. Auger, K. Propp, S. Longo, M. Wild, *Renew. Sustain. Energy Rev.* **56** (2016) 1008–1021.

[5] L. Lu, X. Han, J. Li, J. Hua, M. Ouyang, *J. Power Sources*. **226** (2013) 272–288.

[6] K. M. Tan, V. K. Ramachandaramurthy, J. Y. Yong, *Renew. Sustain. Energy Rev.* **53** (2016) 720–732.

[7] R. Spotnitz, J. Franklin, *J. Power Sources*. **113** (2003) 81–100.

[8] Q. Wang, P. Ping, X. Zhao, G. Chu, J. Sun, C. Chen, *J. Power Sources*. **208** (2012) 210–224.

[9] J. Janek, W. G. Zeier, *Nat. Energy*. **1** (2016) 16141.

[10] A. Manthiram, X. Yu, S. Wang, *Nat. Rev. Mater.* **2** (2017) 16103.

[11] K. Takada, *Acta Mater.* **61** (2013) 759–770.

[12] M. Tatsumisago, F. Mizuno, A. Hayashi, *J. Power Sources*. **159** (2006) 193–199.

[13] Z. Liu, W. Fu, E.A. Payzant, X. Yu, Z. Wu, N. J. Dudney, J. Kiggans, K. Hong, A. J. Rondinone, C. Liang, *J. Am. Chem. Soc.* **135** (2013) 975–978.

[14] K. H. Park, D. Y. Oh, Y. E. Choi, Y. J. Nam, L. Han, J. Y. Kim, H. Xin, F. Lin, S. M. Oh, Y. S. Jung, *Adv. Mater.* **28** (2016) 1874–1883.

[15] Y. Li, B. Xu, H. Xu, H. Duan, X. Lü, S. Xin, W. Zhou, L. Xue, G. Fu, A. Manthiram, J. B. Goodenough, *Angew. Chemie - Int. Ed.* **56** (2017) 753–756.

[16] A. Aboulaich, R. Bouchet, G. Delaizir, V. Seznec, L. Tortet, M. Morcrette, P. Rozier, J. M. Tarascon, V. Viallet, M. Dollé, *Adv. Energy Mater.* **1** (2011) 179–183.

[17] B. Liu, K. Fu, Y. Gong, C. Yang, Y. Yao, Y. Wang, C. Wang, Y. Kuang, G. Pastel, H. Xie, E. D. Wachsman, L. Hu, *Nano Lett.* **17** (2017) 4917–4923.

[18] K. Fu, Y. Gong, G. T. Hitz, D. W. McOwen, Y. Li, S. Xu, Y. Wen, L. Zhang, C. Wang, G. Pastel, J. Dai, B. Liu, H. Xie, Y. Yao, E. D. Wachsman, L. Hu, *Energy*

Environ. Sci. **10** (2017) 1568–1575.

[19] C. Yada, A. Ohmori, K. Ide, H. Yamasaki, T. Kato, T. Saito, F. Sagane, Y. Iriyama, *Adv. Energy Mater.* **4** (2014) 1–5.

[20] S. Yubuchi, Y. Ito, T. Matsuyama, A. Hayashi, M. Tatsumisago, *Solid State Ionics*. **285** (2016) 79–82.

[21] G. Oh, M. Hirayama, O. Kwon, K. Suzuki, R. Kanno, *Chem. Mater.* **28** (2016) 2634–2640.

[22] M. Nagao, A. Hayashi, M. Tatsumisago, *Electrochim. Acta*. **56** (2011) 6055–6059.

[23] H. Nagata, Y. Chikusa, *J. Power Sources*. **263** (2014) 141–144.

[24] H. Nagata, Y. Chikusa, *J. Power Sources*. **264** (2014) 206–210.

[25] H. Nagata, Y. Chikusa, *J. Power Sources*. **329** (2016) 268–272.

[26] S. Kinoshita, K. Okuda, N. Machida, M. Naito, T. Sigematsu, *Solid State Ionics*. **256** (2014) 97–102.

[27] C. Yu, L. Eijck, S. Ganapathy, M. Wagemaker, *Electrochim. Acta*. **215** (2016) 93–99.

[28] N. Tanibata, H. Tsukasaki, M. Deguchi, S. Mori, A. Hayashi, M. Tatsumisago, *J. Mater. Chem. A.* **5** (2017) 11224–11228.

[29] A. Unemoto, S. Yasaku, G. Nogami, M. Tazawa, M. Taniguchi, M. Matsuo, T. Ikeshoji, S. Orimo, *Appl. Phys. Lett.* **105** (2014) 3–7.

[30] M. Nagao, A. Hayashi, M. Tatsumisago, *Electrochem. Commun.* **22** (2012) 177–180.

[31] M. Nagao, A. Hayashi, M. Tatsumisago, *Electrochemistry*. **80** (2012) 734–736.

[32] M. Nagao, A. Hayashi, M. Tatsumisago, T. Kanetsuku, T. Tsuda, S. Kuwabata, *Phys. Chem. Chem. Phys.* **15** (2013) 18600.

[33] G. Sahu, E. Rangasamy, J. Li, Y. Chen, K. An, N. Dudney, C. Liang, *J. Mater. Chem. A.* **2** (2014) 10396.

[34] G. Sahu, Z. Lin, J. Li, Z. Liu, N. Dudney, C. Liang, *Energy Environ. Sci.* **7** (2014) 1053.

[35] E. Rangasamy, Z. Liu, M. Gobet, K. Pilar, G. Sahu, W. Zhou, H. Wu, S. Greenbaum, C. Liang, *J. Am. Chem. Soc.* **137** (2015) 1384–1387.

[36] H. Wang, Z.D. Hood, Y. Xia, C. Liang, *J. Mater. Chem. A.* **4** (2016) 8091–8096.

[37] H. Takahara, M. Tabuchi, T. Takeuchi, H. Kageyama, J. Ide, K. Handa, Y. Kobayashi, Y. Kurisu, S. Kondo, R. Kanno, *J. Electrochem. Soc.* **151** (2004) A1309.

[38] X. Zhang, T. Liu, S. Zhang, X. Huang, B. Xu, Y. Lin, B. Xu, L. Li, C. W. Nan, Y. Shen, *J. Am. Chem. Soc.* **139** (2017) 13779–13785.

[39] X. Yan, Z. Li, Z. Wen, W. Han, *J. Phys. Chem. C*. **121** (2017) 1431–1435.

[40] T. Liu, Y. Ren, Y. Shen, S.X. Zhao, Y. Lin, C. W. Nan, *J. Power Sources*. **324** (2016) 349–357.

[41] J. van den Broek, S. Afyon, J. L. M. Rupp, *Adv. Energy Mater.* **6** (2016) 1–11.

[42] K. Fu, Y. Gong, S. Xu, Y. Zhu, Y. Li, J. Dai, C. Wang, B. Liu, G. Pastel, H. Xie, Y. Yao, Y. Mo, E. Wachsman, L. Hu, *Chem. Mater.* **29** (2017) 8037–8041.

[43] H. Wakayama, H. Yonekura, Y. Kawai, *Chem. Mater.* **28** (2016) 4453–4459.

[44] F. Du, N. Zhao, Y. Li, C. Chen, Z. Liu, X. Guo, *J. Power Sources*. **300** (2015) 24–28.

[45] A. Unemoto, T. Ikeshoji, S. Yasaku, M. Matsuo, V. Stavila, T. J. Udovic, S. Orimo, *Chem. Mater.* **27** (2015) 5407–5416.

[46] K. Yoshida, S. Suzuki, J. Kawaji, A. Unemoto, S. Orimo, *Solid State Ionics*. **285** (2016) 96–100.

[47] Y. Kato, S. Hori, T. Saito, K. Suzuki, M. Hirayama, A. Mitsui, M. Yonemura, H. Iba, R. Kanno, *Nat. Energy*. **1** (2016) 16030.

[48] Y. Inaguma, C. Liquan, M. Itoh, T. Nakamura, T. Uchida, H. Ikuta, M. Wakihara, *Solid State Commun.* **86** (1993) 689–693.

[49] Y. Inaguma, L. Chen, M. Itoh, T. Nakamura, *Solid State Ionics*. **70–71** (1994) 196–202.

[50] M. Yashima, M. Itoh, Y. Inaguma, Y. Morii, *J. Am. Chem. Soc.* **127** (2005) 3491–3495.

[51] H. Aono, E. Sugimoto, Y. Sadaoka, N. Imanaka, G. Adachi, *J. Electrochem. Soc.* **137** (1990) 1023–1027.

[52] G. Adachi, N. Imanaka, H. Aono, *Ceram.* (1996) 127–135.

[53] R. Murugan, V. Thangadurai, W. Weppner, *Angew. Chemie - Int. Ed.* **46** (2007) 7778–7781.

[54] V. Thangadurai, S. Narayanan, D. Pinzaru, *Chem. Soc. Rev.* **43** (2014) 4714.

[55] V. Thangadurai, D. Pinzaru, S. Narayanan, A. K. Baral, *J. Phys. Chem. Lett.* **6** (2015) 292–299.

[56] E. Rangasamy, J. Wolfenstine, J. Sakamoto, *Solid State Ionics*. **206** (2012) 28–32.

[57] S. Ohta, T. Kobayashi, T. Asaoka, *J. Power Sources*. **196** (2011) 3342–3345.

[58] M. Huang, T. Liu, Y. Deng, H. Geng, Y. Shen, Y. Lin, C. W. Nan, *Solid State Ionics*. **204**–**205** (2011) 41–45.

[59] V. Thangadurai, W. Weppner, *J. Solid State Chem.* **179** (2006) 974–984.

[60] R. Kanno, M. Murayama, *J. Electrochem. Soc.* **148** (2001) A742.

[61] M. Murayama, N. Sonoyama, A. Yamada, R. Kanno, *Solid State Ionics*. **170** (2004) 173–180.

[62] N. Kamaya, K. Homma, Y. Yamakawa, M. Hirayama, R. Kanno, M. Yonemura, T. Kamiyama, Y. Kato, S. Hama, K. Kawamoto, A. Mitsui, *Nat. Mater.* **10** (2011) 682–686.

[63] R. P. Rao, S. Adams, *Phys. Status Solidi Appl. Mater. Sci.* **208** (2011) 1804–1807.

[64] S. Boulineau, M. Courty, J. M. Tarascon, V. Viallet, *Solid State Ionics*. **221** (2012) 1–5.

[65] S. Yubuchi, S. Teragawa, K. Aso, K. Tadanaga, A. Hayashi, M. Tatsumisago, *J. Power Sources*. **293** (2015) 941–945.

[66] T. Minami, A. Hayashi, M. Tatsumisago, *Solid State Ionics*. **177** (2006) 2715–2720.

[67] F. Mizuno, A. Hayashi, K. Tadanaga, M. Tatsumisago, *Solid State Ionics*. **177** (2006) 2721–2725.

[68] M. Tatsumisago, A. Hayashi, *Int. J. Appl. Glas. Sci.* **5** (2014) 226–235.

[69] Y. Seino, T. Ota, K. Takada, A. Hayashi, M. Tatsumisago, *Energy Environ. Sci.* **7** (2014) 627–631.

[70] S. Ujiie, T. Inagaki, A. Hayashi, M. Tatsumisago, *Solid State Ionics*. **263** (2014) 57–61.

[71] S. Ujiie, A. Hayashi, M. Tatsumisago, *Mater. Renew. Sustain. Energy*. **3** (2014) 1–8.

[72] A. Fukushima, A. Hayashi, H. Yamamura, M. Tatsumisago, *Solid State Ionics*. **304** (2017) 85–89.

[73] Y. Sun, K. Suzuki, S. Hori, M. Hirayama, R. Kanno, *Chem. Mater.* **29** (2017) 5858–5864.

[74] Y. Wang, W. D. Richards, S. P. Ong, L. J. Miara, J. C. Kim, Y. Mo, G. Ceder, *Nat. Mater.* **14** (2015) 1026–1031.

[75] A. D. Sendek, Q. Yang, E. D. Cubuk, K. A. N. Duerloo, Y. Cui, E. J. Reed, *Energy Environ. Sci.* **10** (2017) 306–320.

[76] Y. Zhu, X. He, Y. Mo, *Adv. Sci.* **4** (2017) 1600517.

[77] R. Mercier, J. P. Malugani, B. Fahys, G. Robert, *Solid State Ionics*. **5** (1981) 663–666.

[78] M. Ménétrier, C. Estournès, A. Levasseur, K. J. Rao, *Solid State Ionics*. **53–56** (1992) 1208–1213.

[79] Y. Guo, H. Li, T. Zhai, *Adv. Mater.* **29** (2017) 1–25.

[80] K. Kerman, A. Luntz, V. Viswanathan, Y. M. Chiang, Z. Chen, *J. Electrochem. Soc.* **164** (2017) A1731–A1744.

[81] D. Aurbach, E. Zinigrad, Y. Cohen, H. Teller, *Solid State Ionics*. **148** (2002) 405–416.

[82] W. Xu, J. Wang, F. Ding, X. Chen, E. Nasybulin, Y. Zhang, J. G. Zhang, *Energy Environ. Sci.* **7** (2014) 513–537.

[83] X. B. Cheng, R. Zhang, C. Z. Zhao, Q. Zhang, *Chem. Rev.* **117** (2017) 10403–10473.

[84] J. B. Bates, N. J. Dudney, B. Neudecker, A. Ueda, C. D. Evans, *Solid State Ionics*. **135** (2000) 33–45.

[85] https://www.excellatron.com/advantage.htm.

[86] T. Yamada, S. Ito, R. Omoda, T. Watanabe, Y. Aihara, M. Agostini, U. Ulissi, J. Hassoun, B. Scrosati, *J. Electrochem. Soc.* **162** (2015) A646–A651.

[87] Y. Tao, S. Chen, D. Liu, G. Peng, X. Yao, X. Xu, *J. Electrochem. Soc.* **163** (2016) A96–A101.

[88] S. Choi, S. Lee, J. Yu, C. H. Doh, Y. C. Ha, *ECS Trans.* **77** (2017) 65–70.

[89] E. Rangasamy, G. Sahu, J. K. Keum, A. J. Rondinone, N. J. Dudney, C. Liang, *J. Mater. Chem. A.* **2** (2014) 4111–4116.

[90] Z. D. Hood, H. Wang, Y. Li, A. S. Pandian, M. Parans Paranthaman, C. Liang, *Solid State Ionics*. **283** (2015) 75–80.

[91] J. M. Whiteley, S. Hafner, C. Zhu, W. Zhang, S. H. Lee, *J. Electrochem. Soc.* **164** (2017) A2962–A2966.

[92] L. Cheng, W. Chen, M. Kunz, K. Persson, N. Tamura, G. Chen, M. Doeff, *ACS Appl. Mater. Interfaces*. **7** (2015) 2073–2081.

[93] M. Botros, R. Djenadic, O. Clemens, M. Möller, H. Hahn, *J. Power Sources*. **309** (2016) 108–115.

[94] A. Sharafi, E. Kazyak, A.L. Davis, S. Yu, T. Thompson, D. J. Siegel, N. P. Dasgupta, J. Sakamoto, *Chem. Mater.* **29** (2017) 7961–7968.

[95] F. Yonemoto, A. Nishimura, M. Motoyama, N. Tsuchimine, S. Kobayashi, Y. Iriyama, *J. Power Sources*. **343** (2017) 207–215.

[96] B. Xu, W. Li, H. Duan, H. Wang, Y. Guo, H. Li, H. Liu, *J. Power Sources*. **354** (2017) 68–73.

[97] R. H. Basappa, T. Ito, H. Yamada, *J. Electrochem. Soc.* **164** (2017) A666–A671.

[98] R. Hongahally Basappa, T. Ito, T. Morimura, R. Bekarevich, K. Mitsuishi, H. Yamada, *J. Power Sources*. **363** (2017) 145–152.

[99] C. L. Tsai, V. Roddatis, C. V. Chandran, Q. Ma, S. Uhlenbruck, M. Bram, P. Heitjans, O. Guillon, *ACS Appl. Mater. Interfaces*. **8** (2016) 10617–10626.

[100] W. Luo, Y. Gong, Y. Zhu, K. K. Fu, J. Dai, S. D. Lacey, C. Wang, B. Liu, X. Han, Y. Mo, E. D. Wachsman, L. Hu, *J. Am. Chem. Soc.* **138** (2016) 12258–12262.

[101] K. Fu, Y. Gong, B. Liu, Y. Zhu, S. Xu, Y. Yao, W. Luo, C. Wang, S. D. Lacey, J. Dai, Y. Chen, Y. Mo, E. Wachsman, L. Hu, *Sci. Adv.* **3** (2017) e1601659.

[102] X. Han, Y. Gong, K. Fu, X. He, G. T. Hitz, J. Dai, A. Pearse, B. Liu, H. Wang, G. Rubloff, Y. Mo, V. Thangadurai, E. D. Wachsman, L. Hu, *Nat. Mater.* **16** (2016) 572–579.

[103] C. Wang, Y. Gong, B. Liu, K. Fu, Y. Yao, E. Hitz, Y. Li, J. Dai, S. Xu, W. Luo, E. D. Wachsman, L. Hu, *Nano Lett.* **17** (2017) 565–571.

[104] Y. Ren, Y. Shen, Y. Lin, C. W. Nan, *Electrochem. Commun.* **57** (2015) 27–30.

[105] E. J. Cheng, A. Sharafi, J. Sakamoto, *Electrochim. Acta*. **223** (2017) 85–91.

[106] P. Arora, Z. Zhang, *Chem. Rev.* **104** (2004) 4419–4462.

[107] S. S. Zhang, *J. Power Sources*. **164** (2007) 351–364.

[108] H. Munakata, M. Kotobuki, K. Sasajima, Y. Yamamoto, K. Kanamura, Abstract #180. Proceedings of the 15th Int. Meeting on Lithium Batteries; IMLB: Montreal, Canada, (2010) pp. 180.

[109] W. Liu, D. Lin, A. Pei, Y. Cui, *J. Am. Chem. Soc.* **138** (2016) 15443–15450.

[110] Z. Xue, D. He, X. Xie, *J. Mater. Chem. A.* **3** (2015) 19218–19253.

[111] C. Yang, K. Fu, Y. Zhang, E. Hitz, L. Hu, *Adv. Mater.* **29** (2017) 1–28.

[112] A. Mauger, M. Armand, C. M. Julien, K. Zaghib, *J. Power Sources*. **353** (2017) 333–342.

[113] M. Rosso, C. Brissot, A. Teyssot, M. Dollé, L. Sannier, J. M. Tarascon, R. Bouchet, S. Lascaud, *Electrochim. Acta*. **51** (2006) 5334–5340.

[114] K. J. Harry, D. T. Hallinan, D. Y. Parkinson, A. A. MacDowell, N. P. Balsara, *Nat. Mater.* **13** (2013) 69–73.

[115] M. Nakayama, M. Kotobuki, H. Munakata, M. Nogami, K. Kanamura, *Phys. Chem. Chem. Phys.* **14** (2012) 10008.

[116] S. Yu, R. D. Schmidt, R. Garcia-Mendez, E. Herbert, N. J. Dudney, J. B. Wolfenstine, J. Sakamoto, D. J. Siegel, *Chem. Mater.* **28** (2016) 197–206.

[117] A. Sakuda, A. Hayashi, M. Tatsumisago, *Sci Rep*. **3** (2013) 2261.

[118] A. Sakuda, A. Hayashi, Y. Takigawa, K. Higashi, M. Tatsumisago, *J. Ceram. Soc. Japan*. **121** (2013) 946–949.

[119] W. Luo, Y. Gong, Y. Zhu, Y. Li, Y. Yao, Y. Zhang, K.K. Fu, G. Pastel, C.F. Lin, Y. Mo, E.D. Wachsman, L. Hu, *Adv. Mater.* **29** (2017) 1–7.

[120] A. Sharafi, H.M. Meyer, J. Nanda, J. Wolfenstine, J. Sakamoto, *J. Power Sources*. **302**

(2016) 135–139.

[121] Y. Zhu, X. He, Y. Mo, *ACS Appl. Mater. Interfaces*. **7** (2015) 23685–23693.

2. Mechanical properties of Li_2S-P_2S_5-based sulfide glasses and application to all-solid-state batteries

2.1. Introduction

Solid electrolytes are a key material for the development of all-solid-state batteries and are preferred for their high ionic conductivity, thermal stability, chemical stability to positive and negative electrode active materials, and mechanical properties, such as softness, that allows them to accommodate volume changes in electrode active materials [1–3]. The mechanical properties of solid electrolytes are particularly unique and critical for all-solid-state batteries. The mechanical properties are also important for all-solid-state batteries using a lithium (Li) metal negative electrode because it exhibits a large volume change [4].

There are two categories of inorganic solid electrolytes: oxides and sulfides. Most of the oxide electrolytes are stiff ceramics, with elastic moduli in the 100–200 GPa range [5]. Oxide ceramic electrolytes require sintering process at high temperatures over 1000°C to reduce the resistance at grain boundaries [6–8]. Such high temperatures lead to undesirable side reactions between electrode/electrolyte interfaces, which cause cell capacities to decrease. Reduction of sintering temperature [9–12] and additional experimental procedures such as screen-printing [13], aerosol deposition [14], or mixing with polymer or gel-polymer electrolytes [15–18] are used to improve interfacial issues in all-solid-state batteries using oxide ceramic electrolytes. On the other hand, all-solid-state batteries using sulfide electrolytes achieve high cell capacities and long cycle performance by simply pressing the powders of solid electrolytes and electrode active materials at room temperature [1,19]. Sakuda *et al.* have reported favorable mechanical properties of Li_2S-P_2S_5 glass electrolytes with high lithium-ion conductivities [20,21]. Li_2S-P_2S_5 glasses have a low Young's modulus (18-25 GPa) and excellent formability allowing them to be highly densified by pressing even at room temperature. These "soft" mechanical properties of the sulfide electrolytes contribute to forming good contacts of solid-solid interfaces between the solid electrolytes and electrode

active materials, leading to excellent electrochemical performance of the cells. Thus, sulfide electrolytes such as the Li_2S-P_2S_5 glass systems have interesting mechanical properties, making them the appropriate choices for all-solid-state batteries. Since sulfide electrolytes are unstable in air, there have not been sufficient studies conducted to evaluate their mechanical properties, therefore further studies are required.

The following three types of sulfide electrolytes have been reported: crystalline, glass, and glass-ceramic materials. Conductivities of glass electrolytes are not extremely high compared to those of crystalline electrolytes such as $Li_{10}GeP_2S_{12}$ [22,23], $Li_{9.54}Si_{1.74}P_{1.44}S_{11.7}Cl_{0.3}$ [24], and $Li_7P_3S_{11}$ [25], which exhibit conductivities of the order of 10^{-2} S cm^{-1}. However, the glass electrolytes have several advantages. They have few grain boundaries because of their isotropic structure, which reduce the interfacial resistances in all-solid-state batteries. Decreasing the risk of short-circuiting with the growth of Li dendrites through the grain boundaries is also considered an advantage. In addition, since glass is composed of a former and a modifier, it can present a wide range of compositions. Controlling them leads to preparing materials with diverse characteristics. For example, Minami *et al*. [26] and Ohtomo *et al*. [27,28] have reported that adding small amounts of oxides to Li_2S-P_2S_5 glasses improved their electrochemical and chemical stability in air without decreasing their conductivities. Moreover, it has been reported that conductivities of sulfide glasses increase to values in the 10^{-3} S cm^{-1} order by adding lithium halides [29–32]. This implies that sulfide glasses have a wide range of mechanical parameters depending on their composition.

The objective of this chapter is exploring solid electrolytes compatible with Li metal from the viewpoint of their mechanical properties mainly such as their elastic moduli and formability. In this chapter, comprehensive evaluation on mechanical properties of sulfide glasses based on Li_2S-P_2S_5 glass systems was carried out.

First of all, the elastic moduli and formability of a Li_2S-P_2S_5 glass system were evaluated. The author assumes that the mechanical properties of the glass and crystalline materials would be different, but the relationship has not been clarified. Thus, the author compared the

formability of $75Li_2S \cdot 25P_2S_5$ (mol%) glasses, glass-ceramics, and crystals in this study.

Secondly, the mechanical properties of Li_2S-P_2S_5 glasses with lithium halides as an additional component (Li_2S-P_2S_5-LiX (X = I, Br, Cl)) were investigated. Adding lithium halides is expected to confer two positive influences on the glass electrolytes. One is an increase in the ionic conductivity, which is well-known in lithium ion conducting glasses [29–32]. The other one is a possible decrease in the elastic modulus owing to a reduction in the glass transition temperature. Although there are many reports on the ionic conductivity and electrochemical properties of Li_2S-P_2S_5 glasses with lithium halides, their mechanical properties have not been investigated. In this thesis, the elastic moduli and formability of Li_2S-P_2S_5 glasses with lithium halides were investigated. In addition, it is assumed that glass electrolytes with a low elastic modulus can accommodate volume changes of electrode active materials, including Li metal, during charging and discharging. In order to investigate the effect, all-solid-state cells were fabricated using solid electrolytes with different Young's moduli and Si electrodes as model active materials exhibiting large volume changes [33–35].

Thirdly, the mechanical properties of the sulfide glasses in the following three systems: 1) Li_2S-P_2S_5 where P_2S_5 is totally or partially replaced by SiS_2 or GeS_2 (Li_2S-SiS_2, Li_2S-GeS_2, and Li_2S-P_2S_5-GeS_2), 2) Li_2S-P_2S_5 where S is totally or partially replaced by O (Li_2O-P_2O_5, Li_2S-Li_2O-P_2S_5, and Li_2S-P_2S_5-P_2O_5), and 3) Li_2S-P_2S_5 where Li_2S is totally replaced by Na_2S, Ag_2S, MgS, and SnS (R_xS_y-P_2S_5, R = Na, Ag, Mg, Sn). The author investigated the effects of changing the glass former and modifier on the mechanical properties of the sulfide glasses. Elastic moduli of their sulfide glass electrolytes were measured by an ultrasonic pulse echo method. Their mean atomic volumes [36] are used to summarize the measured elastic moduli of sulfide glasses. Their formability was evaluated by the relative density and microstructure of powder-compaction pellets just pressed at room temperature. The relationship between elastic moduli and formability was also discussed.

2.2. Experimental

2.2.1. Sample preparation

All Li_2S-P_2S_5–based glasses were prepared by a mechanochemical technique using a planetary ball mill apparatus. Reagent-grade Li_2S (Idemitsu Kosan or Mitsuwa Chemical, >99.9%), P_2S_5 (Aldrich, >99%), LiI (Aldrich, 99.99%), LiBr (Aldrich, 99.999%), LiCl (Aldrich, 99.9%), Li_2O (Furuuchi Chemical, 99.9%), P_2O_5 (Kojundo Chemical, 99.999%), GeS_2 (Furuuchi Chemical, 99.9999%), SiS_2 (Furuuchi Chemical, 99.9%), Na_2S (Nagao, 99.1%), Ag_2S (Aldrich, 99.9%), SnS (Kojundo Chemical, 99.9%), and MgS (Kojundo Chemical, 99.9%) powders were used as the starting materials. These starting materials in stoichiometric proportions were ball-milled until amorphous samples were obtained. $75Li_2S \cdot 25P_2S_5$ (mol%: Li_3PS_4) glass-ceramic powders were prepared by heating the glass powders at 235°C for 2 h in a dry Ar atmosphere. Moreover, crystalline powders with a $75Li_2S \cdot 25P_2S_5$ (mol%) composition were synthesized by carrying out solid phase reactions using Li_2S and P_2S_5 [37]. A mixture of Li_2S and P_2S_5 powders was placed into a carbon crucible in an Ar-filled glove box and sealed in a quartz tube in vacuum. The quartz tube was heated at 500°C for 5 days and slowly cooled to room temperature.

2.2.2. Characterization

The elastic moduli were evaluated for hot-pressed and cold-pressed pellets by an ultrasonic pulse-echo technique using 5 MHz frequency transducers. Hot-pressed pellets were prepared by pelletizing the powders at 270 or 360 MPa at around each glass transition temperature for 4 h in an Ar-filled glove box. Pressing powders at around glass transition temperature makes the glasses soft via the supercooled liquid state, which gives highly dense glass pellets. Cold-pressed pellets of the samples were also prepared by pelletizing the powders at 540 or 800 MPa at room temperature for 5 min. The thickness and diameter of the prepared pellets were about 2-3 mm and 10 mm, respectively. The density of the pellets employed ρ_{HP} values. Those prepared pellets were packed in a polymer bag (thickness of 0.04 mm) in an Ar-filled glove box and evaluated using an ultrasonic pulser/receiver (5077PR, Olympus) in an air atmosphere. The influence of the bag was found to be negligible because the bag was thin enough. In order to transmit longitudinal and shear waves easily between

transducers and the pellets packed in the polymer bag, a couplant (Couplant B, Olympus) and Sonicoat (SHN-B25, Saan-Tech) were used. The elastic moduli of the samples are calculated using the following equations:

$$G = \rho_{HP} V_S^2$$

$$\nu = (V_L^2 - 2V_S^2)/2(V_L^2 - V_S^2)$$

$$E = 2G(1+\nu)$$

$$B = E/3(1-2\nu)$$

where V_S is the velocity of the shear wave, V_L is the velocity of the longitudinal wave, G is the shear modulus, ρ_{HP} is the density of the pellet prepared by hot pressing, ν is the Poisson's ratio, E is the Young's modulus, and B is the bulk modulus.

The formability was investigated from the viewpoint of the relative densities and microstructures of the powder-compressed pellets. The glass powders were compressed mainly at 360 MPa to evaluate the behavior of densification at room temperature. The density of the obtained pellets (ρ_{bulk}) (10 mm in diameter) were determined by their mass and dimensions; the density of the glass powders (ρ_0) were evaluated using a gas pycnometer (AccuPyc II 1340, Shimazu) placed in an Ar atmosphere. The relative density was calculated as ρ_{bulk}/ρ_0 or ρ_{HP}/ρ_0. The microstructures of the pellets were observed by scanning electron microscopy (SEM; JSM-6610A, JEOL) or (FE-SEM; SU8200, Hitachi). Ar ion-milling was done to prepare a flat surface of several samples using an ion-milling system (IM4000; Hitachi).

To measure ionic conductivity, the glass electrolyte powders were put into a φ10 mm die and pelletized at ambient temperatures. The pressure applied for pelletizing was 360 MPa. The obtained pellets were sandwiched between two stainless steel rods as an ion-blocking electrode in an Ar-filled glove box. The ionic conductivities of the glasses at room temperature were measured at each pressure using an AC impedance analyzer (VMP3, Bio-logic), whose lead wires were connected with the stainless-steel electrodes in the glove box. The frequency range and applied voltage were respectively 10Hz – 1 MHz and 10 mV.

The local structure of the glasses was analyzed by Raman spectroscopy using a

spectrometer (LabRAM HR800, Horiba) equipped with a green laser (532 nm). Differential thermal analysis (DTA) was performed on the milled powders using a thermal analyser (Thermo Plus TG8110, Rigaku) at a heating rate of 10 °C min^{-1}.

2.2.3. Cell configuration

The effects of different mechanical properties of the solid electrolytes on the cell performance were investigated for the cells using Si composite electrodes. Micron sized Si powder (Kojundo Chemical), one of the solid electrolytes (SEs), and acetylene black (AB) were mixed in an agate mortar at a weight ratio of 40:60:10 to prepare Si composite electrodes. The Si composite electrode was used as the working electrode and $75Li_2S \cdot 25P_2S_5$ (mol%) glass electrolyte was used as the separator layer. The Si composite electrode (10 mg) and separator layer (80 mg) were put in a polycarbonate tube (10 mm in diameter) and pressed together at a pressure of 360 MPa. A Li-In alloy foil was placed on the surface of the separator layer side of the bilayer pellet as a counter electrode. The three-layered pellet was sandwiched between two stainless steel rods as a current collector and a pressure of 120 MPa was applied to assemble the cell. All the processes were carried out in an Ar-filled glove box. Electrochemical tests were carried out at 0.064 mA cm^{-2} and 0.13 mA cm^{-2} at 25 °C in an Ar atmosphere using a charge-discharge measurement device (BTS-2004, Nagano Co.).

2.3. Results and discussion

2.3.1 Mechanical properties of Li_2S-P_2S_5 glasses and their comparison with the crystalline materials

Elastic moduli of Li_2S-P_2S_5 glass systems measured by an ultrasonic pulse-echo technique are shown in the Table 2-3-1. The already measured ones previously reported by Sakuda *et. al.* [20] are also listed in the same table. Young's moduli of oxide glasses are discussed by the bond dissociation energy per unit volume and ion packing density [38,39]. The author discussed the measured Young's moduli of sulfide glasses based on these two factors. In this research, the Young's moduli of sulfide glasses were summarized using mean

Table 2-3-1 The longitudinal velocity (V_L), shear velocity (V_S), density (ρ_{HP}), shear modulus (G), Young's modulus (E), bulk modulus (B),and Poisson's ratio (ν) of Li_2S-P_2S_5 glasses prepared by a hot press at various molding temperatures and pressures. The relative density is calculated from the powder density (ρ_0) of milled glasses.

Sample	Powder density (ρ_0) /g cm^{-3}	Molding condition			Hot-press density (ρ_{HP}) /g cm^{-3}	Relative density /%	V_L /ms^{-1}	V_s /ms^{-1}	G /GPa	E /GPa	ν	B /GPa
		Temperature /°C	Time /h	Pressure /MPa								
$25Li_2S{\cdot}75P_2S_5$	2.02	130	4	270	2.00	99.1	2960	1580	5.0	13.0	0.30	10.9
*$50Li_2S{\cdot}50P_2S_5$	2.00	(230)	-	(360)	(1.89)	94.4	(3390)	(1910)	(6.9)	(17.5)	(0.27)	(12.5)
$67Li_2S{\cdot}33P_2S_5$	1.95	200	4	360	1.95	100	4040	2070	8.4	22.1	0.32	20.7
*$70Li_2S{\cdot}30P_2S_5$	1.92	(240)	-	(360)	(1.91)	99.6	(4020)	(2090)	(8.3)	(21.9)	(0.31)	(19.7)
*$75Li_2S{\cdot}25P_2S_5$	1.88	(190)	-	(360)	(1.88)	99.9	(4150)	(2150)	(8.7)	(22.9)	(0.32)	(20.8)
*$80Li_2S{\cdot}20P_2S_5$	1.85	(190)	-	(360)	(1.85)	100	(4300)	(2270)	(9.5)	(24.9)	(0.31)	(21.5)

* Parentheses indicates data from the reference [20]. The powder and relative densities were measured and calculated in this research.

atomic volumes [36] because ion packing densities of the glasses can be easily estimated by calculating the mean atomic volumes from their densities. The powder densities are basically used for calculations. Young's moduli and the calculated mean atomic volumes of the Li_2S-P_2S_5 glasses are shown in Fig. 2-3-1. Young's moduli increase with the decrease of the mean atomic volumes. The decrease of the mean atomic volumes in the Li_2S-P_2S_5 glasses is associated with structural changes. Raman spectra of Li_2S-P_2S_5 glasses and P_2S_5 crystals are shown in Fig. 2-3-2. The Raman spectra are similar to previous results [40–43]. $25Li_2S \cdot 75P_2S_5$ (mol%) glass contains a molecular P_4S_{10} structure in the region of 100-300 cm^{-1} [40]. In addition, the main anions in Li_2S-P_2S_5 glasses change from PS_3^- (meta-thiophosphate) to $P_2S_7^{4-}$ (pyro-thiophosphate) and PS_4^{3-} (ortho-thiophosphate) with an increase in the Li_2S content, suggesting that anions in Li_2S-P_2S_5 glasses changes from a chain to an isolated structure by breaking the bridging structure of the P-S-P bonds. It is considered that the mean atomic volume decrease (and the ion packing density increase) upon the increase of isolated anions in Li_2S-P_2S_5 glasses, which is a possible reason for the increase in the Young's moduli. It is also anticipated that the bond dissociation energy per unit volume in Li_2S-P_2S_5 glasses would decrease with increasing Li_2S content because the bond dissociation energy of Li-S bonds is lower than that of P-S bonds (Li-S: 313 kJ mol^{-1}, P-S: 442 kJ mol^{-1}) [44], which is not consistent with the increase in the Young's moduli. This suggests that contributions of the bond dissociation energies to the Young's moduli are small for the Li_2S-P_2S_5 glasses.

Formability of Li_2S-P_2S_5 glasses was evaluated by powder compaction tests. Table 2-3-2 shows the bulk density and relative density of cold-pressed pellets of Li_2S-P_2S_5 glasses. The highest relative density is obtained at 75 mol% Li_2S content and the lowest is at 50 mol%. The more isolated structure at 75 mol% composed of Li^+ and PS_4^{3-} ions may promote the better densification. Rouxel *et al.* report that a glass with a highly cross-linked network structure (ex. amorphous silica) has lower Poisson's ratio, while a glass with low-dimensional structure (ex. bulk metallic glass of $Zr_{55}Cu_{30}AlNi_5$) has higher Poisson's ratio [45,46]. In addition, they suggest that ductility is exhibited in indentation tests with the increase in

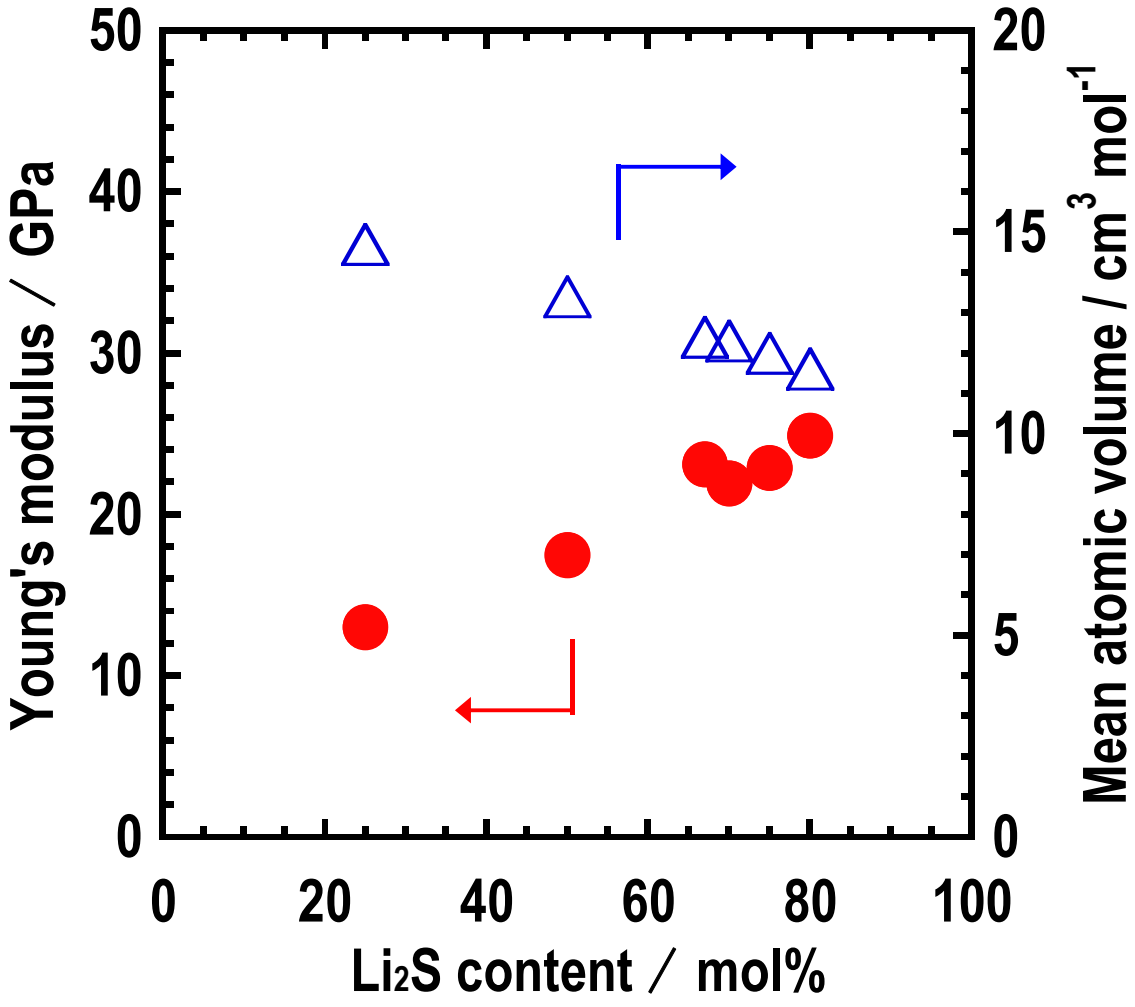

Fig. 2-3-1 Young's moduli and mean atomic volumes of Li_2S-P_2S_5 glasses.

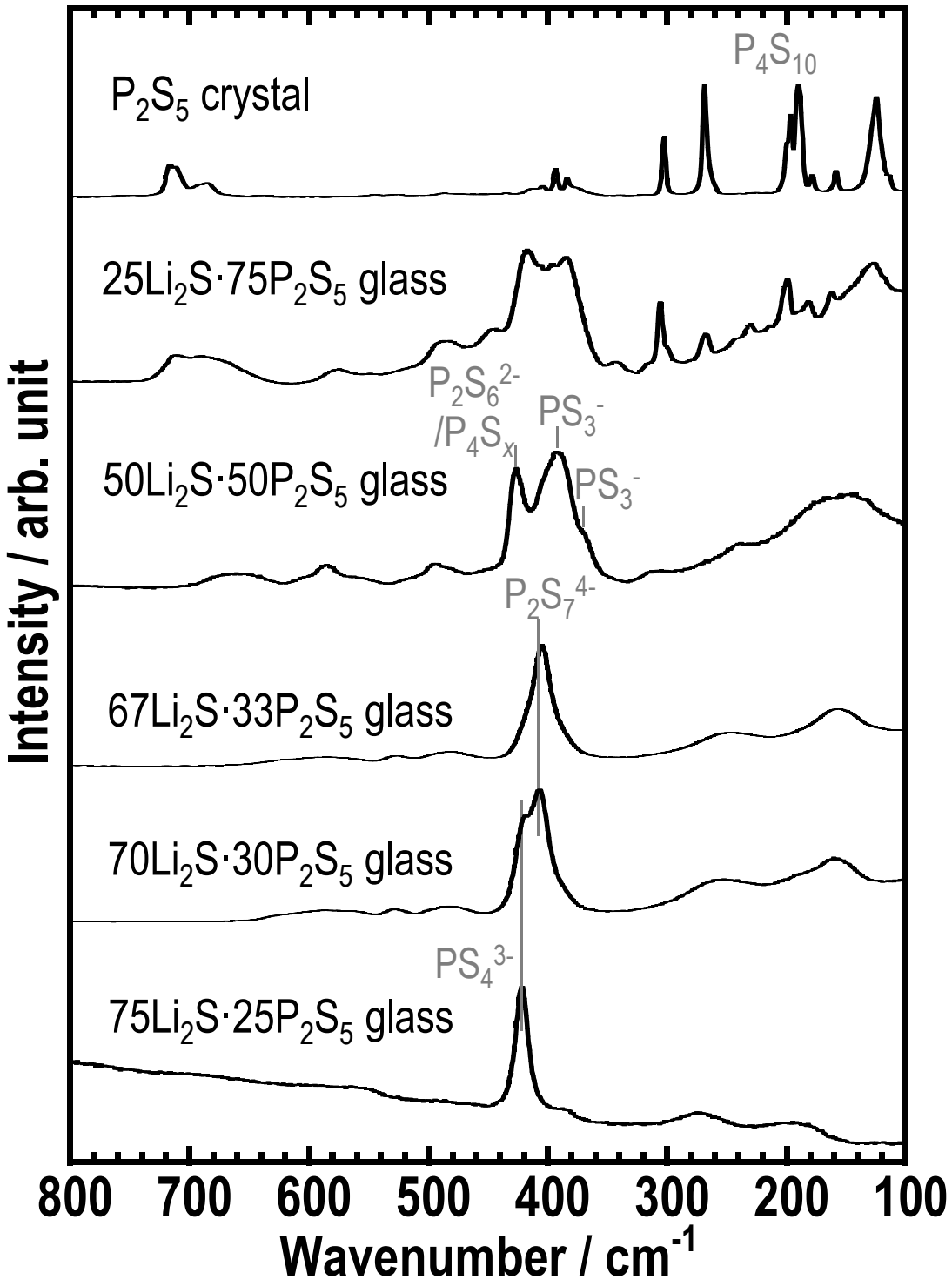

Fig. 2-3-2 Raman spectra of P_2S_5 crystals and Li_2S-P_2S_5 glasses.

Poisson's ratio [45], which means that glass structure with less connectivity tends to exhibit ductile behavior. This suggestion corresponds to our results that glasses with modifier-rich compositions are more easily densified.

Formability of the $75Li_2S \cdot 25P_2S_5$ glass, glass-ceramic, and crystal synthesized by a solid phase reaction was compared. Figure 2-3-3 shows XRD patterns of the as-prepared crystalline samples. The β-Li_3PS_4 and γ-Li_3PS_4 phases are observed for the glass-ceramic and crystal synthesized by a solid phase reaction, respectively. For more accurate measurements on formability, the prepared powders were sieved so that the maximum size of the sample should be less than 53 μm. After sieving, the powders have almost the same size as a secondary particle (Fig. 2-3-4). Figure 2-3-5 (a) shows the molding pressure dependence of the relative density of these materials. The relative density of the glass is smaller than those of the glass-ceramics and crystals at lower pressure. At the lower pressures, it is assumed that the rearrangement of the particles is dominant for the densification [47]. The densification by the rearrangement is affected by the original size of the particles, whose distribution might still remain heterogeneous even after sieving. On the other hand, the relative density of the glass is larger than those of the two crystalline materials at higher pressures. Cross-sectional SEM images of these materials after cold-pressing at 36, 180, 360 MPa are shown in Fig. 2-3-5 (b). It seems that the glass-ceramic and crystals are densified by filling voids by fragmentation or slightly plastic deformation of the particles. In contrast, highly densified areas with a larger size of grains than the original one are observed in the glass compacts at 360 MPa. The voids and grain boundaries in the glass compacts can be reduced owing to the isotropic structure with a free volume of the glass. The better formability of the glass is important to form solid-solid interfaces between electrode active materials and solid electrolytes in bulk-type all-solid-state batteries. The few grain boundaries in the glass are also critical for the use of Li metal negative electrodes because Li dendrites are likely to propagate through the grain boundaries.

Table 2-3-2 Bulk density and relative density of Li_2S-P_2S_5 glasses of cold-pressed (at 360 MPa) pellets. The relative density is calculated from the powder density.

Glass composition	Cold-press density at 360 MPa (ρ_{bulk}) / g cm^{-3}	Relative density / %
$25Li_2S{\cdot}75P_2S_5$	1.74	86.4
$50Li_2S{\cdot}50P_2S_5$	1.70	85.0
$67Li_2S{\cdot}33P_2S_5$	1.67	85.9
$75Li_2S{\cdot}25P_2S_5$	1.70	90.4

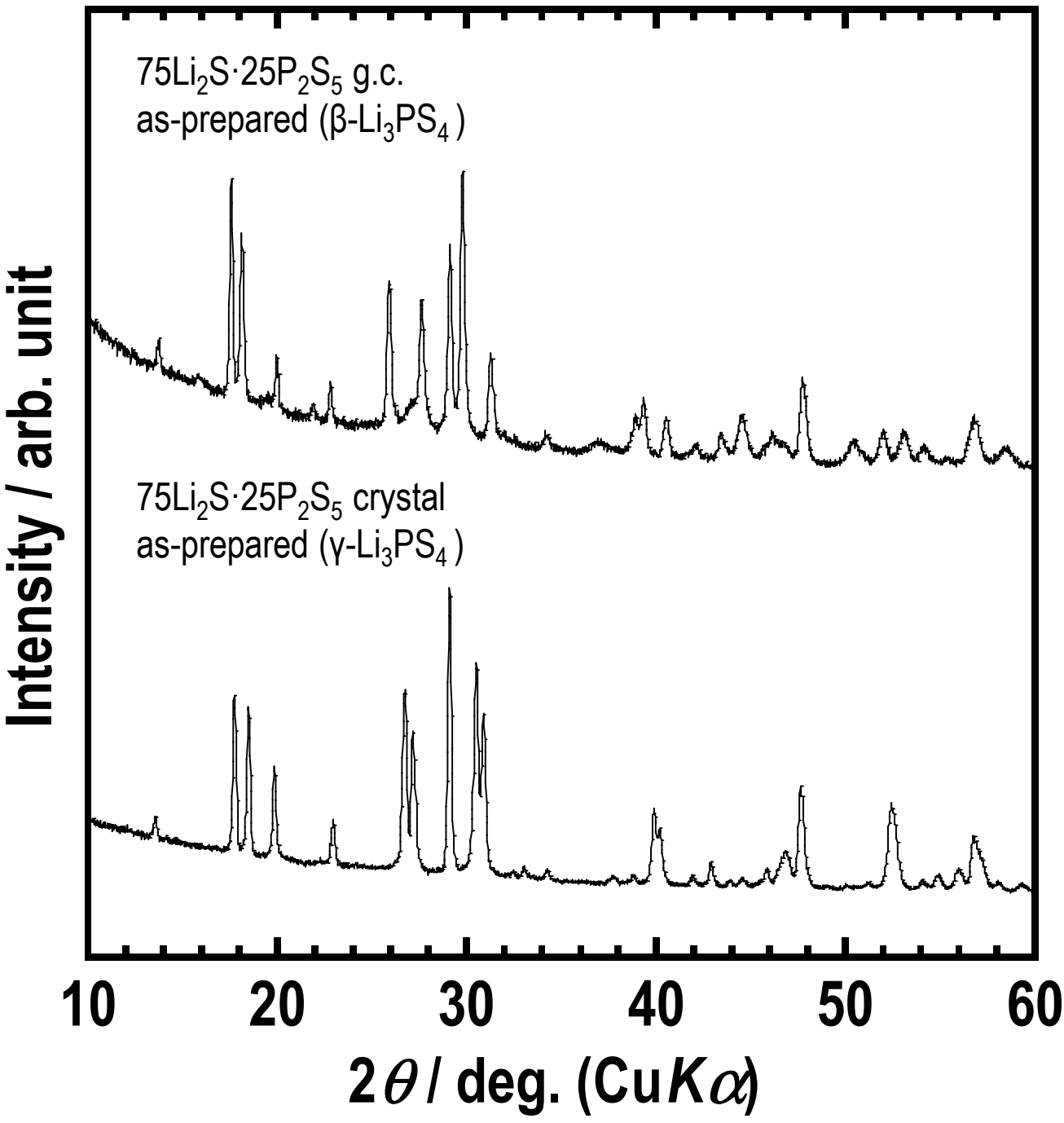

Fig. 2-3-3 XRD patterns of $75Li_2S \cdot 25P_2S_5$ glass-ceramic and crystal synthesized by solid phase reactions.

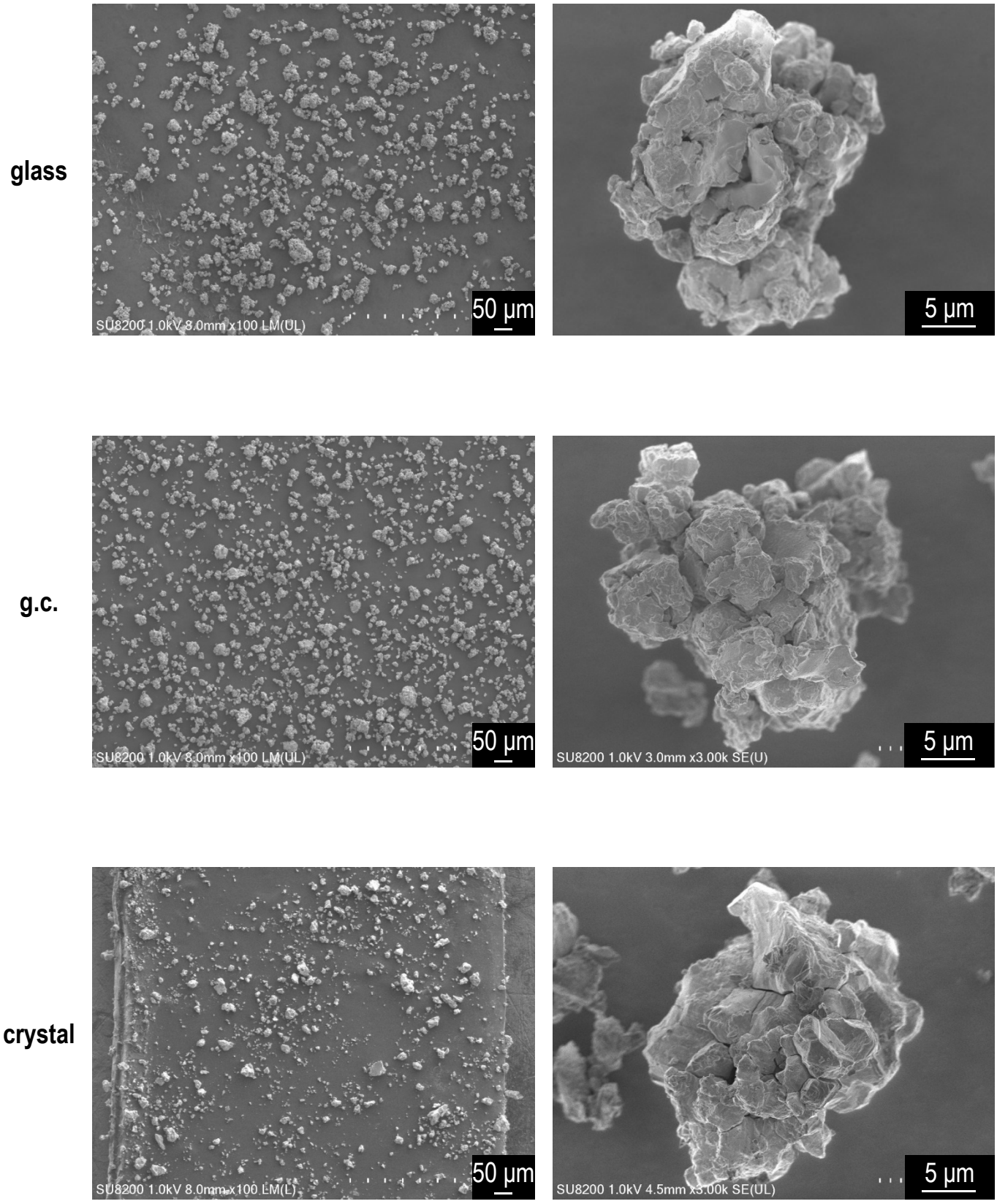

Fig. 2-3-4 SEM images of powders of $75Li_2S \cdot 25P_2S_5$ glass, glass-ceramic, and crystal synthesized by solid phase reactions. The particles were sieved to achieve sizes under 53 µm.

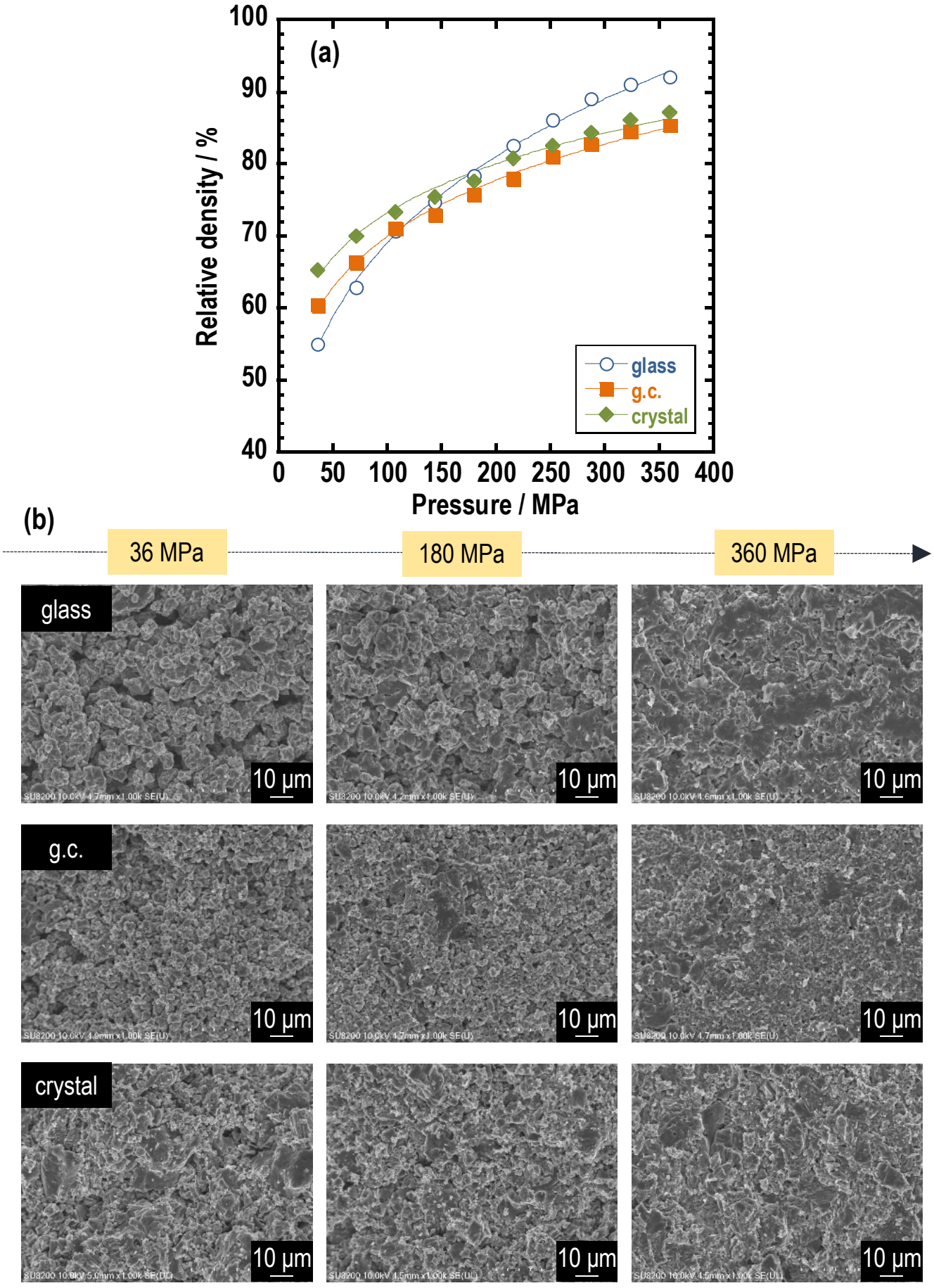

Fig. 2-3-5 (a) Molding pressure dependence of the relative density of $75Li_2S \cdot 25P_2S_5$ glass, glass-ceramic, and crystal. (b) SEM images of fracture cross sections of these materials after cold-pressing at 36, 180, and 360 MPa respectively.

2.3.2 Mechanical properties of Li_2S-P_2S_5 glasses with lithium halides and their application to all-solid-state batteries

Two types of Li_2S-P_2S_5 glass electrolytes with lithium halides were prepared. The first type consisted of Li_2S-P_2S_5 glass electrolytes with different lithium halides. These are denoted as $(100-x)(0.75Li_2S\cdot 0.25P_2S_5)\cdot xLiX$ (mol%) ($0 \leq x \leq 30$, X = I, Br, and Cl). The other set of samples consisted of Li_2S-P_2S_5 glass electrolytes with low Li_2S contents; these are denoted as $(100-y)(0.67Li_2S\cdot 0.33P_2S_5$ or $0.50Li_2S\cdot 0.50P_2S_5)\cdot yLiI$ (mol%) ($0 \leq y \leq 33$). Several representative DTA curves of Li_2S-P_2S_5 glasses with lithium halides, prepared by mechanical milling, are shown in Fig. 2-3-6. Typical endothermic changes attribute to glass transition phenomena can be observed. The glass transition temperatures of all the samples are summarized in Table 2-3-3; they decrease upon the addition of lithium halides. The melting and glass transition temperatures are generally related to the bond energies of the tested materials. Li_2S-P_2S_5 glasses with lithium halides will thus have lower bond energies than those without lithium halides. The glass transition phenomena are not clearly visible in some samples such as $(100-x)(0.75Li_2S\cdot 0.25P_2S_5)\cdot xLiI$ (mol%) (x = 0, 5, 10, 20, and 30), as shown in Fig. 2-3-7. Exothermic peaks were observed in the range of 170 °C to 230 °C; these are attributed to crystallisation, which shifted to lower temperatures with an increase in the lithium halide content. Although it has not been clarified why the glass transition phenomena were not observed clearly, one plausible reason for it is that the crystallization occurred immediately just above their glass transition phenomena. The glass transition temperatures of these glasses are thus expected to decrease upon the addition of lithium halides.

The elastic moduli measured by the ultrasonic pulse echo method, the molding conditions, and the electrical conductivities of Li_2S-P_2S_5 glasses with lithium halides are listed in Table 2-3-4. Some previously reported elastic moduli of Li_2S-P_2S_5 glasses [48] are also listed in the table. The Young's moduli of Li_2S-P_2S_5 glasses decrease upon the addition of lithium halides. Especially, the Young's moduli of $(100-x)(0.75Li_2S\cdot 0.25P_2S_5)\cdot xLiI$ (mol%) (x = 0, 5, 10, 20, and 30) glass electrolytes gradually decrease from 23 GPa (y = 0) to 19 GPa upon the addition of 30 mol% of LiI. The Young's moduli of Li_2S-P_2S_5 glasses with lithium

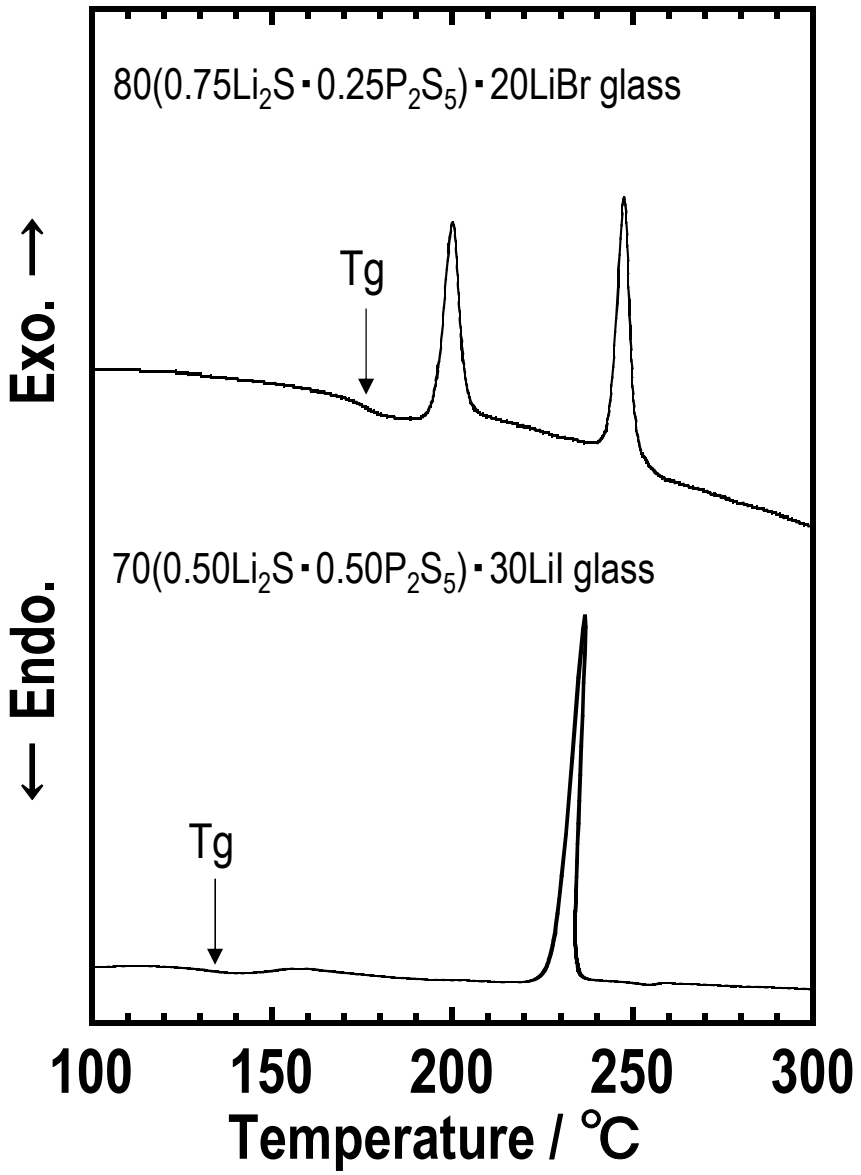

Fig. 2-3-6 Typical DTA curves indicating the glass transition temperatures (Tg) of Li_2S-P_2S_5 glasses with lithium halides.

Table 2-3-3 Glass transition temperature (Tg) for Li_2S-P_2S_5 glasses with lithium halides

Sample	Tg /°C
$75Li_2S \cdot 25P_2S_5$	-
$95(0.75Li_2S \cdot 0.25P_2S_5) \cdot 5LiI$	-
$90(0.75Li_2S \cdot 0.25P_2S_5) \cdot 10LiI$	-
$80(0.75Li_2S \cdot 0.25P_2S_5) \cdot 20LiI$	-
$70(0.75Li_2S \cdot 0.25P_2S_5) \cdot 30LiI$	-
$67Li_2S \cdot 33P_2S_5$	224
$67(0.67Li_2S \cdot 0.33P_2S_5) \cdot 33LiI$	162
$50Li_2S \cdot 50P_2S_5$	165
$75(0.50Li_2S \cdot 0.50P_2S_5) \cdot 25LiI$	141
$70(0.50Li_2S \cdot 0.50P_2S_5) \cdot 30LiI$	130
$90(0.75Li_2S \cdot 0.25P_2S_5) \cdot 10LiBr$	196
$80(0.75Li_2S \cdot 0.25P_2S_5) \cdot 20LiBr$	177
$90(0.75Li_2S \cdot 0.25P_2S_5) \cdot 10LiCl$	-

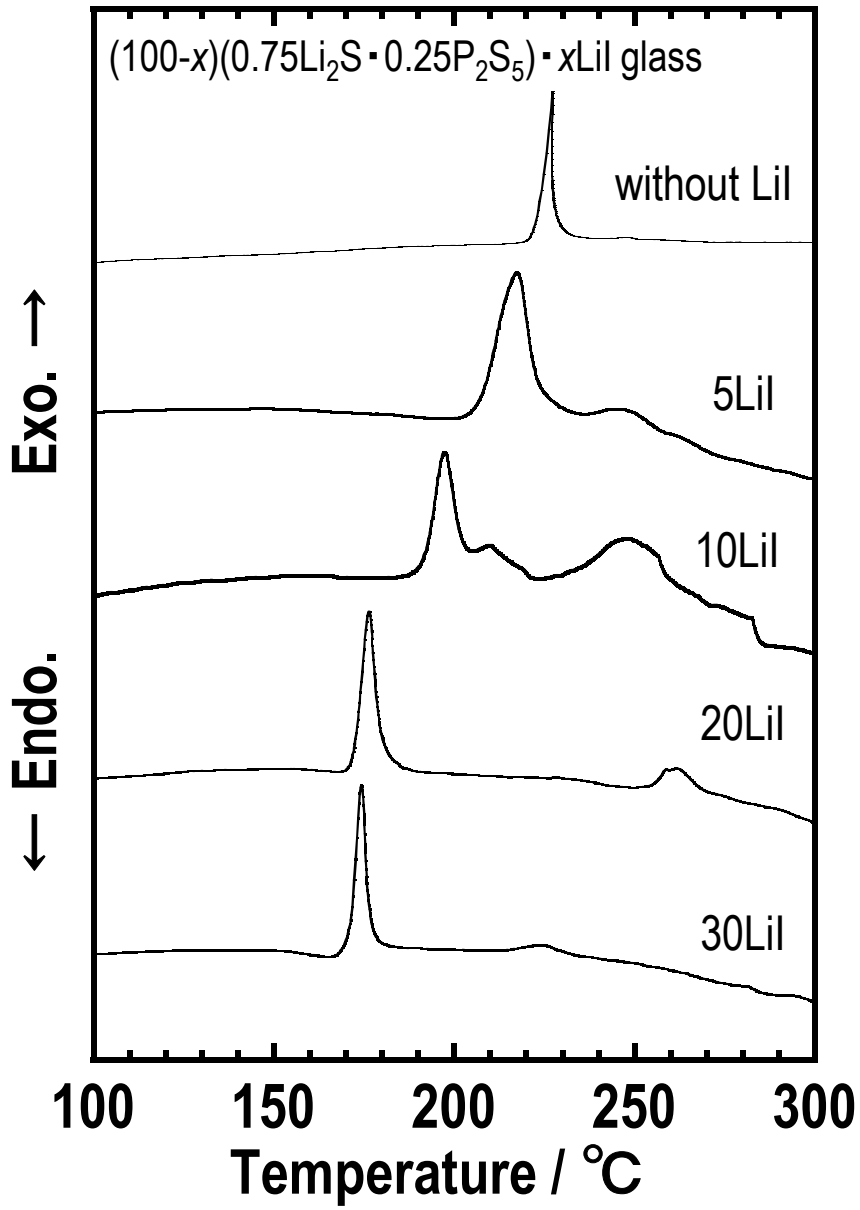

Fig. 2-3-7 DTA curves of $(100-x)(0.75Li_2S \cdot 0.25P_2S_5) \cdot xLiI$ (mol%) (y = 0, 5, 10, 20, and 30) glasses.

Table 2-3-4 The longitudinal velocity (V_L), shear velocity (V_S), density (ρ_{HP}), shear modulus (G), Young's modulus (E), bulk modulus (B),and Poisson's ratio (ν) of Li_2S-P_2S_5 glasses with lithium halides prepared by a hot press at various molding temperatures and pressures.

Sample	Molding temperature /°C	Molding pressure /MPa	V_L /m s^{-1}	V_S /m s^{-1}	ρ_{HP} /g cm^{-3}	G /GPa	E /GPa	B /GPa	ν	**Conductivity of cold-pressed pellets /S cm^{-1}
*75Li_2S·25P_2S_5	190	360	4,150	2,150	1.88	8.7	23	21	0.32	2.4 x 10^{-4}
95(0.75Li_2S·0.25P_2S_5)·5LiI	160	360	3,920	2,030	1.97	8.1	21	19	0.32	2.9 x 10^{-4}
90(0.75Li_2S·0.25P_2S_5)·10LiI	150	360	3,830	1,990	2.03	8.0	21	19	0.32	4.7 x 10^{-4}
80(0.75Li_2S·0.25P_2S_5)·20LiI	135	360	3,620	1,880	2.17	7.7	20	18	0.32	1.1 x 10^{-3}
70(0.75Li_2S·0.25P_2S_5)·30LiI	130	360	3,390	1,740	2.33	7.1	19	17	0.32	1.5 x 10^{-3}
67Li_2S·33P_2S_5	220	360	4,070	2,120	1.96	8.8	23	21	0.31	5.8 x 10^{-5}
67(0.67Li_2S·0.33P_2S_5)·33LiI	160	360	3,410	1,760	2.38	7.4	19	18	0.32	4.4 x 10^{-4}
*50Li_2S·50P_2S_5	230	360	3,390	1,910	1.89	6.9	18	13	0.27	<1 x 10^{-5}
75(0.50Li_2S·0.50P_2S_5)·25LiI	150	360	3,300	1,730	2.26	6.8	18	16	0.31	
70(0.50Li_2S·0.50P_2S_5)·30LiI	140	360	3,090	1,610	2.43	6.3	17	15	0.31	2.2 x 10^{-4}
LiI crystal	R.T.	540	2,910	1,640	3.92	10.6	27	19	0.27	
90(0.75Li_2S·0.25P_2S_5)·10LiBr	170	360	4,080	2,030	1.97	8.1	22	23	0.34	3.7 x 10^{-4}
80(0.75Li_2S·0.25P_2S_5)·20LiBr	160	360	4,020	2,010	2.04	8.2	22	22	0.33	9.2 x 10^{-4}
LiBr crystal	R.T.	540	3,690	2,110	3.42	15.2	38	27	0.26	
NaBr crystal	R.T.	540	3,440	1,930	3.11	11.6	29	21	0.27	
KBr crystal	R.T.	540	3,090	1,680	2.72	7.7	20	16	0.29	
90(0.75Li_2S·0.25P_2S_5)·10LiCl	170	360	4,060	2,040	1.87	7.8	21	20	0.33	

* Data from the reference [20]

** Cold press of solid electrolytes was conducted at room temperature under 360 MPa

ρ_{HP}: Density of pellets prepared by a hot press
G : Shear modulus
E : Young's modulus
K : Bulk modulus
ν : Poisson's ratio

halides are lower than those of ionic crystals, such as crystalline LiI or LiBr. The lower elastic moduli are related to the larger free volumes of the glasses [49]. The Young's moduli of glasses can be estimated from the bonding energy and the ion packing density [38]. Unfortunately, the bonding energies of $(100-y)(0.75Li_2S\cdot 0.25P_2S_5)\cdot yLiI$ glasses are not currently known. However, it can be theorised that the glasses might have lower bonding energies because the glass transition and crystallisation temperatures decrease upon LiI addition. The lower bonding energy could thus be one factor behind the Young's moduli of these glasses decreasing upon the addition of LiI. Further, the author calculates the mean atomic volumes [36] in order to estimate the ion packing densities. Fig. 2-3-8 shows the relationship between the mean atomic volumes and Young's moduli as a function of the composition of the $(100-x)(0.75Li_2S\cdot 0.25P_2S_5)\cdot xLiI$ glasses. The Young's moduli of these glasses decrease with increasing mean atomic volume. Moreover, the mean atomic volume increases with increasing the LiI content, indicating that the Li_2S-P_2S_5 glasses with LiI exhibit more open structures. The main anion in the $75Li_2S\cdot 25P_2S_5$ ($y = 0$) glass is PS_4^{3-}. Adding LiI to the $75Li_2S\cdot 25P_2S_5$ glass does not change the main structural unit of PS_4^{3-} anions in the glass network [50]. Therefore, I^- ions would increase the free volume and decrease the ion packing density in the glass structure owing to their relatively large size and high polarizability [51]. The decrease in ion packing density could be another factor behind the decrease in the Young's moduli of the Li_2S-P_2S_5 glasses upon the addition of LiI.

The formability of $(100-x)(0.75Li_2S\cdot 0.25P_2S_5)\cdot xLiI$ glasses was investigated by powder compaction. Fig. 2-3-9 shows the SEM images of the fracture cross-sections of the $(100-x)(0.75Li_2S\cdot 0.25P_2S_5)\cdot xLiI$ ($x = 0$, 30) glass pellets pressed at 360 MPa. It appears that the $x = 30$ glass has fewer pores and grain boundaries. The relative densities of the $x = 0$ and 30 pellets calculated from their powder densities (1.88 g cm^{-3} and 2.31 g cm^{-3}, respectively) are ca. 90% and 92%, respectively. The relative densities increase slightly upon the addition of LiI. It is noted that the powder compaction tests of the glasses were performed at room temperature, which is below the glass transition temperature. Sakuda *et al.* has reported that "room temperature pressure sintering" occurs for sulfide solid electrolytes in the powder

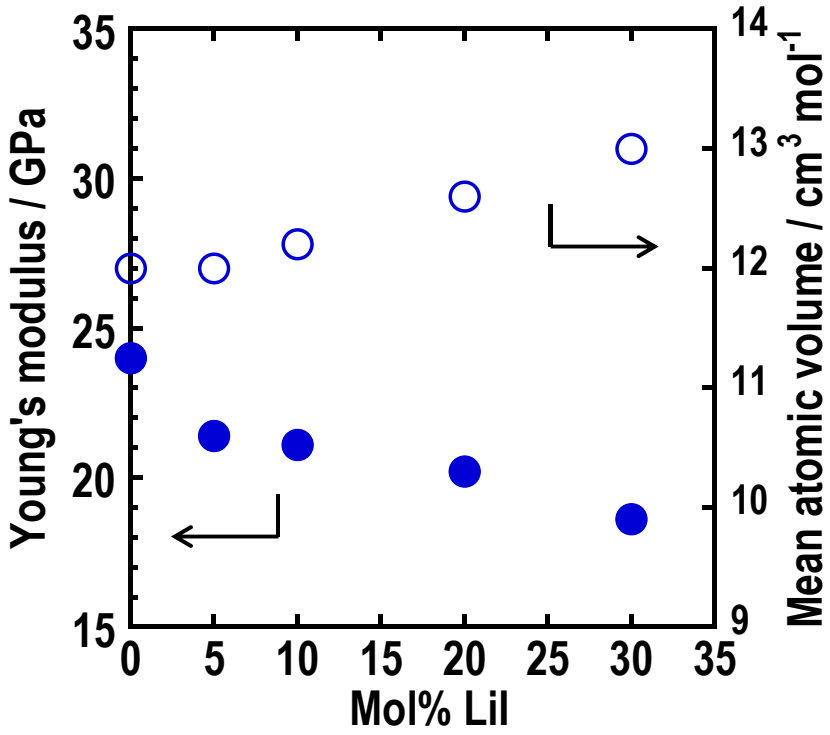

Fig. 2-3-8 Relationship between the Young's moduli and mean atomic volumes of $(100-x)(0.75Li_2S\cdot 0.25P_2S_5)\cdot xLiI$ (mol%) (x = 0, 5, 10, 20, and 30) glasses.

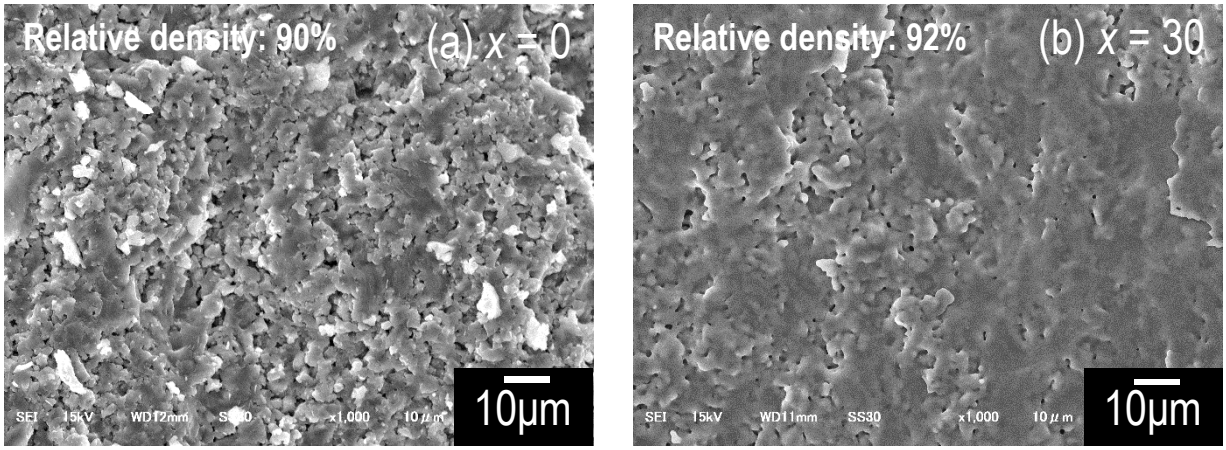

Fig. 2-3-9 SEM images of the cross-sections of $(100-x)(0.75Li_2S\cdot 0.25P_2S_5)\cdot xLiI$ glass pellets pressed at 360 MPa. (a) x = 0 mol% and (b) x = 30 mol%.

compaction test [21]. During the densification of the glass pellets (by the application of pressure at room temperature), it is assumed that lithium (Li^+), thiophosphate (PS_4^{3-}), and iodide (I^-) ions diffuse to the particle boundaries. LiI addition decreases the bonding energy of the Li_2S-P_2S_5 glasses, as indicated by the decrease in the glass transition temperature. In addition, the glass structures possess larger free volumes. These two factors would facilitate ion diffusion and rotation and bring about better densification in the $70(0.75Li_2S \cdot 0.25P_2S_5) \cdot 30LiI$ glass.

The electrical conductivities of Li_2S-P_2S_5 glasses increase upon the addition of lithium halides, as shown in Table 2-3-4. Low elastic moduli and high ionic conductivities can be obtained by adding lithium halides, especially LiI, to the Li_2S-P_2S_5 glasses. To investigate the effects of different mechanical properties of solid electrolytes on the electrochemical performance of all-solid-state cells, cells using Si composite electrodes with $75Li_2S \cdot 25P_2S_5$ and $70(0.50Li_2S \cdot 0.50P_2S_5) \cdot 30LiI$ glass electrolytes were fabricated. These two types of solid electrolytes exhibit almost similar electrical conductivities (10^{-4} S cm^{-1} at room temperature) but the $70(0.50Li_2S \cdot 0.50P_2S_5) \cdot 30LiI$ glass exhibits a lower Young's modulus (17 GPa) than the $75Li_2S \cdot 25P_2S_5$ glass (23 GPa). The charge-discharge curves during the initial cycle and the cycle performance of these cells are shown in Fig. 2-3-10. The cell using $70(0.50Li_2S \cdot 0.50P_2S_5) \cdot 30LiI$ glass electrolytes with low elastic moduli exhibits large capacities even after 20 cycles.

Several factors other than the elastic moduli of solid electrolytes may affect the cell performance. These cells had voids in the Si composite electrodes because they were fabricated by powder compaction at room temperature. Voids may exert both positive and negative influences on the cell performance. On the positive side, voids can accommodate the large strains generated by volume changes in Si. The formation of Li_xSi during Li insertion generates about 400% volume expansion [34]. Not only the solid electrolytes but also the voids undergo such large volume changes; the expanded voids can prevent the destruction of Si electrodes and contribute to the high capacities. On the negative side, the voids may prohibit Li-ion passes in Si composite electrodes. A decrease in the number of Li-ion passes

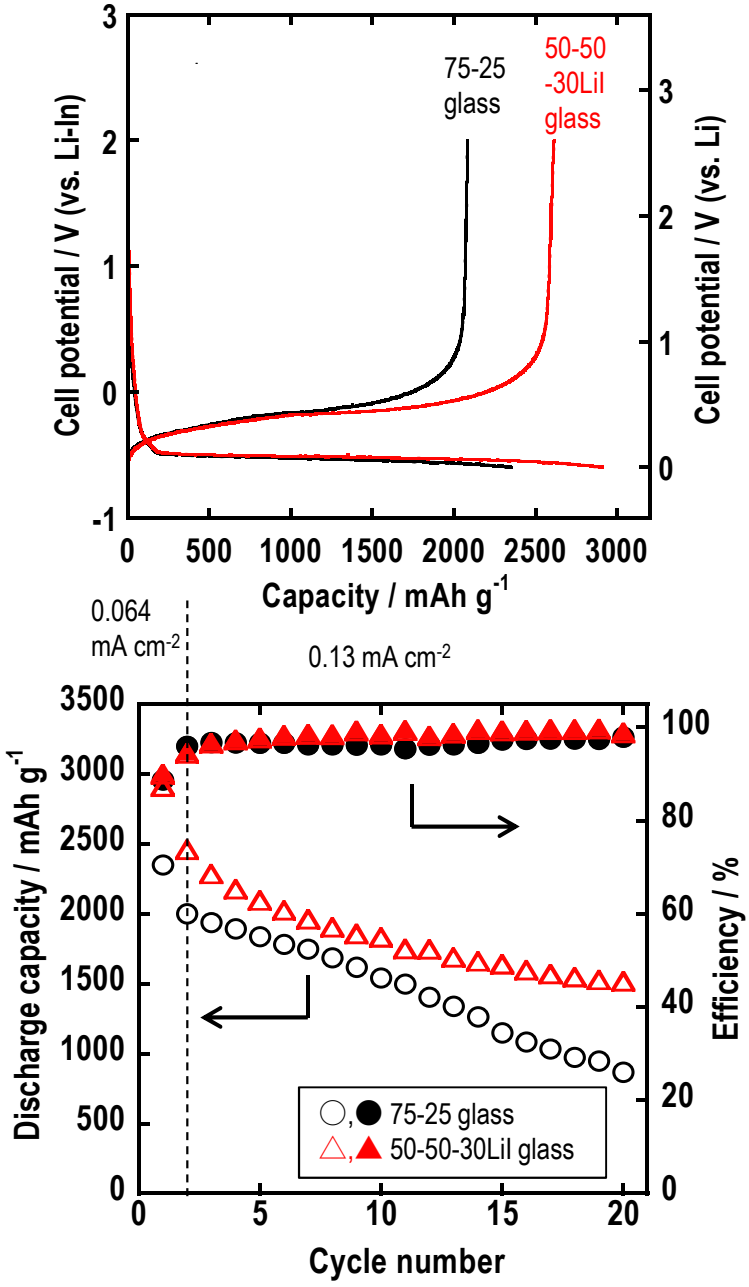

Fig. 2-3-10 Charge-discharge curves during the initial cycle and cycle performance of all-solid-state cells using Si composite electrodes containing $75Li_2S \cdot 25P_2S_5$ (75-25) and $70(0.50Li_2S \cdot 0.50P_2S_5) \cdot 30LiI$ (50-50-30LiI) glass electrolytes.

leads to non-uniform electrochemical reactions and results in capacity loss. The amount of voids in the Si composite electrodes has not been quantified, but the cell using $70(0.50Li_2S \cdot 0.50P_2S_5) \cdot 30LiI$ glass electrolytes would have a lesser number of voids because the formability of Li_2S-P_2S_5 glasses with LiI is expected to be high. Therefore, larger capacities may be obtained for the cell with $70(0.50Li_2S \cdot 0.50P_2S_5) \cdot 30LiI$ glass because of a greater number of Li-ion passes compared to the cell using $75Li_2S \cdot 25P_2S_5$ glass. It is suggested that the large strains induced by the volume changes in Si are mainly accommodated by the glass electrolyte.

Side reactions occurring at the electrode/electrolyte interface also affect the cell performance. The coulombic efficiencies of the cells using $75Li_2S \cdot 25P_2S_5$ and $70(0.50Li_2S \cdot 0.50P_2S_5) \cdot 30LiI$ glass electrolytes during the first cycle were 89% and 90%, respectively. It is well known that large irreversible capacity losses during the initial cycle are produced by the formation of a solid electrolyte interface (SEI). Son *et al.* reported the formation of an SEI layer during the lithiation of Si particles in all-solid-state cells [52]. However, after several cycles, both cells using $75Li_2S \cdot 25P_2S_5$ and $70(0.50Li_2S \cdot 0.50P_2S_5) \cdot 30LiI$ glass electrolytes maintained high coulombic efficiencies, respectively. Therefore, side reactions would not have a large effect on the cell performance in this case.

As stated above, many factors affect the cell performance. However, the elastic modulus of solid electrolytes is one of the predominant parameters that should be considered. Glass electrolytes with lower elastic moduli can accommodate larger strains generated by the volume changes in Si, and thus these electrolytes will be effective in suppressing the destruction of electrode particles and retaining the interface between the electrodes and electrolytes. Lithium metal negative electrodes also exhibited a large volume change during the dissolution and deposition reactions. It is expected to suppress the dendrite growth using glass electrolytes with a lower elastic modulus.

2.3.3 Mechanical properties of element substituted Li_2S-P_2S_5 glasses and their comparison with oxide and other chalcogenide glasses

Ion-conducting glasses are composed of the glass former and modifier. In this section, effects by changing them in Li_2S-P_2S_5 glasses on the mechanical properties were investigated. Elastic moduli of Li_2S-P_2S_5 glasses where P_2S_5 is totally or partially replaced by the other glass former and ones where sulfur is totally or partially replaced by oxygen are also shown in Table 2-3-5. Relationship between the Young's moduli and mean atomic volume is displayed in Fig. 2-3-11. Young's moduli of Li_2S-SiS_2 and Li_2S-GeS_2 glasses are higher than those of Li_2S-P_2S_5 glasses. On the other hand, the mean atomic volume of $50Li_2S \cdot 50SiS_2$ glass is smaller than that of $50Li_2S \cdot 50P_2S_5$ glass. Comparing the ortho-compositions, $67Li_2S \cdot 33GeS_2$ glass has a smaller mean atomic volume than that of $75Li_2S \cdot 25P_2S_5$ glass. In addition, Young's moduli of Li_3PS_4-Li_4GeS_4 glasses increase with an increase in the Ge content, while the mean atomic volumes of Li_3PS_4-Li_4GeS_4 glasses decrease with an increase in the Ge content. It seems that the Young's moduli of these glasses roughly have the negative correlation with the mean atomic volumes. The Young's moduli of oxygen-substituted Li_2S-P_2S_5-P_2O_5 and Li_2O-Li_2S-P_2S_5 glasses also have the same relationship with the mean atomic volumes. Of course, the Young's -moduli are also affected by the bond dissociation energies (P-S: 442 kJ mol^{-1}, Ge-S: 534 kJ mol^{-1}, Si-S: 617 kJ mol^{-1}, P-O: 589 kJ mol^{-1}) [44] in addition to the mean atomic volumes. The bond dissociation energies of Ge-S, Si-S, and P-O bonds are larger than that of P-S bond, corresponding to the increase in the Young's moduli.

Table 2-3-6 also shows the elastic moduli of Li_2S-P_2S_5 glasses where Li_2S is fully replaced by other sulfide-modifiers such as: Na_2S, Ag_2S, SnS, and MgS. Their Young's moduli increase with an increase in each modifier content, while the mean atomic volumes decrease upon the addition of their modifiers (Fig. 2-3-12). On the other hand, negative correlation between the Young's moduli and mean atomic volumes was observed in the meta-composition (denoted as 50-50 in Fig. 2-3-12) except for Sn. Since the boding dissociation energies are reported as Li-S: 313 kJ mol^{-1}, Na-S: no data, Ag-S: 217 kJ mol^{-1}, Sn-S: 467 kJ mol^{-1}, and Mg-S: 234 kJ mol^{-1} [44], the relatively higher bond dissociation

Table 2-3-5 The longitudinal velocity (V_L), shear velocity (V_S), density (ρ_{HP}), shear modulus (G), Young's modulus (E), bulk modulus (B),and Poisson's ratio (ν) of hot-pressed bodies of Li_2S-P_2S_5 glasses where P_2S_5 is totally or partially replaced by the other glass former and ones where S is totally or partially replaced by O. Molding temperatures and pressures to prepare the hot-pressed bodies are also indicated in the Table. The relative density was calculated from the powder density (ρ_0) of milled glasses.

Sample	Powder density (ρ_0) /g cm^{-3}	Molding condition Temperature /ºC	Time /h	Pressure /MPa	Hot-press density (ρ_{HP}) /g cm^{-3}	Relative density /%	V_L /ms^{-1}	V_s /ms^{-1}	G /GPa	E /GPa	ν	B /GPa
*$50Li_2S{\cdot}50P_2S_5$	2.00	(230)	-	(360)	(1.89)	94.4	(3390)	(1910)	(6.9)	(17.5)	(0.27)	(12.5)
$67Li_2S{\cdot}33P_2S_5$	1.95	200	4	360	1.95	100	4040	2070	8.4	22.1	0.32	20.7
*$70Li_2S{\cdot}30P_2S_5$	1.92	(240)	-	(360)	(1.91)	99.6	(4020)	(2090)	(8.3)	(21.9)	(0.31)	(19.7)
*$75Li_2S{\cdot}25P_2S_5$	1.88	(190)	-	(360)	(1.88)	99.9	(4150)	(2150)	(8.7)	(22.9)	(0.32)	(20.8)
$50Li_2S{\cdot}50SiS_2$	1.94	310	4	360	1.84	95.1	4770	2540	11.9	31.0	0.30	26.1
$60Li_2S{\cdot}40GeS_2$	-	220	4	360	2.20	-	4120	2170	10.3	27.1	0.31	23.5
$67Li_2S{\cdot}33GeS_2$	-	205	4	360	2.15	-	4170	2230	10.7	27.8	0.30	23.1
$25Li_3PS_4{\cdot}75Li_4GeS_4$	-	215	4	360	2.13	-	4260	2230	10.6	27.7	0.31	24.5
$50Li_3PS_4{\cdot}50Li_4GeS_4$	-	205	4	360	2.06	-	4300	2200	10.0	26.3	0.32	24.8
$75Li_3PS_4{\cdot}25Li_4GeS_4$	-	195	4	360	1.98	-	4200	2140	9.1	24.0	0.32	22.8
$70Li_2S{\cdot}27P_2S_5{\cdot}3P_2O_5$	-	200	4	360	1.95	-	4230	2160	9.1	24.1	0.32	22.7
$70Li_2S{\cdot}20P_2S_5{\cdot}10P_2O_5$	-	230	4	360	1.99	-	4280	2260	10.2	26.6	0.31	22.9
$10Li_2O{\cdot}60Li_2S{\cdot}30P_2S_5$	-	210	4	360	1.94	-	4110	2140	8.9	23.3	0.31	20.9
$20Li_2O{\cdot}50Li_2S{\cdot}30P_2S_5$	-	210	4	360	1.95	-	4130	2160	9.1	23.8	0.31	21.1

* Data from the reference [20].

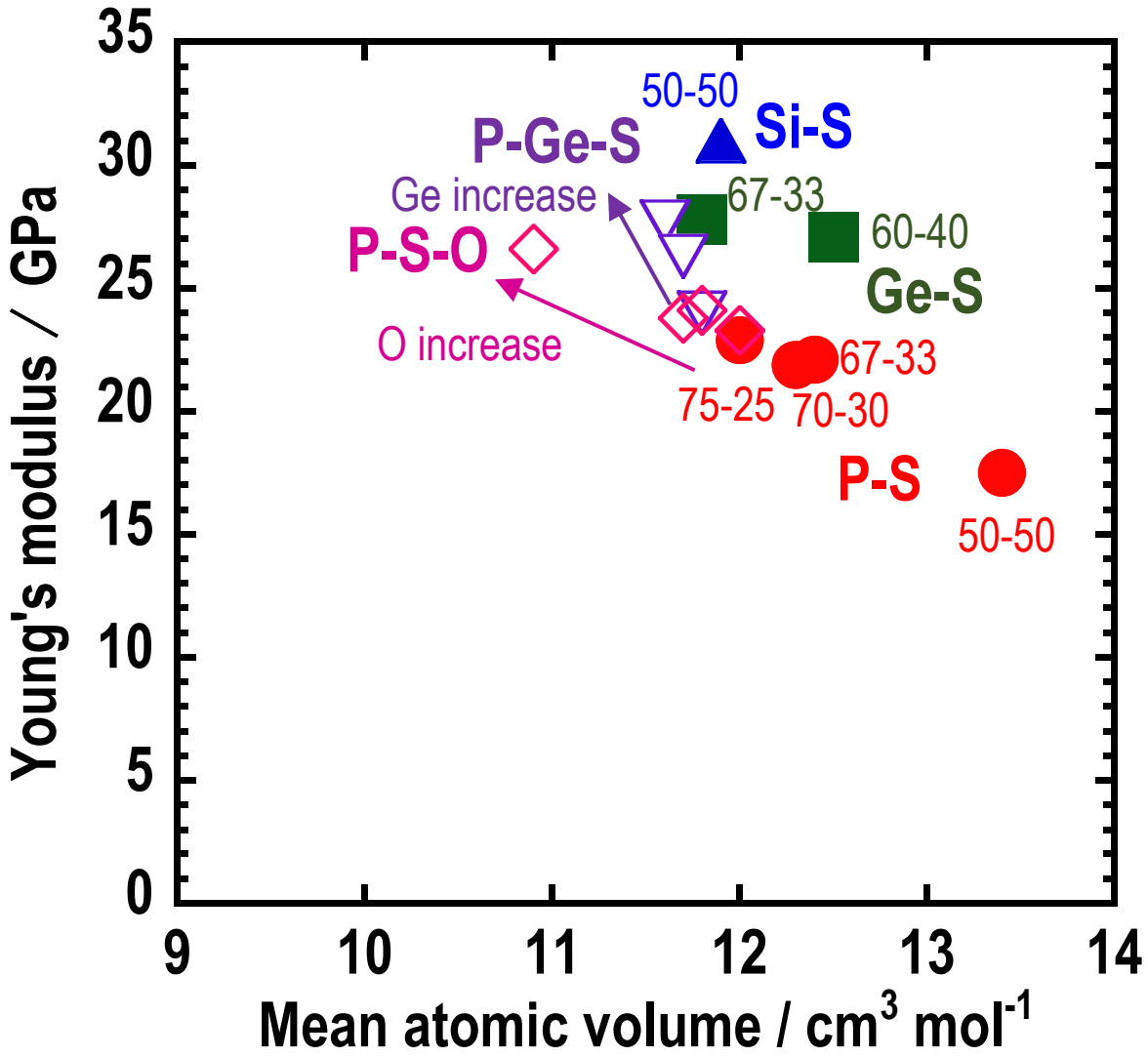

Fig. 2-3-11 Relationship between Young's moduli and mean atomic volumes of the Li_2S-P_2S_5 glasses where P_2S_5 is totally or partially replaced by the other glass formers, and Li_2S-P_2S_5 glasses where S is totally or partially replaced by O: Li_2S-P_2S_5, Li_2S-SiS_2, Li_2S-GeS_2, Li_3PS_4-Li_4GeS_4; and Li_2S-P_2S_5-P_2O_5 and Li_2O-Li_2S-P_2S_5. The molar ratios of the glasses are also shown (e.g., P-S:75-25 = $75Li_2S \cdot 25P_2S_5$ (mol%)).

Table 2-3-6 The longitudinal velocity (V_L), shear velocity (V_S), density (ρ_{HP}), shear modulus (G), Young's modulus (E), bulk modulus (B),and Poisson's ratio (ν) of hot-pressed bodies of Li_2S-P_2S_5 glasses where Li_2S is fully replaced by other sulfide-modifiers such as: Na_2S, Ag_2S, SnS, and MgS. Molding temperatures and pressures to prepare the hot-pressed bodies are also indicated in the table. The relative density was calculated from the powder density (ρ_0) of milled glasses.

Sample	Powder density /g cm^{-3}	Molding condition			Hot press density (ρ_{HP}) /g cm^{-3}	Relative density /%	V_L /ms^{-1}	V_s /ms^{-1}	G /GPa	E /GPa	ν	B /GPa
		Temperature /°C	Time /h	Pressure /MPa								
$50Na_2S{\cdot}50P_2S_5$	2.07	180	4	270	2.05	99.2	3280	1640	5.5	14.7	0.33	14.7
$67Na_2S{\cdot}33P_2S_5$	2.03	190	4	360	2.01	99.0	3830	1860	7.0	18.7	0.35	20.2
$75Na_2S{\cdot}25P_2S_5$	2.00	170	4	360	1.98	98.9	3890	1900	7.1	19.2	0.34	20.4
$50Ag_2S{\cdot}50P_2S_5$	3.40	180	4	360	3.43	100.9	2620	1430	7.0	18.0	0.29	14.2
$50SnS{\cdot}50P_2S_5$	2.72	190	4	270	2.55	93.8	2960	1550	6.1	16.1	0.31	14.2
$67SnS{\cdot}33P_2S_5$	3.19	190	4	270	3.01	94.3	2770	1510	6.9	17.7	0.29	13.9
$75SnS{\cdot}25P_2S_5$	3.47	200	4	270	3.46	99.7	3000	1570	8.5	22.4	0.31	19.8
$50MgS{\cdot}50P_2S_5$	2.08	R.T.	2	800	1.98	95.5	2650	1570	4.9	12.0	0.23	7.4

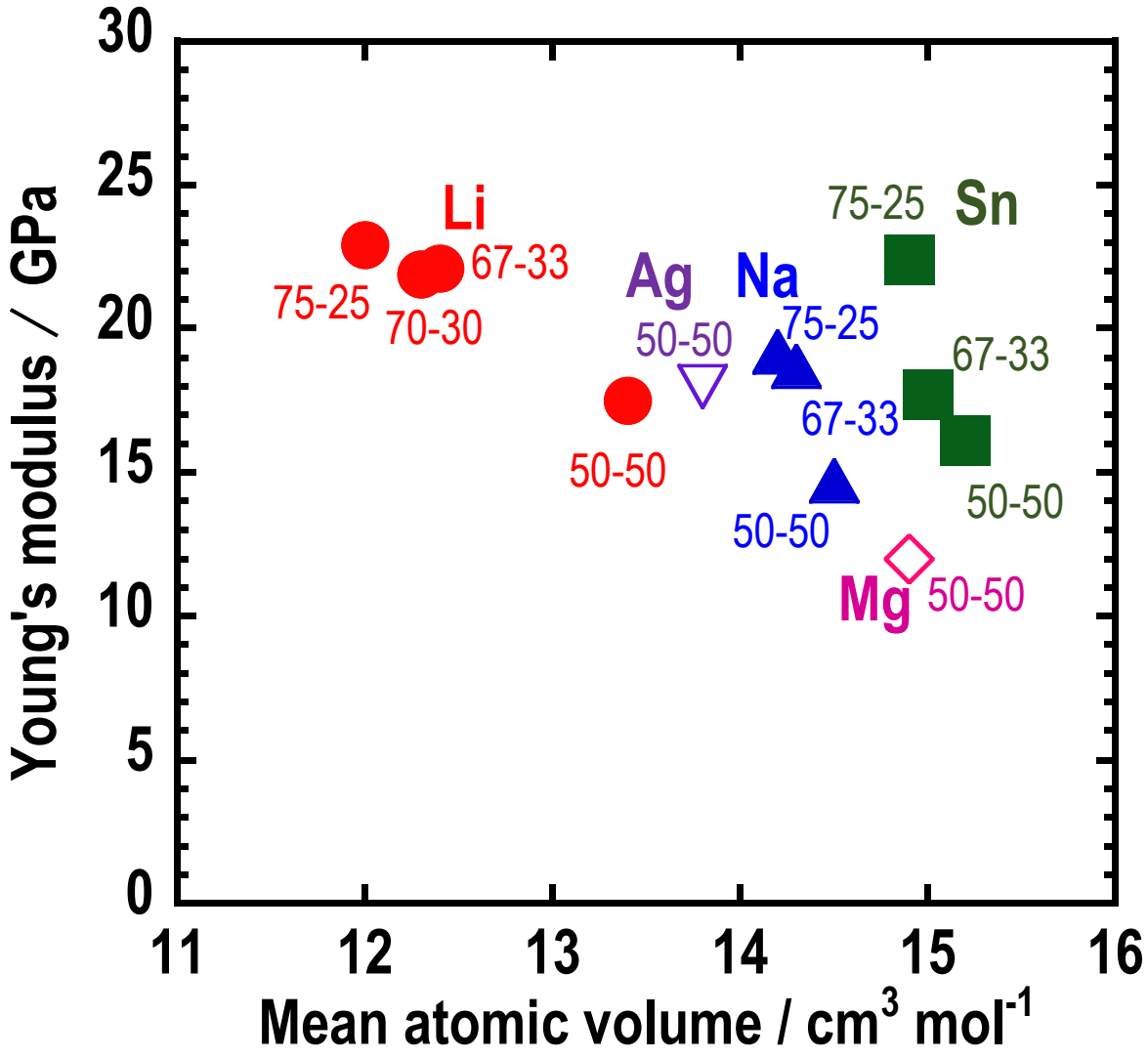

Fig. 2-3-12 Relationship between Young's moduli and mean atomic volumes of the Li_2S-P_2S_5 glasses where Li_2S is fully replaced by other sulfide-modifiers such as: Na_2S (Na_2S-P_2S_5), Ag_2S (Ag_2S-P_2S_5), SnS (SnS-P_2S_5), and MgS (MgS-P_2S_5).

energies of Sn-S bonds might increase Young's moduli.

Young's moduli of Li_2S-P_2S_5-based glasses studied here are summarized in Fig. 2-3-13 along with those of previously reported oxide [53–58] and other chalcogenide glasses [59–61]. In general, there is a good correlation between Young's moduli and mean atomic volumes. Oxide glasses (the orange, green, and gray areas) have higher Young's moduli and smaller mean atomic volumes. Already reported chalcogenide glasses (the purple area) have lower Young's moduli and larger mean atomic volumes. The sulfide glasses studied here (the blue area) are placed in the intermediate region between the oxide and other chalcogenide glasses.

Next, formability of these sulfide glasses was investigated by powder-compaction tests. The bulk density and relative density of the cold-pressed Li_2S-P_2S_5 glasses where P_2S_5 is replaced by the other glass former and those where S is replaced O are listed in Table 2-3-7. The highest relative density in the system Li_2S-GeS_2 is obtained at 67 mol% of the Li_2S content (ortho-composition) and the lowest is at 50 mol% (meta-composition); a similar trend is observed in the Li_2S-P_2S_5 glasses. On the other hand, the relative densities become smaller by changing the cations of a glass former from P to Ge or Si in $50Li_2S \cdot 50M_xS_y$ (M = P, Ge, Si) glasses. Furthermore, the relative densities of Li_4PS_4-Li_4GeS_4 glasses decreases with an increase in the Ge content. As shown in Fig. 2-3-14, SEM images of fracture cross section of the cold-pressed pellets (at 360 MPa) reveal that the amounts of voids and grain boundaries increase with an increase in the Ge content. There are two factors to be considered for the difference of formability among glass-forming cations: the glass network connectivity and the mean atomic volume. The number of sulfur for cross-linking is three for P (P is fourfold coordinated to sulfur, but a P = S bond is not involved in the connection in the glass network), and it is four for Ge or Si. In addition, P-S bonds have more covalent character than Ge-S or Si-S bonds. Thus, it is assumed that isolated structures are formed more preferably in the glass containing P as the glass former cation. The isolated structure can facilitate the densification by pressure. In addition, Li_2S-P_2S_5 glasses have larger mean atomic volumes than those of Li_2S-GeS_2 and the Li_2S-SiS_2 glasses, indicating that the Li_2S-P_2S_5 glasses have a larger free volume in the glass structure. The larger free volume will be the other important factor for the

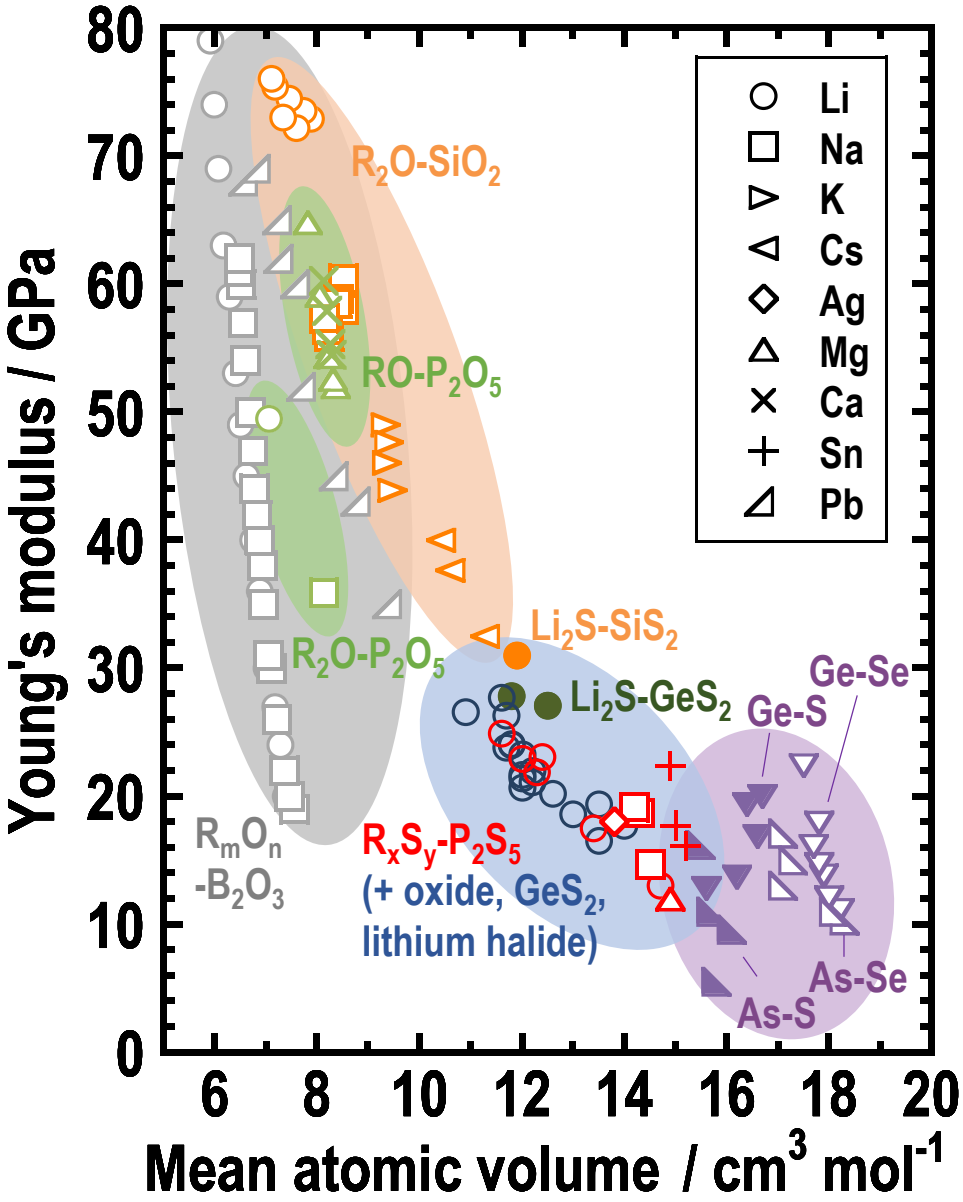

Fig. 2-3-13 Relationship between mean atomic volume and Young's modulus for newly measured Li_2S-P_2S_5-based glasses (blue-circled region) and other silicate (orange-circled region) [53], phosphate (green-circled region) [54,55], borate (gray-circled region) [56-58], chalcogenide (purple-circled region) [59-61] glasses.

Table 2-3-7 Bulk density and relative density of cold-pressed pellets of Li_2S-P_2S_5 glasses where P_2S_5 is totally or partially replaced by the other glass former and ones where S is totally or partially replaced by O. The relative density was calculated from the powder density or density of hot-pressed bodies.

Glass composition / mol%	Cold-press density at 360 MPa (ρ_{bulk}) / g cm^{-3}	Relative density / %
$50Li_2S \cdot 50P_2S_5$	1.70	85.0
$50Li_2S \cdot 50SiS_2$	1.94	75.7
$50Li_2S \cdot 50GeS_2$	1.40	(76)
$60Li_2S \cdot 40GeS_2$	1.79	(81)
$67Li_2S \cdot 33GeS_2$	1.78	(83)
$25Li_3PS_4 \cdot 75Li_4GeS_4$	1.75	(82)
$50Li_3PS_4 \cdot 50Li_4GeS_4$	1.72	(83)
$75Li_3PS_4 \cdot 25Li_4GeS_4$	1.71	(86)
$70Li_2S \cdot 20P_2S_5 \cdot 10P_2O_5$	1.65	(83)
$50Li_2O \cdot 50P_2O_5$	1.70	72.2

* Parentheses indicates the relative density calculated using the density of the hot-pressed pellet.

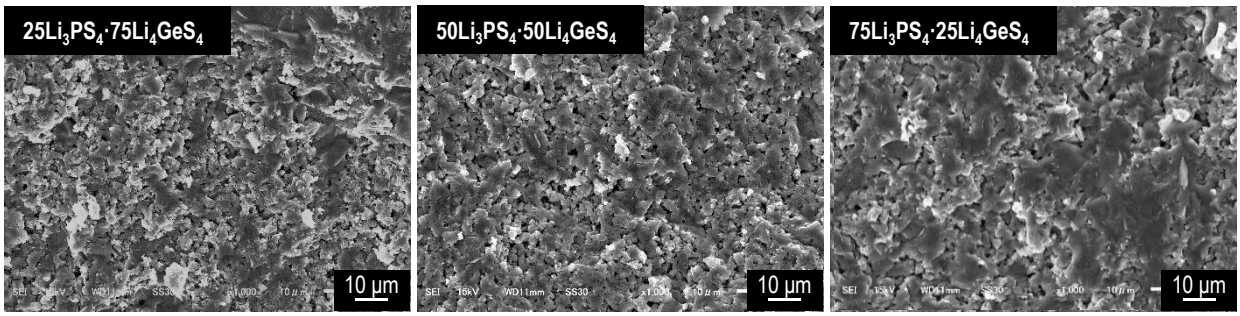

Fig. 2-3-14 Cross-sectional SEM images of cold-pressed pellets (at 360 MPa) of $x\mathrm{Li_3PS_4}\cdot(100\text{-}x)\mathrm{Li_4GeS_4}$ (x = 25, 50, 75 mol%) glasses.

densification. On the other hand, replacing S with O in the Li_2S-P_2S_5 glasses decreases the relative density of the glasses, as indicated in Table 2-3-7. The formability is obviously different between $50Li_2S \cdot 50P_2S_5$ sulfide and $50Li_2O \cdot 50P_2O_5$ oxide glasses as shown in the cross-sectional SEM images of powder-compressed bodies after cold-pressing at 360 MPa (Fig. 2-3-15). It is assumed that oxide glasses have more rigid glass network because the bonding dissociation energies of oxide glasses are higher than that of sulfide glasses (P-S: 442 kJ mol^{-1}, Li-S: 313 kJ mol^{-1}, P-O: 589 kJ mol^{-1}, Li-O: 341 kJ mol^{-1}) [44]. In addition, the mean atomic volumes decrease by replacing S with O, as shown in Fig. 2-3-11; thus, the rigid structure with a smaller free volume of oxide glasses may disturb the densification by pressure.

The relative densities of Li_2S-P_2S_5 glasses where Li_2S is replaced by the other sulfide-modifiers after cold-pressing at 360 MPa are shown in Table 2-3-8. The relative density increases with an increase in the contents of glass modifiers as shown in Fig 2-3-16. As for Li_2S-P_2S_5 glasses, it is considered that increasing the isolated ion structure contributes to an increase in the relative density in the systems Na_2S-P_2S_5 and SnS-P_2S_5. The relative density of Na_2S-P_2S_5 glasses is larger than that of Li_2S-P_2S_5 glasses. SEM images of cross sections of the cold-pressed pellets for the $75Na_2S \cdot 25P_2S_5$ and $75Li_2S \cdot 25P_2S_5$ glasses prepared by Ar ion-milling are shown in Fig. 2-3-17. The $75Na_2S \cdot 25P_2S_5$ glass has fewer pores and grain boundaries than the $75Li_2S \cdot 25P_2S_5$ glass. The densification will be prevented if the interaction between the cation of the glass modifier and S is stronger. The strength of interaction between the cation of the glass modifier and S is estimated as the cation field strength (Z/r^2; Z: cation charge, r: cation radius) [62]. In Fig. 2-3-18, the relative densities of $50R_xS_y \cdot 50P_2S_5$ glasses (R = Li, Na, Ag, Mg) are plotted based on the difference of the cation field strength. The relative density of $50SnS \cdot 50P_2S_5$ glass is excluded in the plots because the ionic radius of Sn^{2+} is not well defined because of its irregular coordination [63]. The relative densities of $50R_xS_y \cdot 50P_2S_5$ glasses decrease upon the increase with the cation field strength except for the $50Ag_2S \cdot 50P_2S_5$ glass. The Ag-S bond has more covalent character than the other R-S bonds, which might interfere with the densification.

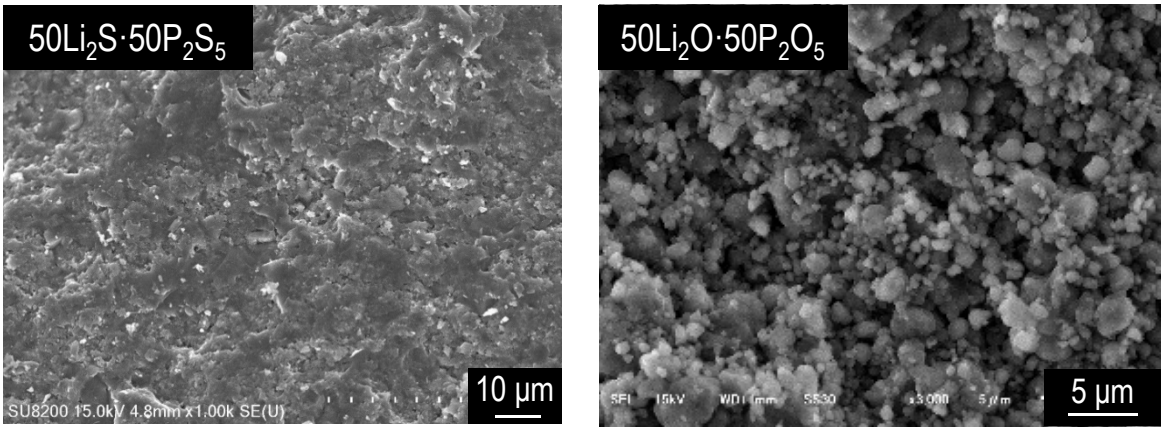

Fig. 2-3-15 Cross-sectional SEM images of cold-pressed pellets (at 360 MPa) of $50Li_2S \cdot 50P_2S_5$ and $50Li_2O \cdot 50P_2O_5$ (mol%) glasses.

Table 2-3-8 Bulk density and relative density of cold-pressed pellets of Li_2S-P_2S_5 glasses where Li_2S is replaced by other sulfide-modifiers such as: Na_2S, Ag_2S, SnS, and MgS. The relative density was calculated from the powder density or hot-press density.

Glass composition / mol%	Cold-press density @360 MPa (ρ_{bulk}) / g cm^{-3}	Relative density / %
$50Na_2S \cdot 50P_2S_5$	1.90	92.0
$67Na_2S \cdot 33P_2S_5$	1.90	93.7
$75Na_2S \cdot 25P_2S_5$	1.88	94.1
$50Ag_2S \cdot 50P_2S_5$	2.87	84.5
$50SnS \cdot 50P_2S_5$	2.24	82.4
$67SnS \cdot 33P_2S_5$	2.65	83.1
$75SnS \cdot 25P_2S_5$	3.01	86.8
$50MgS \cdot 50P_2S_5$	1.63	78.3

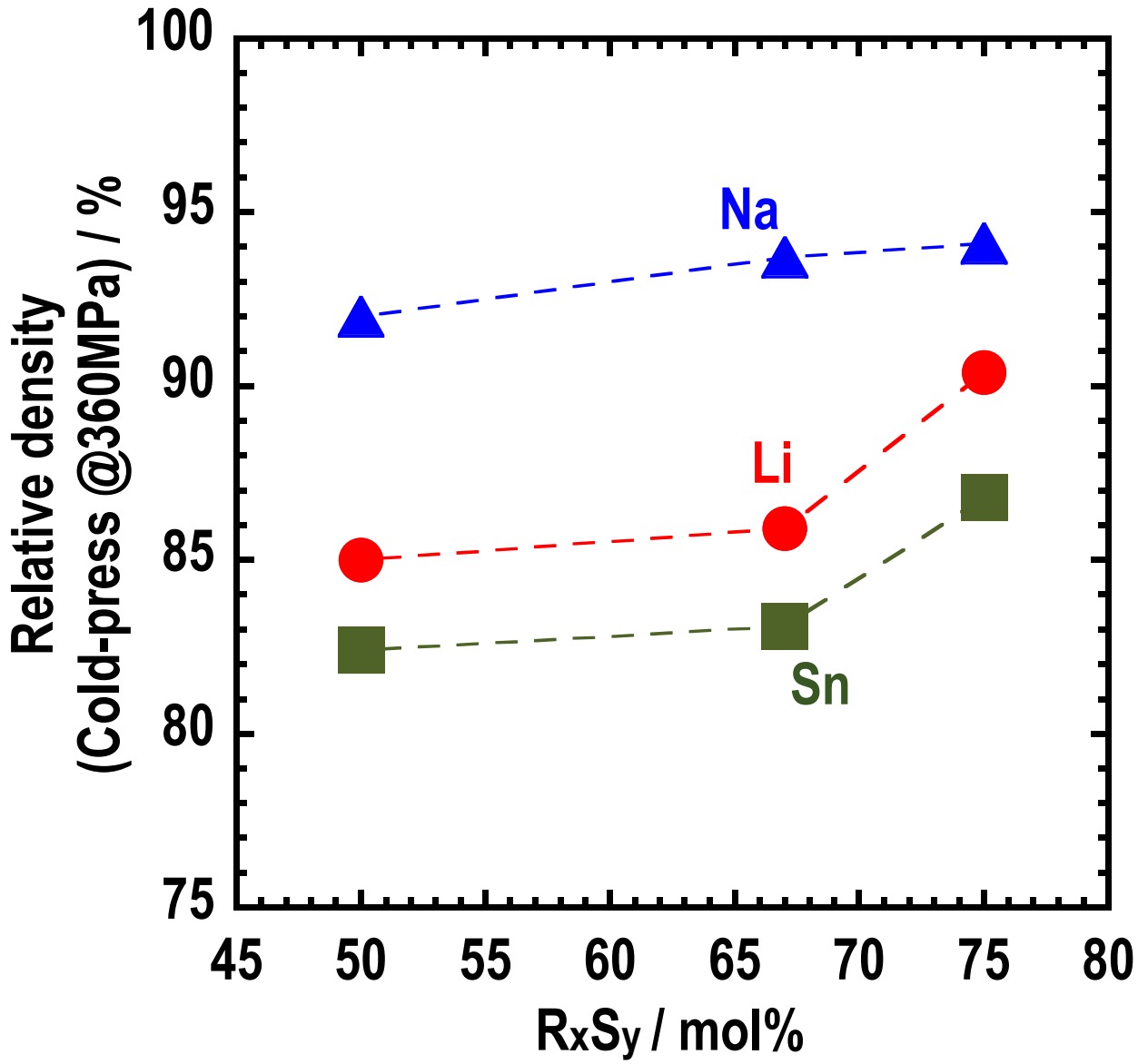

Fig. 2-3-16 Compositional dependence of the relative densities of the pellets of Li_2S-P_2S_5 glasses cold-pressed at 360 MPa, where Li_2S is fully replaced by other sulfide-modifiers such as Na_2S (Na_2S-P_2S_5) and SnS (SnS-P_2S_5).

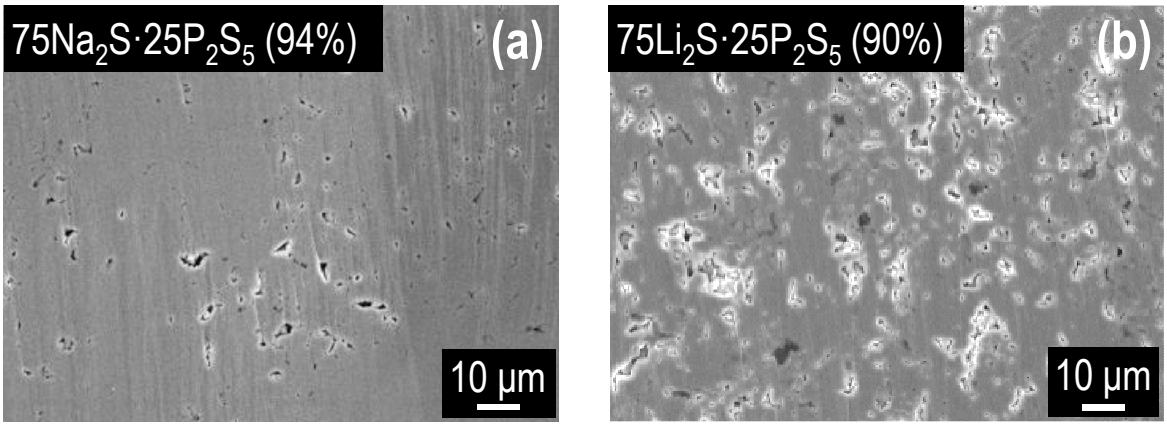

Fig. 2-3-17 SEM images of cross sections of (a) $75Na_2S \cdot 25P_2S_5$ and (b) $75Li_2S \cdot 25P_2S_5$ glasses pellets prepared by Ar ion-milling. Molding pressure was 360 MPa. The relative densities are indicated in the insets.

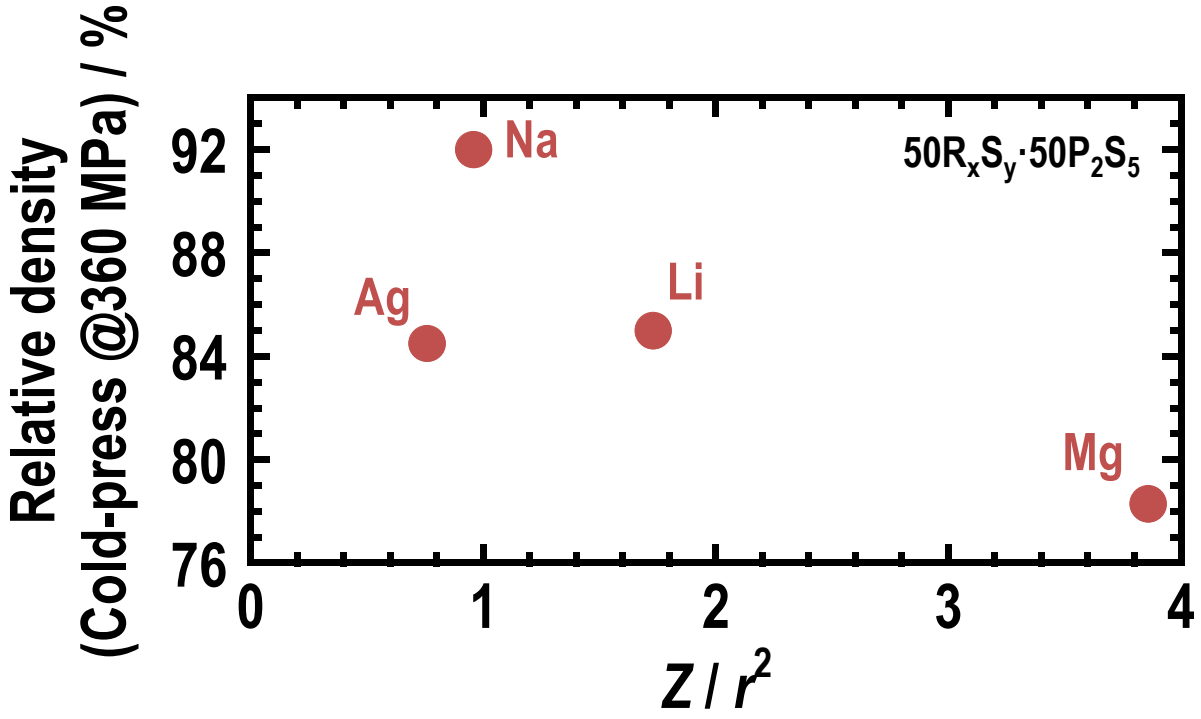

Fig. 2-3-18 Relationship between cation field strength (Z/r^2; Z: cation charge, r: cation radius) and relative density of cold-pressed pellets (at 360 MPa) of the $50R_xS_y \cdot 50P_2S_5$ glasses (R = Li, Na, Ag, Mg). The cation radii were retrieved from the literature [44].

Pugh's ratio (*B*/*G*) (*B* is the bulk and *G* the shear modulus) are used as ductile-brittle evaluation parameters of the materials [64] and are applied to solid electrolytes [65,66]. It is assumed that ductile-brittle properties affect the densification of the glasses in powder-compaction tests. The relationship between *B*/*G* and the relative density of Li_2S-P_2S_5-based glasses in powder-compaction tests are shown in Fig. 2-3-19. The glass with a larger *B*/*G* ratio, meaning higher ductility, tends to display a higher relative density. The powder-compaction tests were carried out at the high pressure (360 MPa) and at room temperature, which is below glass transition temperatures. It is considered that fracturing or plastic deformation of the particles are the main process for the densification in the powder-compaction tests [47]. It is assumed that the more brittle materials are densified by fracturing and the more ductile materials are densified by plastic deformation. Thus, the results in Fig. 2-3-19 may suggest that plastic deformation contributes to the densification of these glasses. It is noted that the lower bonding energy, the larger free volume, and the more isolated structure of sulfide glasses lead to superior mechanical properties.

2.4. Summary

Mechanical properties of Li_2S-P_2S_5-based glasses were investigated in this chapter. At first, the elastic moduli and formability of Li_2S-P_2S_5 glasses were evaluated. Young's moduli of Li_2S-P_2S_5 glasses increased with an increase in the Li_2S content. The addition of Li_2S transformed local structure from chain to isolated structure. It is suggested that the more isolated structure increased the ion packing density and led to an increase of the Young's moduli. In addition, $75Li_2S \cdot 25P_2S_5$ (mol%) glasses composed of Li^+ and PS_4^{3-} ions, which is the most isolated structure in Li_2S-P_2S_5 glasses, exhibited better densification by pressure. Difference in formability between Li_2S-P_2S_5 glasses, glass-ceramics, and crystals were also evaluated. The glasses showed higher densification with few grain boundaries than the crystalline ones because of the isotropic structure with the free volume. The few grain boundaries in the glass are critical for the use of Li metal negative electrodes because Li dendrites are likely to propagate through the grain boundaries.

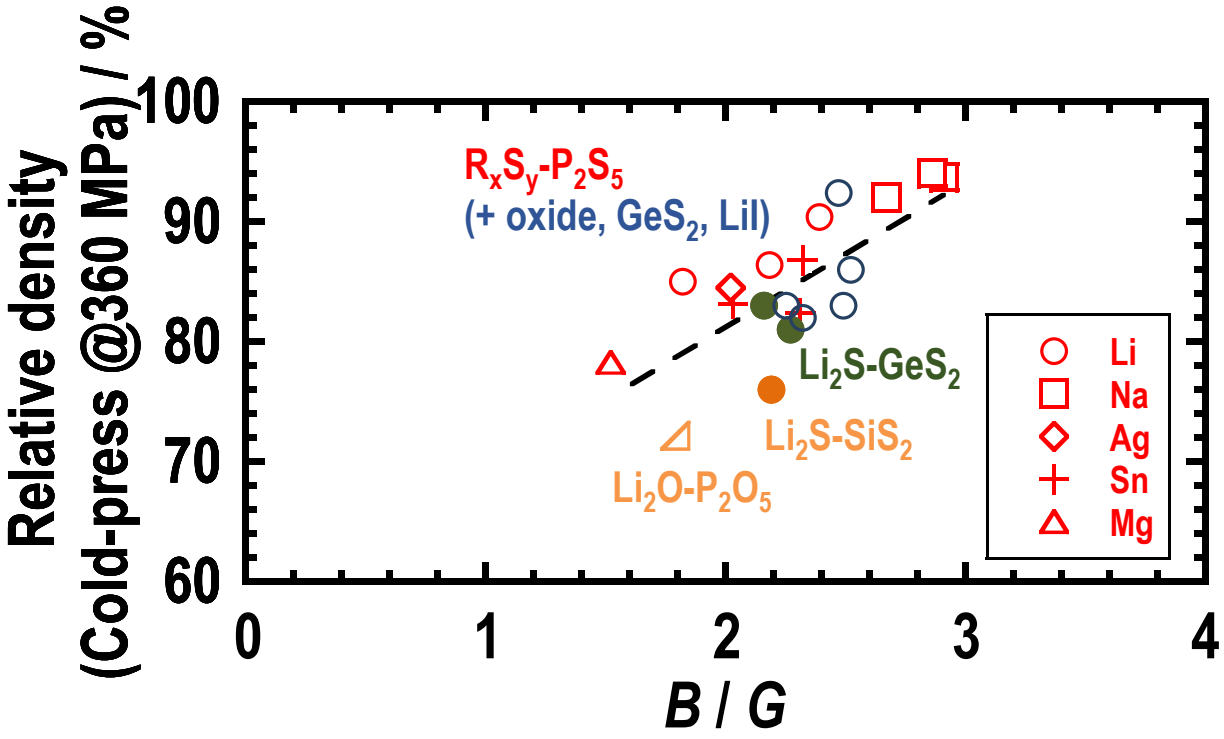

Fig. 2-3-19 Relationship between the ratio of bulk modulus (B) to shear modulus (G) and relative density of the Li_2S-P_2S_5-based and Li_2O-P_2O_5 glasses after cold-pressing at 360 MPa. The B/G ratio of Li_2O-P_2O_5 glasses was calculated using data retrieved from the literature [54].

Secondly, the mechanical properties of Li_2S-P_2S_5-LiX (X = I, Br, and Cl) glass electrolytes were investigated. The Young's moduli of the glass electrolytes were found to decrease upon the addition of lithium halides. In particular, LiI addition to the $75Li_2S \cdot 25P_2S_5$ glass gradually decreased its Young's modulus from 23 GPa to 19 GPa. The electrical conductivities of Li_2S-P_2S_5 glasses increased upon the addition of lithium halides. At the same time, both lower elastic moduli and higher ionic conductivities can be obtained. The performance of the all-solid-state cells using Si composite electrodes was compared with $75Li_2S \cdot 25P_2S_5$ and $70(0.50Li_2S \cdot 0.50P_2S_5) \cdot 30LiI$ glass electrolytes, which exhibited similar electrical conductivities but different Young's moduli. The cell with $70(0.50Li_2S \cdot 0.50P_2S_5) \cdot 30LiI$ glass electrolytes, which exhibited lower Young's moduli, exhibited larger capacities over 20 cycles. Therefore, it can be concluded that Li_2S-P_2S_5-LiI glasses with superior mechanical properties, such as lower Young's modulus and better formability, would exhibit better cell performance. Li metal negative electrodes also exhibited a large volume change during the dissolution and deposition reactions. It is expected to suppress the dendrite growth using the glass electrolytes with a lower elastic modulus.

Thirdly, the mechanical properties of element substituted Li_2S-P_2S_5 glasses were evaluated and compared with oxide and other chalcogenide glasses. The Young's moduli of the Li_2S-P_2S_5 glasses increased when replacing the glass former of P_2S_5 with GeS_2 or SiS_2. The Young's moduli also increased by substituting S with O. In addition, the elastic moduli of Li_2S-P_2S_5 glasses where Li_2S is fully replaced by other sulfide-modifiers of Na_2S, Ag_2S, SnS, and MgS were investigated. The Young's moduli of these glasses increased with an increase in the content of each modifier. Young's moduli studied here were summarized from the viewpoint of the mean atomic volumes. A good correlation between Young's moduli and mean atomic volumes was found in the sulfide glasses as well as oxide and other chalcogenide glasses. Formability of these sulfide glasses was investigated on the basis of the relative density of the powder-compressed pellets at 360 MPa. The formability of the Li_2S-P_2S_5 glasses is better than that of the Li_2S-SiS_2 and Li_2S-GeS_2 glasses. Moreover, it is suggested that the cation field strength of glass modifiers is related to the formability. Pugh's

ratio (B/G) was used to evaluate ductile-brittle properties of materials. The glass with a larger B/G ratio, meaning higher ductility, tended to display a higher relative density. It is noteworthy that plastic deformation affected the densification of sulfide glasses due to their lower bonding energy, larger free volume, and more isolated structure.

2.5. Reference

[1] A. Hayashi, A. Sakuda, M. Tatsumisago, *Front. Energy Res.* **4** (2016) 1–13.

[2] J. Janek, W. G. Zeier, *Nat. Energy*. **1** (2016) 16141.

[3] A. Manthiram, X. Yu, S. Wang, *Nat. Rev. Mater.* **2** (2017) 16103.

[4] H. Wu, Y. Cui, *Nano Today*. **7** (2012) 414–429.

[5] J. Wolfenstine, J. L. Allen, J. Sakamoto, D. J. Siegel, H. Choe, *Ionics* (2017) 1–6.

[6] Y. Inaguma, C. Liquan, M. Itoh, T. Nakamura, T. Uchida, H. Ikuta, M. Wakihara, *Solid State Commun.* **86** (1993) 689–693.

[7] M. Huang, T. Liu, Y. Deng, H. Geng, Y. Shen, Y. Lin, C. W. Nan, *Solid State Ionics*. **204**–**205** (2011) 41–45.

[8] V. Thangadurai, W. Weppner, *J. Solid State Chem.* **179** (2006) 974–984.

[9] K. Tadanaga, R. Takano, T. Ichinose, S. Mori, A. Hayashi, M. Tatsumisago, *Electrochem. Commun.* **33** (2013) 51–54.

[10] R. Takano, K. Tadanaga, A. Hayashi, M. Tatsumisago, *Solid State Ionics*. **255** (2014) 104–107.

[11] S. W. Baek, J. M. Lee, T. Y. Kim, M. S. Song, Y. Park, *J. Power Sources*. **249** (2014) 197–206.

[12] S. Ohta, J. Seki, Y. Yagi, Y. Kihira, T. Tani, T. Asaoka, *J. Power Sources*. **265** (2014) 40–44.

[13] S. Ohta, S. Komagata, J. Seki, T. Saeki, S. Morishita, T. Asaoka, *J. Power Sources*. **238** (2013) 53–56.

[14] T. Kato, S. Iwasaki, Y. Ishii, M. Motoyama, W. C. West, Y. Yamamoto, Y. Iriyama, *J. Power Sources*. **303** (2016) 65–72.

[15] W. Zhou, S. Wang, Y. Li, S. Xin, A. Manthiram, J. B. Goodenough, *J. Am. Chem. Soc.* **138** (2016) 9385–9388.

[16] X. Tao, Y. Liu, W. Liu, G. Zhou, J. Zhao, D. Lin, C. Zu, O. Sheng, W. Zhang, H. W. Lee, Y. Cui, *Nano Lett.* **17** (2017) 2967–2972.

[17] J. Zhang, X. Zang, H. Wen, T. Dong, J. Chai, Y. Li, B. Chen, J. Zhao, S. Dong, J. Ma,

L. Yue, Z. Liu, X. Guo, G. Cui, L. Chen, *J. Mater. Chem. A*. **5** (2017) 4940–4948.

[18] K. Yoshima, Y. Harada, N. Takami, *J. Power Sources*. **302** (2016) 283–290.

[19] M. Tatsumisago, A. Hayashi, *Int. J. Appl. Glas. Sci.* **5** (2014) 226–235.

[20] A. Sakuda, A. Hayashi, Y. Takigawa, K. Higashi, M. Tatsumisago, *J. Ceram. Soc. Japan*. **121** (2013) 946–949.

[21] A. Sakuda, A. Hayashi, M. Tatsumisago, *Sci Rep*. **3** (2013) 2261.

[22] N. Kamaya, K. Homma, Y. Yamakawa, M. Hirayama, R. Kanno, M. Yonemura, T. Kamiyama, Y. Kato, S. Hama, K. Kawamoto, A. Mitsui, *Nat. Mater.* **10** (2011) 682–686.

[23] Y. Sun, K. Suzuki, S. Hori, M. Hirayama, R. Kanno, *Chem. Mater.* **29** (2017) 5858–5864.

[24] Y. Kato, S. Hori, T. Saito, K. Suzuki, M. Hirayama, A. Mitsui, M. Yonemura, H. Iba, R. Kanno, *Nat. Energy*. **1** (2016) 16030.

[25] Y. Seino, T. Ota, K. Takada, A. Hayashi, M. Tatsumisago, *Energy Environ. Sci.* **7** (2014) 627–631.

[26] K. Minami, A. Hayashi, S. Ujiie, M. Tatsumisago, *Solid State Ionics*. **192** (2011) 122–125.

[27] T. Ohtomo, F. Mizuno, A. Hayashi, K. Tadanaga, M. Tatsumisago, *J. Power Sources*. **146** (2005) 715–718.

[28] T. Ohtomo, A. Hayashi, M. Tatsumisago, K. Kawamoto, *J. Non. Cryst. Solids*. **364** (2013) 57–61.

[29] M. Ménétrier, C. Estournès, A. Levasseur, K.J. Rao, *Solid State Ionics*. **53–56** (1992) 1208–1213.

[30] R. Mercier, J. P. Malugani, B. Fahys, G. Robert, *Solid State Ionics*. **5** (1981) 663–666.

[31] S. Ujiie, A. Hayashi, M. Tatsumisago, *Mater. Renew. Sustain. Energy*. **3** (2014) 1–8.

[32] S. Ujiie, T. Inagaki, A. Hayashi, M. Tatsumisago, *Solid State Ionics*. **263** (2014) 57–61.

[33] Y. Kubota, M. C. S. Escao, H. Nakanishi, H. Kasai, *J. Appl. Phys.* **102** (2007) 1–6.

[34] M. Ashuri, Q. He, L. L. Shaw, *Nanoscale*. **8** (2016) 74–103.

[35] M. Gu, Z. Wang, J. G. Connell, D. E. Perea, L. J. Lauhon, F. Gao, C. Wang, *ACS Nano*. **7** (2013) 6303–6309.

[36] N. Soga, H. Yamanaka, C. Hisamoto, M. Kunugi, *J. Non. Cryst. Solids*. **22** (1976) 67–76.

[37] K. Homma, M. Yonemura, T. Kobayashi, M. Nagao, M. Hirayama, R. Kanno, *Solid State Ionics*. **182** (2011) 53–58.

[38] A. Makishima, J. D. Mackenzie, *J. Non. Cryst. Solids*. **12** (1973) 35–45.

[39] S. Inaba, S. Fujino, K. Morinaga, *J. Am. Ceram. Soc.* **82** (1999) 3501–3507.

[40] P. Boolchand, P. Chen, U. Vempati, *J. Non. Cryst. Solids*. **355** (2009) 1773–1785.

[41] M. Tachez, J. P. Malugani, R. Mercier, G. Robert, *Solid State Ionics*. **14** (1984) 181–185.

[42] S. S. Berbano, I. Seo, C. M. Bischoff, K. E. Schuller, S. W. Martin, *J. Non. Cryst. Solids*. **358** (2012) 93–98.

[43] C. Bischoff, K. Schuller, M. Haynes, S. W. Martin, *J. Non. Cryst. Solids*. **358** (2012) 3216–3222.

[44] Y. R. Luo, J. A. Kerr, "CRC handbook of chemistry and physics", Ed. by D. R. Lide. and CRC Press Taylor&Flancis, Boca Raton (2006) pp.9-54–9-59.

[45] T. Rouxel, S. Yoshida, *J. Am. Ceram. Soc.* **100** (2017) 4374–4396.

[46] T. Rouxel, *J. Am. Ceram. Soc.* **90** (2007) 3019–3039.

[47] A. R. Cooper, L.E. Eaton, *J. Am. Ceram. Soc.* **45** (1962) 97–101.

[48] A. Kato, M. Nagao, A. Sakuda, A. Hayashi, M. Tatsumisago, *J. Ceram. Soc. Japan*. **122** (2014) 552–555.

[49] M. Nose, A. Kato, A. Sakuda, A. Hayashi, M. Tatsumisago, *J. Mater. Chem. A*. **3** (2015) 22061–22065.

[50] Y. Wang, T. Matsuyama, M. Deguchi, A. Hayashi, A. Nakao, M. Tatsumisago, *J. Ceram. Soc. Japan*. **124** (2016) 597–601.

[51] J. Swenson, L. Börjesson, *Phys. Rev. Lett.* **77** (1996) 3569–3572.

[52] S. B. Son, J. E. Trevey, H. Roh, S. H. Kim, K. B. Kim, J. S. Cho, J. T. Moon, C. M.

DeLuca, K. K. Maute, M. L. Dunn, H. N. Han, K. H. Oh, S. H. Lee, *Adv. Energy Mater.* **1** (2011) 1199–1204.

[53] K. Takahashi, A. Osaka, *J. Ceram. Soc. Jpn.* **91** (1983) 116–120.

[54] M. Ashizuka, T. Sakai, A. Iwata, *J. Ceram. Soc. Jpn.* **91** (1983) 86–94.

[55] M. Ashizuka, T. Sakai, *J. Ceram. Soc. Jpn.* **91** (1983) 176–182.

[56] M. Kodama, S. Kojima, S. Feller, M. Affatigato, *Phys. Chem. Glas.* **46** (2005) 190–193.

[57] M. Kodama, A. Ono, S. Kojima, S. A. Feller, M. Affatigato, *Phys. Chem. Glas.* **47** (2006) 465–470.

[58] A. Mohajerani, V. Martin, D. Boyd, J. W. Zwanziger, *J. Non. Cryst. Solids*. **381** (2013) 29–34.

[59] T. N. Mel'nichenko, V. I. Fedelesh, I. M. Yurkin, T. D. Mel'nichenko, *Glas. Phys. Chem.* **28** (2002) 25–32.

[60] J. Guin, T. Rouxel, V. Keryvin, J. Sanglebœuf, I. Serre, J. Lucas, *J. Non Cryst. Solids*. **298** (2002) 260–269.

[61] T. D. Mel'nichenko, V. I. Fedelesh, T. N. Mel'nichenko, D. S. Sanditov, S. S. Badmaev, D. G. Damdinov, *Glas. Phys. Chem.* **35** (2009) 32–42.

[62] A. Dietzel, *Z. Electrochem.* **48** (1942) 3.

[63] R. D. Shannon, *Acta Crystallogr. Sect. A.* **32** (1976) 751–767.

[64] S. F. Pugh, *Philos. Mag. Ser. 7.* **45** (1954) 823–843.

[65] Z. Deng, Z. Wang, I. H. Chu, J. Luo, S. P. Ong, *J. Electrochem. Soc.* **163** (2016) A67–A74.

[66] S. Yu, R. D. Schmidt, R. Garcia-Mendez, E. Herbert, N. J. Dudney, J. B. Wolfenstine, J. Sakamoto, D. J. Siegel, *Chem. Mater.* **28** (2016) 197–206.

3. Interface formation between lithium metal negative electrodes and sulfide solid electrolytes

3.1. Introduction

Bulk-type batteries are one type in all-solid-state batteries [1]. They are expected to use for large-scale applications such as electric vehicles or smart grid systems [2]. Lithium (Li) metal negative electrodes are an attractive choice to achieve bulk-type all-solid-state batteries with high energy density [3]. However, present bulk-type cells using Li metal electrodes suffer from low areal capacities at most 1.5 mAh cm^{-2} because of short-circuiting by Li dendrites. Interface formation between Li metal and solid electrolytes is closely associated with the generation of the Li dendrite. The design of the interface suppressing Li dendrites is urgently needed.

Vacuum-evaporation of Li metal is a good technique to form an interface between Li metal and solid electrolytes. Nagao *et al.* have reported that a uniform interface with a large contact area prepared by vacuum-evaporation of Li metal improves the reversibility of Li dissolution/deposition in bulk-type batteries [4]. In addition, it has been reported that the interface modification by inserting indium thin films between Li metal and sulfide solid electrolytes is effective to reduce a risk of short-circuiting in all-solid-state Li/$Li_4Ti_5O_{12}$ cells [5]. Some researchers also have reported that Li dissolution/deposition cycles in all-solid-state symmetric cells with garnet-type $Li_7La_3Zr_2O_{12}$ electrolytes were improved by the interface modifications with the insertion of metal or metal oxide thin films such as Au, Si, Ge, Al, Al_2O_3, and ZnO [6–12]. Moreover, as for garnet-type electrolytes, there are several studies on the interface formation in terms of operating temperatures in Li metal cells [13,14]. An advantage of inorganic solid electrolytes is that they have thermal stability even at above 60°C, which is difficult to use in organic liquid electrolytes. It was reported that the interfacial resistance between Li metal and garnet-type $Li_7La_3Zr_2O_{12}$ electrolytes decreased, and Li dissolution/deposition performance of symmetric Li metal cells improved at high temperatures (~100°C) [13,14]. As stated above, many researches have suggested the

importance of the interface between Li metal and solid electrolytes. However, the interface factors determining Li dissolution/deposition behaviors have not been clarified. Structure of the solid electrolytes at the interface, morphology changes of Li metal, and interfacial resistances should be important clues to design a favorable interface suppressing the Li dendrites.

The purpose of this chapter is the improvement of all-solid-state Li metal batteries by examining the interface formation between Li metal and solid electrolytes. At first, all-solid-state Li symmetric cells were fabricated by vacuum-evaporation of Li metal on powder-compressed pellets of Li_3PS_4 glass electrolytes. The utilization of Li metal, morphology changes of Li metal, and the interfacial resistance were evaluated for the cells. First principle calculations suggest that Li_3PS_4 electrolytes thermodynamically decompose into Li_2S and Li_3P in contact with Li metal [15]. The structure changes of Li_3PS_4 electrolytes at the interface were investigated by XPS. In addition, the stability of the Li/Li_3PS_4 interface after storage for one year was examined by impedance measurements and SEM observations. Moreover, effects of inserting gold (Au) thin films to the interface between Li metal and Li_3PS_4 electrolytes were investigated as a model of interface modifications. Au thin films are often used as current collectors for measuring conductivities of sulfide solid electrolytes, and therefore Au has good compatibility with sulfides. For large scale applications, high rate performance with large areal capacities are needed in all-solid-state batteries. High operating temperatures allow for high ionic conduction of solid electrolytes and fast chemical reactions at the electrode/electrolyte interface, which improves the electrochemical performance of the batteries. The Li dissolution/deposition behavior of Li metal cells with Li_3PS_4 glass electrolytes was compared at 25°C and 100°C. The effects of high-temperature operation on Li dissolution/deposition behaviors at the Li/Li_3PS_4 interface modified with Au thin films were also examined.

3.2. Experimental

3.2.1. Cell configuration and setting for electrochemical tests

Sulfide glasses at the composition of $75Li_2S \cdot 25P_2S_5$ (mol%) (Li_3PS_4) were prepared by mechanochemical synthesis using ball-milling apparatus [16]. The obtained powders were pelletized by pressing under pressure of 360 MPa at ambient temperature. The diameter and thickness of the electrolyte pellets were about 10 mm and 0.76 mm, respectively. In order to investigate electrochemical properties of Li dissolution and deposition, symmetric cells with Li/Li_3PS_4/Li configuration were fabricated. A Li thin film was formed on both sides of the electrolyte pellet by vacuum-evaporation. The active electrode area of all the cells was 0.785 cm^2, which was the same as the diameter of electrolyte pellets. In order to investigate the effects of the insertion of Au thin film between Li metal and Li_3PS_4 solid electrolytes, Au thin film was also deposited by vacuum-evaporation before depositing Li films. A thermal evaporator (VPC-060, ULVAC, Inc.) placed in an Ar-filled glove box was used for preparation of Li and Au thin films. Each thickness of the Li and Au thin films was about 3 μm and about 60 nm, respectively. The obtained pellets after vacuum-evacuation of Li and Au films were sandwiched between two stainless-steels plates as a current collector. The pellets with current collectors were packed in an Ar-filled cell. The electrochemical tests were conducted at 25°C using charge-discharge measuring devices (BTS-2004, Nagano Co.), whose lead wires were connected to the stainless-steel electrodes in the cell. At first, the symmetric cells were worked at a negative potential direction and stopped when the cell potential reaches to -50 mV. After that, the cell operation was switched to a positive potential direction until an electrical quantity was the same as that obtained at the previous operation. As a result, the quantity of Li on both sides were unchanged after each cycle of Li dissolution and deposition. The current density for galvanostatic cycling tests was 0.064 mA cm^{-2}.

Symmetric cells were also fabricated using Li foils. Li foils (0.25 mm of thickness, 9 mm of diameter) were attached to both surfaces of the Li_3PS_4 glass pellet. Stainless steel foils (0.02 mm of thickness, 10 mm of diameter) were put on the Li foils as current collectors. These were sealed in vacuum in a pouch with Ni lead plates for connecting to

charge-discharge measuring devices (BTS-2004, Nagano Co.). These procedures were performed in a dry Ar atmosphere. At the end of the cell assembly, the pouch was pressed at 90 MPa by cold isostatic pressing (CIP) for better contacts between Li foils and Li_3PS_4 pellets. Symmetric cells with Au thin films were fabricated in the same procedure. Au thin films with a thickness of about 60 nm were deposited by vacuum-evaporation before attaching Li foils. In addition, all-solid-state cells with the Li/Li_3PS_4/$LiNi_{1/3}Mn_{1/3}Co_{1/3}O_2$ (NMC) configuration were fabricated. $LiNbO_3$-coated NMC, Li_3PS_4 glass powders were mixed in an agate mortar at the composition of 70:30 in wt%. The NMC composite electrode (10 mg or 65 mg) and separator layer of Li_3PS_4 glass (50 mg) were pelletized by cold-pressing at 360 MPa (10 mm in diameter). A Li foil was then attached on the surface of the separator layer side of the bilayer pellet. The three-layered pellet was sandwiched between two stainless steel as a current collector and was sealed in a pouch with Ni lead plates. A hydrostatic pressure of 90 MPa was applied to assemble the cell. The electrochemical tests were conducted at 25°C and 100°C. A cell resistance was measured by AC impedance method using an impedance analyzer (Solartron, 1260).

3.2.2. Characterization

XPS spectra of the Li/Li_3PS_4 and Li/Au/Li_3PS_4 interfaces were measured by using a spectrometer (K-Alpha, Thermo Fisher Scientific). Samples were transferred to the analysis chamber using a vessel packed with a dry Ar gas. Monochromatic Al-Kα radiation (1486.6 eV) was used as the X-ray source. To remove the influence of the charging effect on the spectra, neutralization of the samples was performed during the measurement by the combined use of a flood gun. The samples were etched by Ar^+ ion monomer and depth analyses were carried out from the top of the Li film into the Li_3PS_4 electrolyte. The obtained spectra were calibrated by setting the measured binding energy (BE) of the C1s peak to 284.7 eV of adventitious carbon accumulated in the analysis chamber of the spectrometer [17].

Morphology changes of Li metal were observed after three different cell operations by SEM (JSM-6610A, JEOL); after the initial dissolution, the following deposition, and after 5

cycles. Some interfaces between Li metal and Li_3PS_4 electrolytes was observed by a field emission scanning electron microscope (FE-SEM, SU8220; Hitachi). Before FE-SEM observation, Ar ion-milling was done to prepare a flat surface of the interface using an ion-milling system (IM4000; Hitachi).

3.3. Results and discussion

3.3.1 Interface formation using vacuum-evaporation of lithium metal

A SEM image for cross-section of the interface between a Li thin film and Li_3PS_4 solid electrolytes are shown in Fig. 3-3-1. The electrolyte pellet pressed at ambient temperature has some grain boundaries and voids on the surface as well as cross-section of the pellet. It is noted that the deposited Li thin film fills with the grain boundaries and voids on the surface of solid electrolytes, and thus good interfaces with large contact areas between Li metal and Li_3PS_4 solid electrolytes were obtained. The thickness of a Li thin film was about 3 μm. Therefore, the loading of Li metal was about 0.126 mg calculated from the density of Li (6.941 g cm^{-3}).

Galvanostatic cycling tests for the Li/Li_3PS_4/Li cell are shown in Fig. 3-3-2. At the initial cycle, the dissolution/deposition time of the cell was about 4 hours (915 mC cm^{-2}), which corresponded to about 0.0518 mg of Li dissolution/deposition; the utilization of Li metal was thus about 40 % calculated from the loading of Li metal. 40 % of utilization of Li metal was higher than the utilization of Li metal for thin-film batteries (which was at most 20 %, calculated utilization based on the reference [18–21]). High utilization of Li metal is demanded for practical Li metal batteries, and the cell with high utilization of Li metal meets the demand for batteries with a high energy density. The interface prepared by vacuum-evaporation of Li metal exhibited the high utilization at the initial cycle. However, the utilization of Li metal for the cell decreased rapidly for 5 cycles.

For the investigation of interface modification, an Au thin film was inserted at the interface between the Li thin film and Li_3PS_4 electrolytes. Figure 3-3-3 shows a SEM image for cross-section of the interface between the Au thin film and Li_3PS_4 electrolytes. The Au

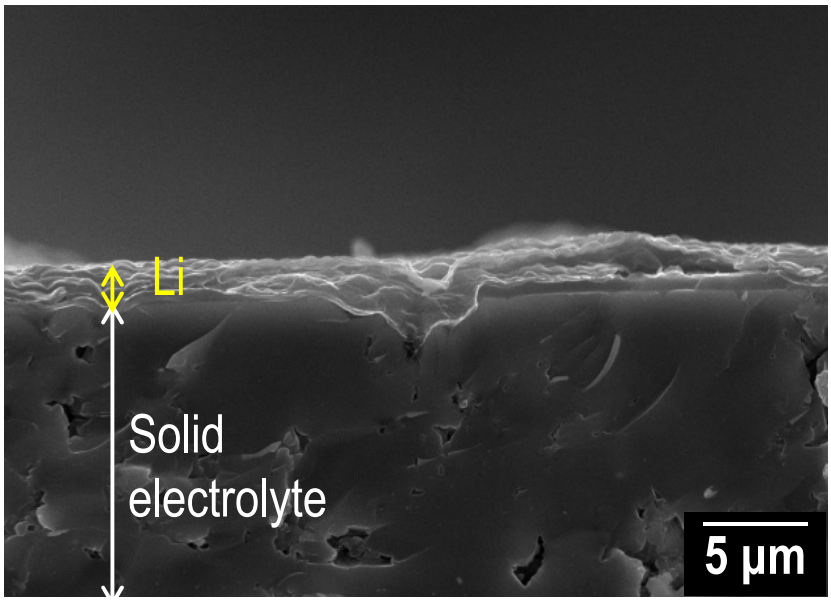

Fig. 3-3-1 Cross-sectional SEM image of the interface between a Li thin film and powder-compressed Li_3PS_4 solid electrolytes.

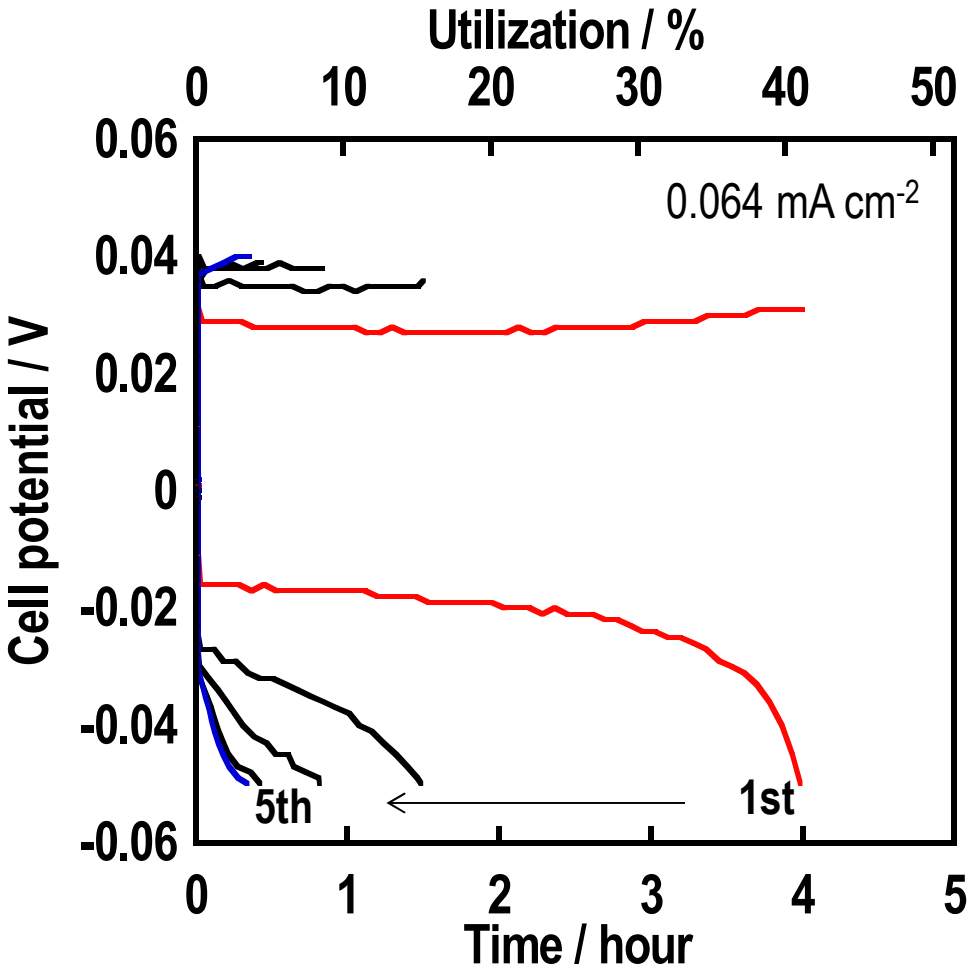

Fig. 3-3-2 Galvanostatic cycling tests for Li symmetric cells using Li thin films.

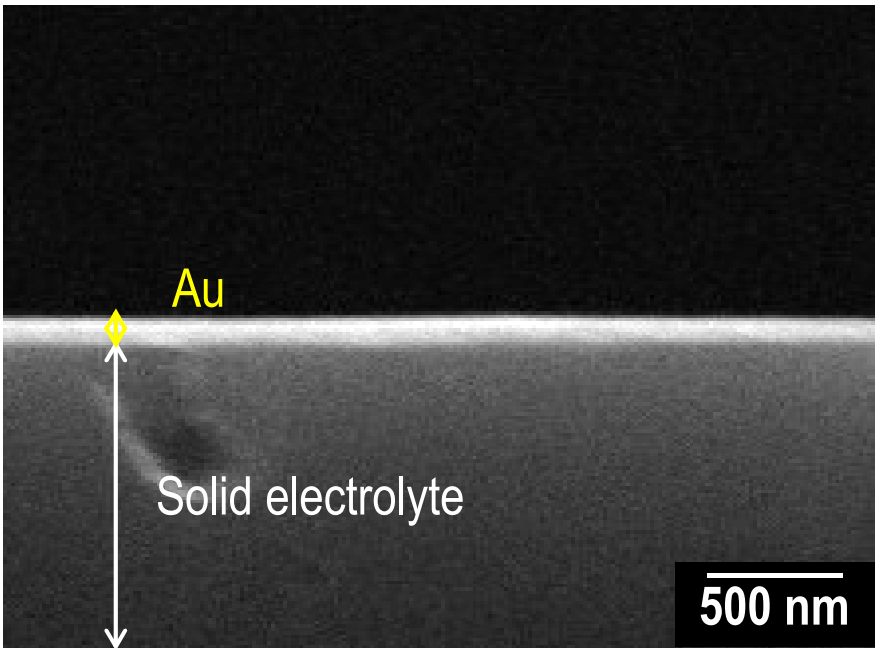

Fig. 3-3-3 Cross-sectional SEM image of the interface between the Au thin film and Li_3PS_4 solid electrolytes.

thin film was adhesively formed on the Li_3PS_4 electrolytes and the thickness of the Au thin film was about 60 nm. XRD patterns of the Au thin films after vacuum-evaporation of Li metal on the electrolyte are shown in Fig. 3-3-4. Diffraction peaks assigned to $Li_{15}Au_4$ alloy, which is the most lithiated phase in Li-Au alloys [22], were observed. The amount of Li deposited by vacuum-evacuation is excess above the amount of Li used for forming $Li_{15}Au_4$ alloy (the Li/Au ratio was 40 by molar basis). Thus, diffraction peaks assigned to Li metal were also observed in Fig. 3-3-4. The intensity of diffraction peaks of Li metal was much lower than that of the Li-Au alloy. The reason has not been clarified yet, but it may be based on the difference of atomic scattering factors for X-ray between Li and Au. Galvanostatic cycling tests for the Li/Au/Li_3PS_4/Au/Li cell are shown in Fig. 3-3-5. At the initial cycle, the Li dissolution/deposition time of the cell was about 3.5 hours (800 mC cm^{-2}), corresponding to about 0.0453 mg of dissolution/deposition (about 35% of Li utilization). Furthermore, about 25 % of utilization of Li metal was retained after the 5th cycle.

In order to find clues for the differences in electrochemical performances with and without the Au films, structure of solid electrolytes at the interfaces was analyzed by XPS. Figure 3-3-6 (a) shows the depth profile of atomic ratios for the sample with the Li/Li_3PS_4 interface. Since the sample was etched from the top of Li metal into Li_3PS_4 electrolyte, all atomic ratios approached to the constant ratios with the increase of the etching time. The author determined interface position as about half of the constant ratios. S2p and P2p XPS spectra at the Li/Li_3PS_4 interface and inside of Li_3PS_4 solid electrolyte (SE) are shown in Fig. 3-3-6 (b). From S2p spectra, not only S^- doublet peaks ($2p_{1/2}$ and $2p_{2/3}$) of Li_3PS_4 ($S2p_{3/2}$: 161.5 eV) [17] but also S^{2-} doublet peaks of Li_2S ($S2p_{3/2}$: 160.1 eV) [17,23] were observed at the interface. Furthermore, doublet peaks of Li_3P ($P2p_{3/2}$: 125.8 eV) [24,25] and broad peaks of the other reduced phosphorus compounds such as Li_xP ($0 \leq x < 3$) were detected from P2p spectra at the interface. On the other hand, the spectra for inside of SE are attributed to Li_3PS_4 electrolyte, suggesting that Li_3PS_4 electrolyte was partially reduced at the Li/Li_3PS_4 interface. The reduction reaction of sulfide solid electrolytes has been predicted by theoretical calculations [15] and the author has experimentally observed the reduction of the Li_3PS_4

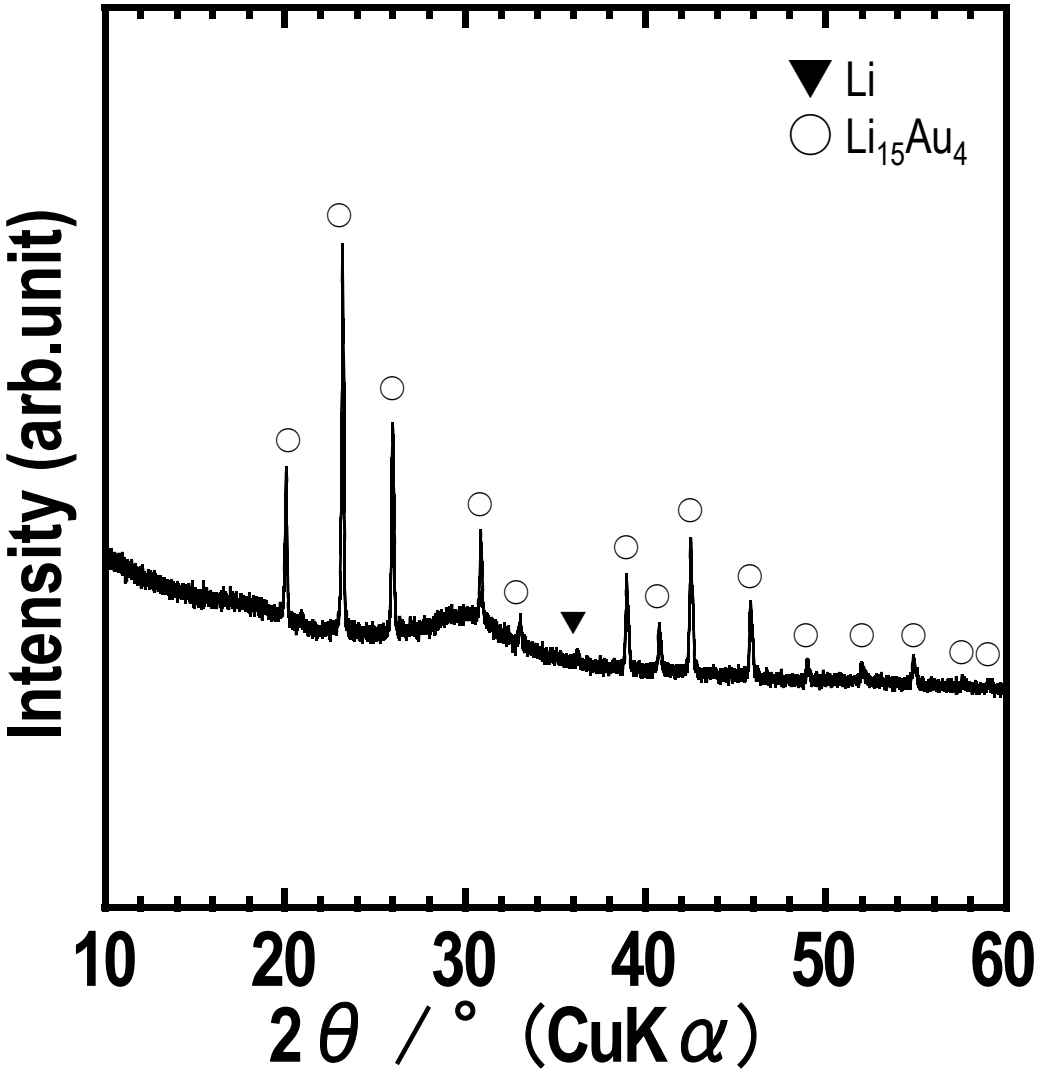

Fig. 3-3-4 XRD patterns of Li/Au thin films on the Li_3PS_4 solid electrolytes.

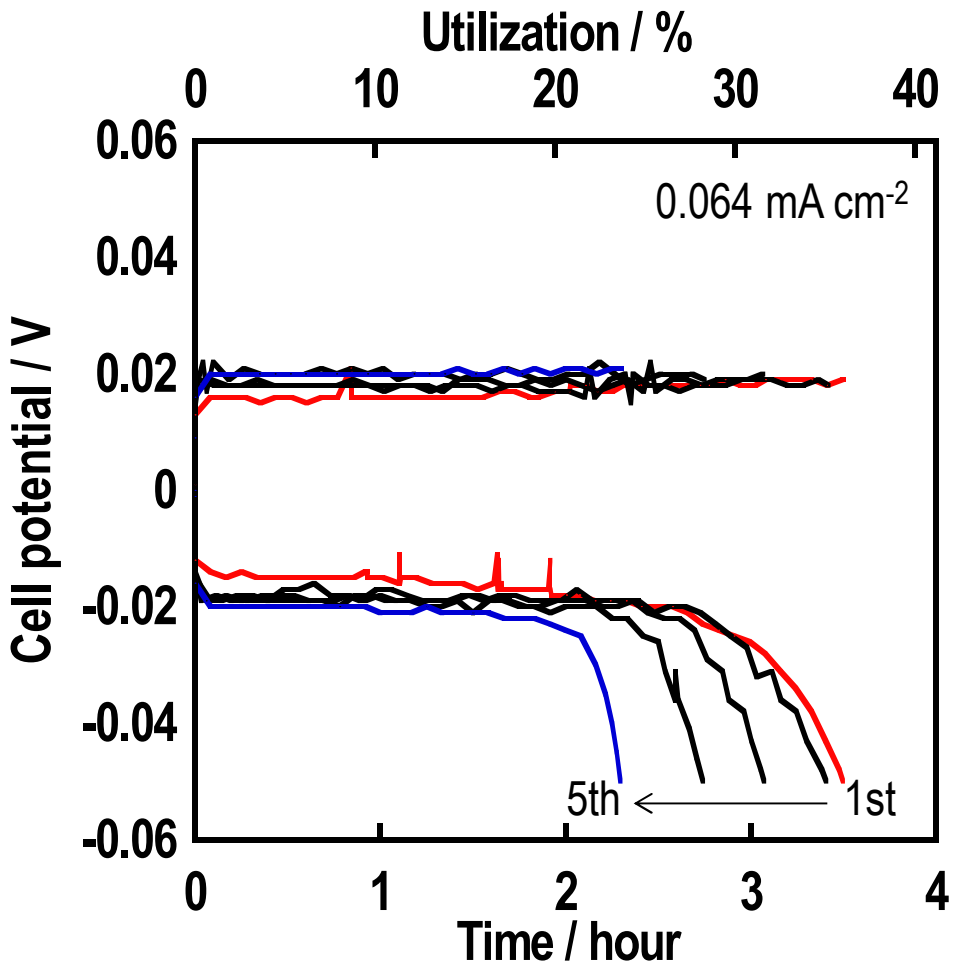

Fig. 3-3-5 Galvanostatic cycling tests for the Li symmetric cell inserting Au thin film.

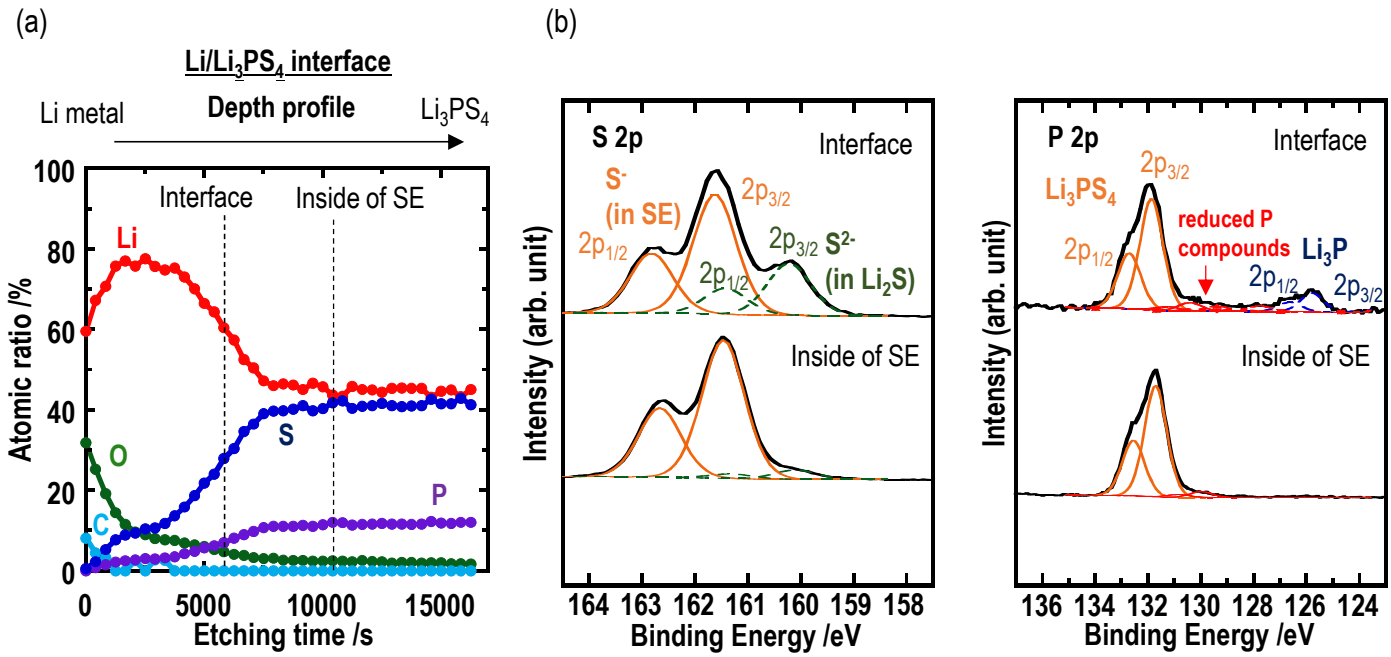

Fig. 3-3-6 (a) Depth profile of atomic ratios for the Li/Li_3PS_4 interface. (b) S2p and P2p XPS spectra at the Li/Li_3PS_4 interface and inside of Li_3PS_4 electrolyte.

in the vicinity of Li metal in this study. Reduction phenomena of other sulfides such as $Li_{10}GeP_2S_{12}$ and $Li_7P_3S_{11}$ electrolytes were also confirmed by XPS [24,25].

The passivation ability of the reduced product layer was investigated by FE-SEM and AC impedance. Figure 3-3-7 shows a back scattered electron image of the Li/Li_3PS_4 interface after storage in dry Ar atmosphere for 1 year. A cross-section of the Li/Li_3PS_4 interface was prepared by Ar ion-milling before FE-SEM observation. Any cracks or compositional changes by the reduction reaction were not observed at this scale, suggesting that clear interface between Li metal and Li_3PS_4 electrolytes was maintained during storage for one year. It is noteworthy that the reduced product layer was stable and thin (at least less than tens of nm) and degradation of the interface was not observed. AC impedance measurement was also done for the Li/Li_3PS_4/Li cell after storage for one year (Fig. 3-3-8). The resistance of the Li/Li_3PS_4/Li cell increased little after one year, indicating that the reduced product layer has a low resistance and good stability as predicted by theoretical calculations [15]. This is because the reduced products have ionic conductivities but poor electronic conductivities [26,27].

S2p and P2p XPS spectra at the Li/Au/Li_3PS_4 interface and inside of Li_3PS_4 solid electrolyte are shown in Fig. 3-3-9. The peaks of the reduced products such as Li_2S, Li_3P, and the other phosphorus compounds were observed at the Li/Au/Li_3PS_4 interface. Some peaks at around 130 eV in P2p spectra are attributable to reduced P compounds of Li_xP ($0 \leq x < 3$) and may also be attributable to Au-P compounds; further structural investigation is needed to clarify the peak assignment. The ratios of the reduced products in each element are calculated from the peak deconvolution of S2p and P2p spectra are shown in Table 3-3-1. The amounts of the reduced products were almost the same between the Li/Li_3PS_4 and Li/Au/Li_3PS_4 interfaces. As shown in the depth profile of atomic ratios for the Li/Au/Li_3PS_4 interface in Fig. 3-3-9, the atomic ratio of Au was mainly detected between Li metal and Li_3PS_4 electrolyte. In addition, Au was alloyed with Li to $Li_{15}Au_4$ phase at the interface, which indicates that the Li_3PS_4 electrolyte had a contact with the Li-Au alloy layer. Nevertheless, the Li_3PS_4 electrolytes at the interfaces were partially reduced regardless of the insertion of Au to the Li/Li_3PS_4 interface. This is because the potential of Li-Au alloy (0.1- 0.3 V vs. Li^+/Li) [28] is

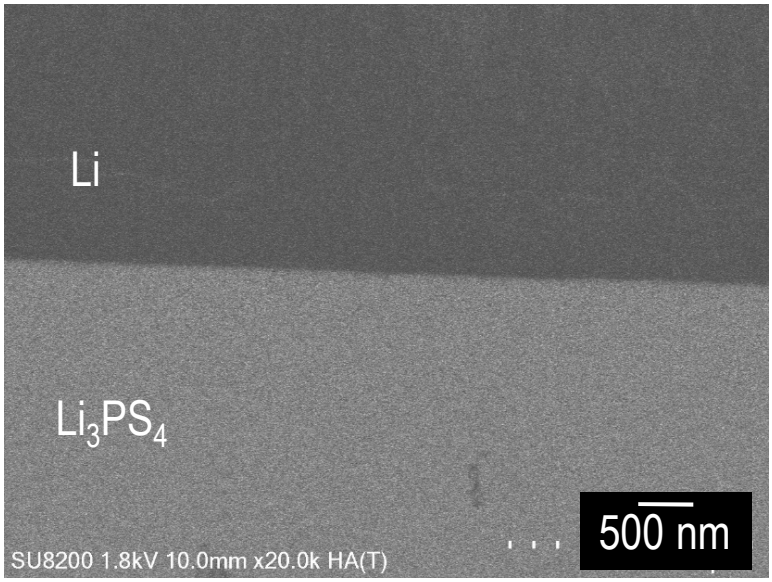

Fig. 3-3-7 Cross-sectional back scattered electron image of the Li/Li_3PS_4 interface after storage in a dry Ar atmosphere for one year.

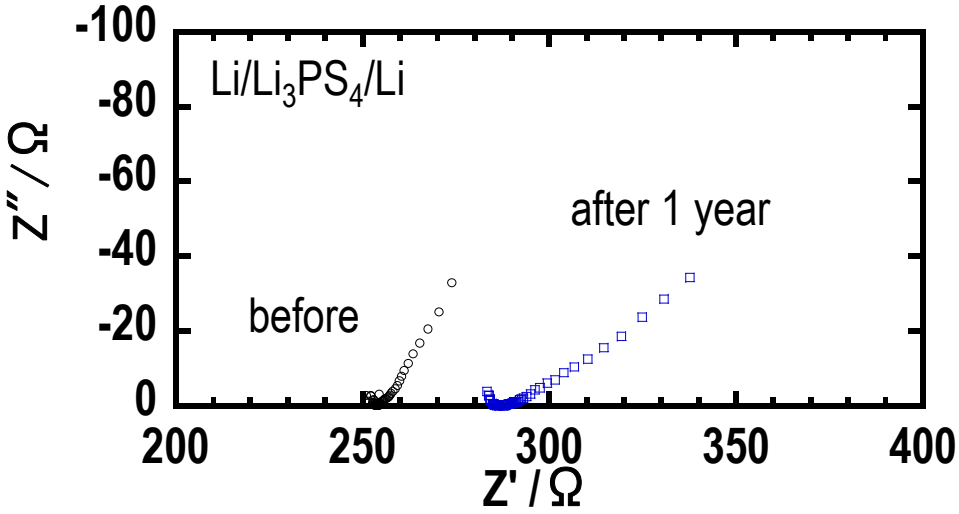

Fig. 3-3-8 Impedance plots of $Li/Li_3PS_4/Li$ cells before and after storage in a dry Ar atmosphere for one year.

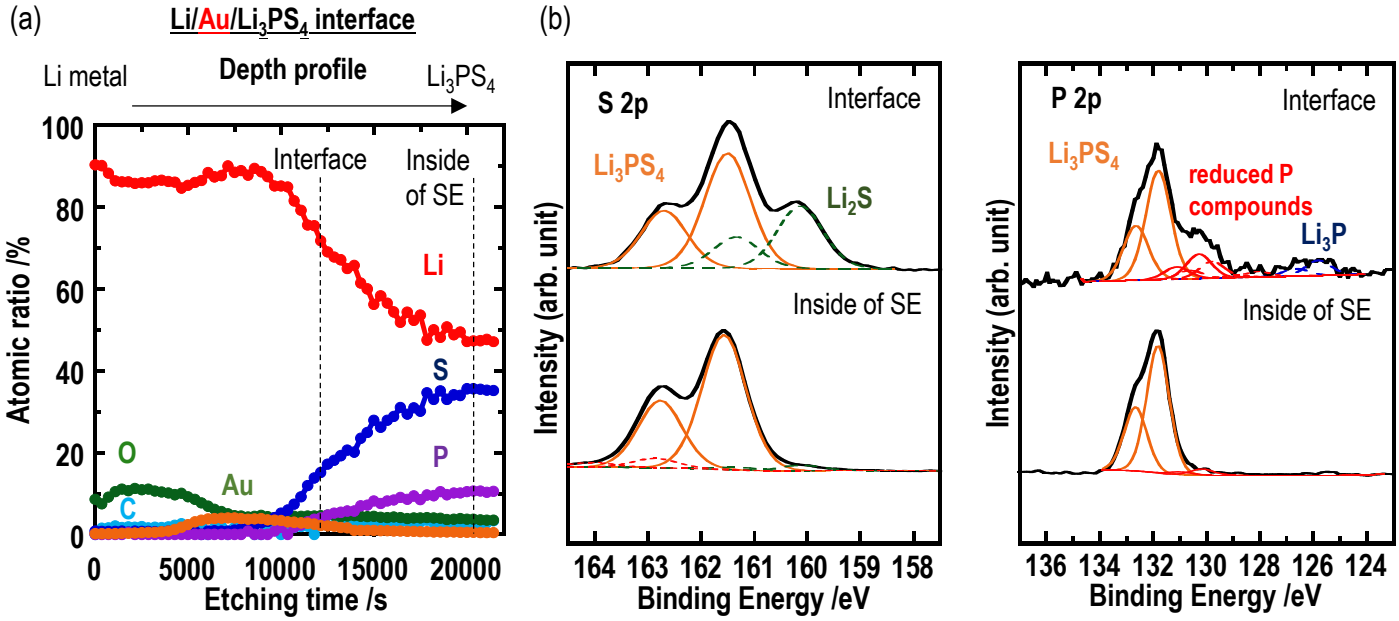

Fig. 3-3-9 (a) Depth profile of atomic ratios for the Li/Au/Li_3PS_4 interface. (b) S2p and P2p XPS spectra at the Li/Au/Li_3PS_4 interface and inside of Li_3PS_4 electrolyte.

Table 3-3-1 The ratios of reduced products in each element for the Li/Li_3PS_4 and $Li/Au/Li_3PS_4$ interfaces

	Li_2S ratio in all S species	reduced P compounds (including Li_3P) ratio in all P species
Li/Li_3PS_4 interface	0.31	0.26
$Li/Au/Li_3PS_4$ interface	0.35	0.36

close to that of Li metal. It is assumed that there is little difference between structure of the electrolytes at interfaces with and without Au films.

Figure 3-3-10 shows impedance plots of the Li/Li_3PS_4/Li cell (a) before galvanostatic tests, and (b) after the tests at the negative potential direction (i) and at the positive potential direction (ii). These impedance plots exhibit that a cell resistance before galvanostatic tests was about 250 Ω and increased largely after the initial galvanostatic tests at the negative potential side. The cell resistance decreased slightly after galvanostatic tests at the positive potential side and increased slightly after following galvanostatic tests at the negative potential side again. The cell resistance includes various kinds of resistance components. The resistance of a distorted semicircle with characteristic frequency of 250 kHz is probably attributed to the interfacial resistance of Li metal and Li_3PS_4 electrolytes, and the resistance at the higher frequency region of the semicircle is attributed to the resistance of the electrolyte pellet. Figure 3-3-11 shows the impedance plots of the Li/Au/Li_3PS_4/Au/Li cell (a) before galvanostatic tests, and (b) after the tests at the negative potential direction (i) and at the positive potential direction (ii). The interfacial resistance between Li metal and Li_3PS_4 electrolytes with characteristic frequency of 250 kHz disappeared for the cell with Au thin films. The resistance of the cell with Au thin films was lower than that of the cell without Au thin films.

Morphology changes of Li metal for the Li/Li_3PS_4/Li and Li/Au/Li_3PS_4/Au/Li cells were investigated after three cell operations; after the initial dissolution, the following deposition, and after 5 cycles. The SEM images of the Li surfaces and schematic diagrams are summarized in Fig. 3-3-12. Compared to the morphology of Li metal before galvanostatic tests, a contrast caused by difference of Li thickness was observed after the initial dissolution for the Li/Li_3PS_4/Li cell. Voids were generated between Li metal and the solid electrolyte because of the inhomogeneous Li dissolution. In addition, needle-like and granular deposits were observed after the following deposition. It is assumed that the voids created with uneven current distribution and led to extremely inhomogeneous Li deposition such as needle-like deposits. As a result, it is considered that the rapid decrease of utilization of Li metal was

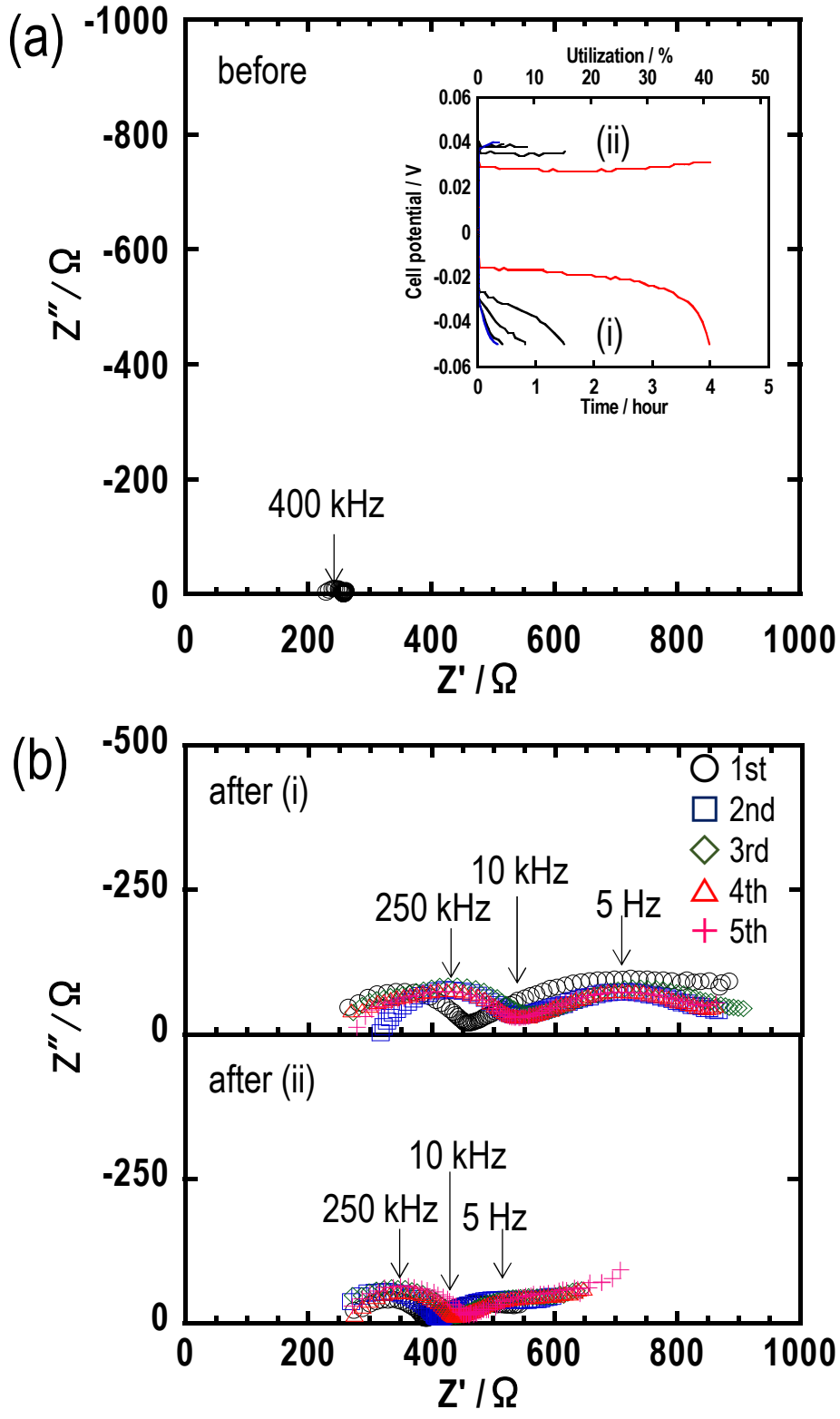

Fig. 3-3-10 Impedance plots of Li symmetric cells (a) before galvanostatic tests, and (b) after the tests at the negative potential direction (i) and at the positive potential direction (ii).

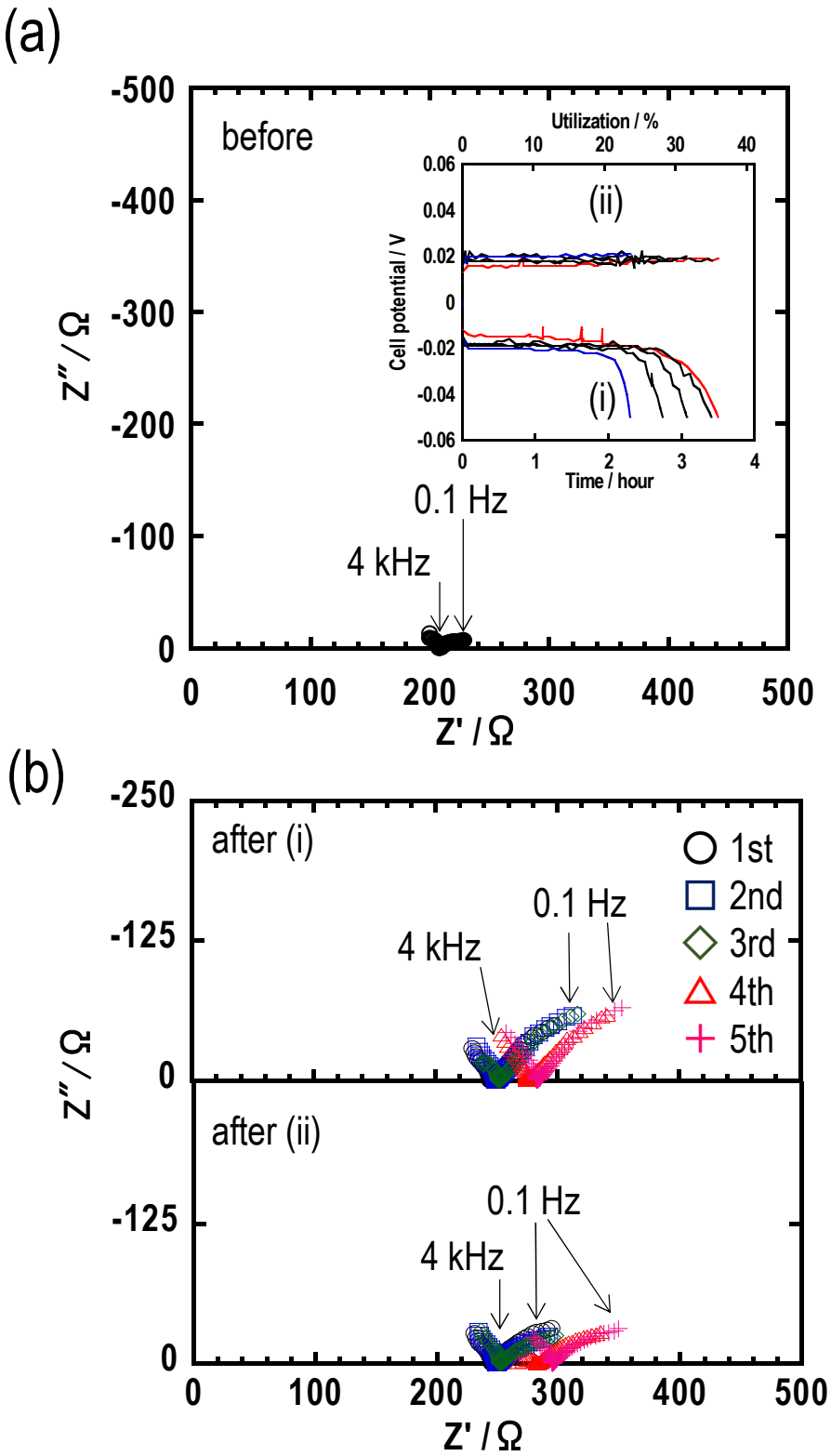

Fig. 3-3-11 Impedance plots of the Li/Au/Li_3PS_4/Au/Li cell (a) before galvanostatic tests, and (b) after the tests at the negative potential direction (i) and at the positive potential direction (ii).

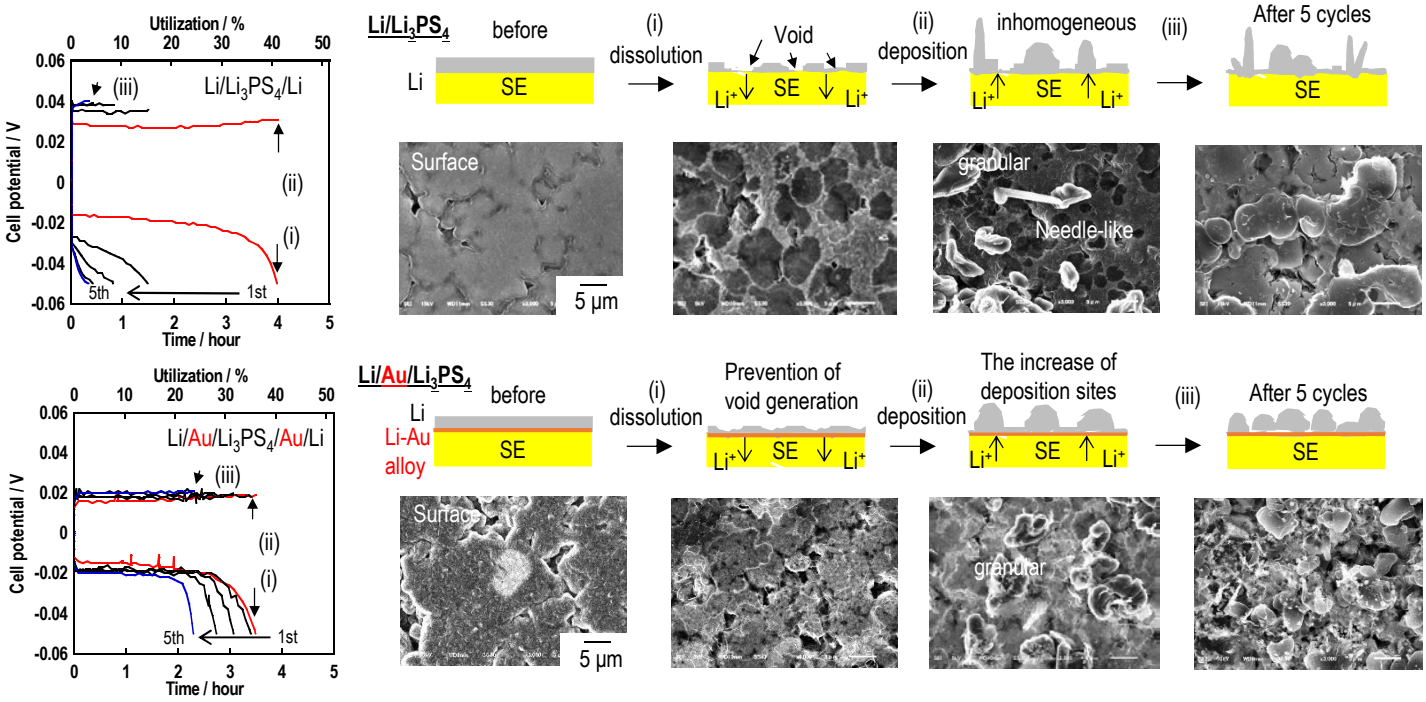

Fig. 3-3-12 SEM images of lithium surfaces and schematic diagrams of morphology changes for lithium metal during galvanostatic cycling tests. SEM observation was done after three cell operations; (i) after initial dissolution, (ii) the following deposition, and (iii) after 5 cycles.

caused by the drastic morphology change after the initial cycle for the cell with the Li/Li_3PS_4 interface. The inhomogeneous dissolution/deposition repeatedly proceeded after 5 cycles. The resistance changes in Fig. 3-3-10 are well-explained by considering the generation and disappearance of voids at the interface between Li metal and Li_3PS_4 electrolytes [29]. It is surprising that the morphology of Li metal changed drastically, though uniform interfaces with large contact areas were formed by vacuum-evaporation before galvanostatic tests. Note that grain boundaries and pores remained on the surface of the powder-compressed Li_3PS_4 pellet. The inhomogeneous dissolution/deposition reaction at the interface may be suppressed by decreasing such grain boundaries and pores. On the other hand, for the cell with the Au thin film, a contrast caused by difference of Li thickness was not clearly observed. In addition, needle-like deposits were few and the similar size of granular deposits were observed after Li deposition. The more uniform morphology of Li metal was retained after the 5th cycle. Li-Au alloy was formed at the Li/Au/Li_3PS_4 interface. The Li-Au alloy layer can prevent void generation during Li dissolution, corresponding to the disappearance of the interfacial resistance with characteristic frequency of 250 kHz in Fig. 3-3-11. Moreover, the remained Li-Au alloy would increase Li deposition sites, and thus more uniform deposition after 5 cycles for the cell with the Au thin film was observed. The reversibility of Li dissolution/deposition for the cell with Au thin films is not a sufficient level for application now, and thus optimizing the thickness of alloy layers and controlling the surface morphology of solid electrolyte layers are important for further improvement of uniform dissolution/deposition and its reversibility. It is noteworthy that homogeneous Li dissolution/deposition reactions occur by inserting Au thin film between the Li thin film and Li_3PS_4 solid electrolytes.

3.3.2 High temperature performance of all-solid-state lithium metal batteries

In this section, Li foils were mainly used for the evaluation. Li foils were attached to Li_3PS_4 electrolytes by CIP. The impedance plots of Li/Li_3PS_4/Li cells before and after CIP are shown in Fig. 3-3-13 (a). A resistance of a distorted semicircle with the characteristic

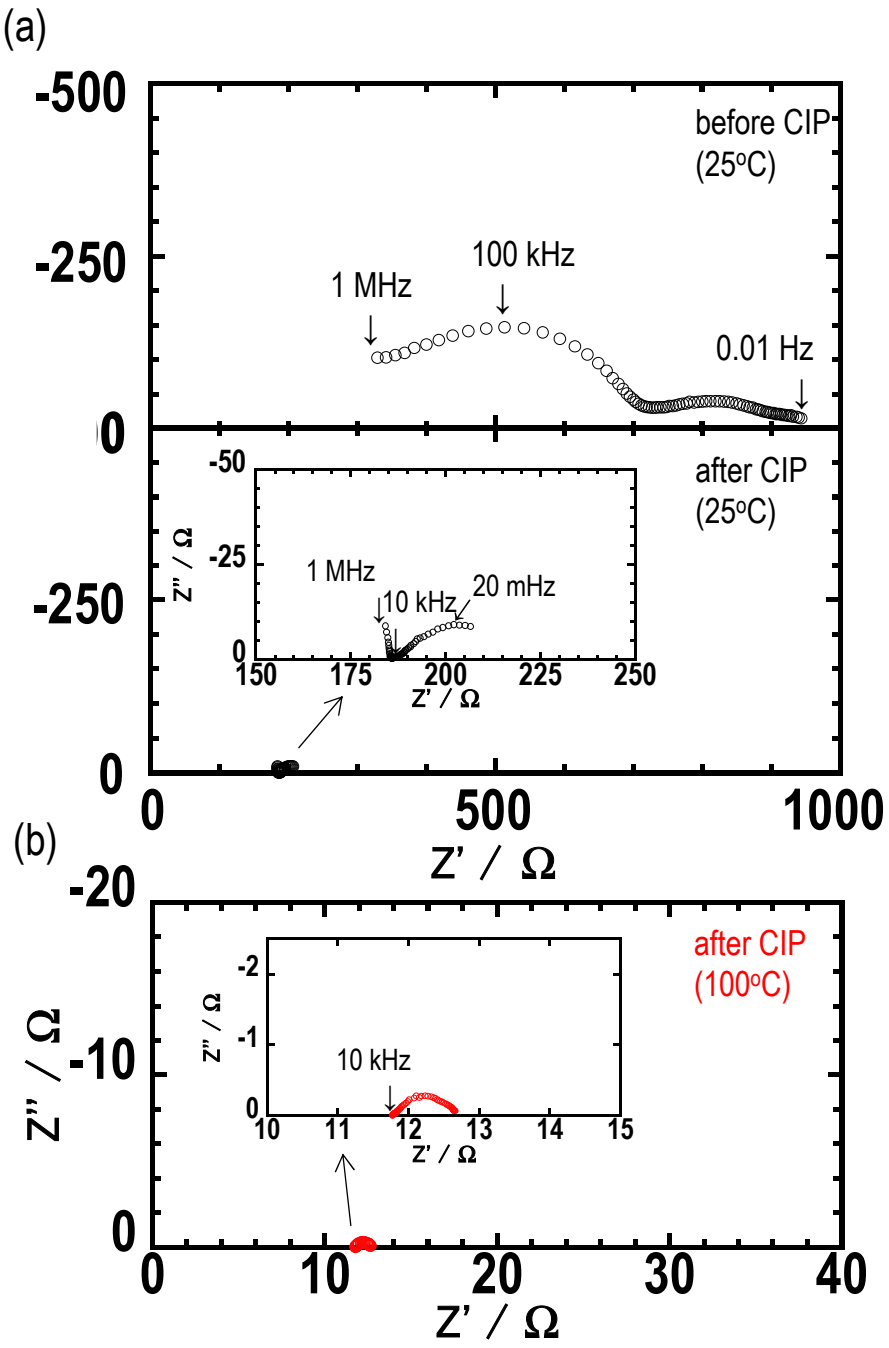

Fig. 3-3-13 Impedance plots of Li/Li_3PS_4/Li cells (a) at 25°C before and after CIP, and (b) at 100°C after CIP.

frequency of 100 Hz is observed before CIP, which is probably attributable to the interfacial resistance between the Li metal and the Li_3PS_4 electrolytes. A region with a higher frequency would be attributable to the resistance for the separator layer of Li_3PS_4 electrolytes. After CIP treatments, the interfacial resistance drastically decreased. This means that interfaces with a large contact area between the Li metal and the Li_3PS_4 electrolytes were achieved by CIP. An interfacial resistance between the Li metal and the garnet-type $Li_7La_3Zr_2O_{12}$ electrolytes decreased by interface modification with metals or metal oxides [6,8–12,30–32]. On the other hand, the resistance of the Li/Li_3PS_4 interface easily decreased by pressing without any interface modification. Impedance plots of Li/Li_3PS_4/Li cells after CIP at 100°C are shown in Fig. 3-3-13 (b). The resistance of the cell became much smaller than that at 25°C.

Figure 3-3-14 (a) shows the results of galvanostatic cycling tests of Li/Li_3PS_4/Li cells at 25°C and 100°C. Galvanostatic cycling tests were performed for 1 and/or 5 h at a constant current density. The applied current densities and areal capacities are also shown in Fig. 3-3-14. Although the cell potential of Li/Li_3PS_4/Li cells suddenly dropped during cycling at 0.38 mA cm^{-2} at 25°C, a stable cell potential was obtained at a higher current density of 0.51 mA cm^{-2} with larger areal capacities of 2.5 mAh cm^{-2} at 100°C. The author indicated in the previous section that obvious morphology changes of Li metal can be observed using Li thin films prepared by vacuum evaporation. Symmetric cells were thus fabricated using Li thin films instead of Li foils. After the galvanostatic tests at 0.064 mA cm^{-2} for 4 h at 25°C and 100°C, the morphology changes after Li deposition was observed by SEM (Fig. 3-3-15). The islands of Li metal were partially deposited after the test at 25°C. On the other hand, the uniform deposition of Li metal was observed after the test at 100°C. These results suggest that increasing the operation temperature of the cell contributes to the more uniform deposition of the Li metal.

Figure 3-3-14 (b) shows the result of the galvanostatic cycling test for the cell with Au thin films at 100°C. Galvanostatic cycling tests started from 0.51 mA cm^{-2} to 1.8 mA cm^{-2} and their time were set for 1 and 5 h at a constant current density. The cell potential was stable up to 1.3 mA cm^{-2} for 5 h, corresponding to 6.5 mAh cm^{-2} of the areal capacity. A calculated

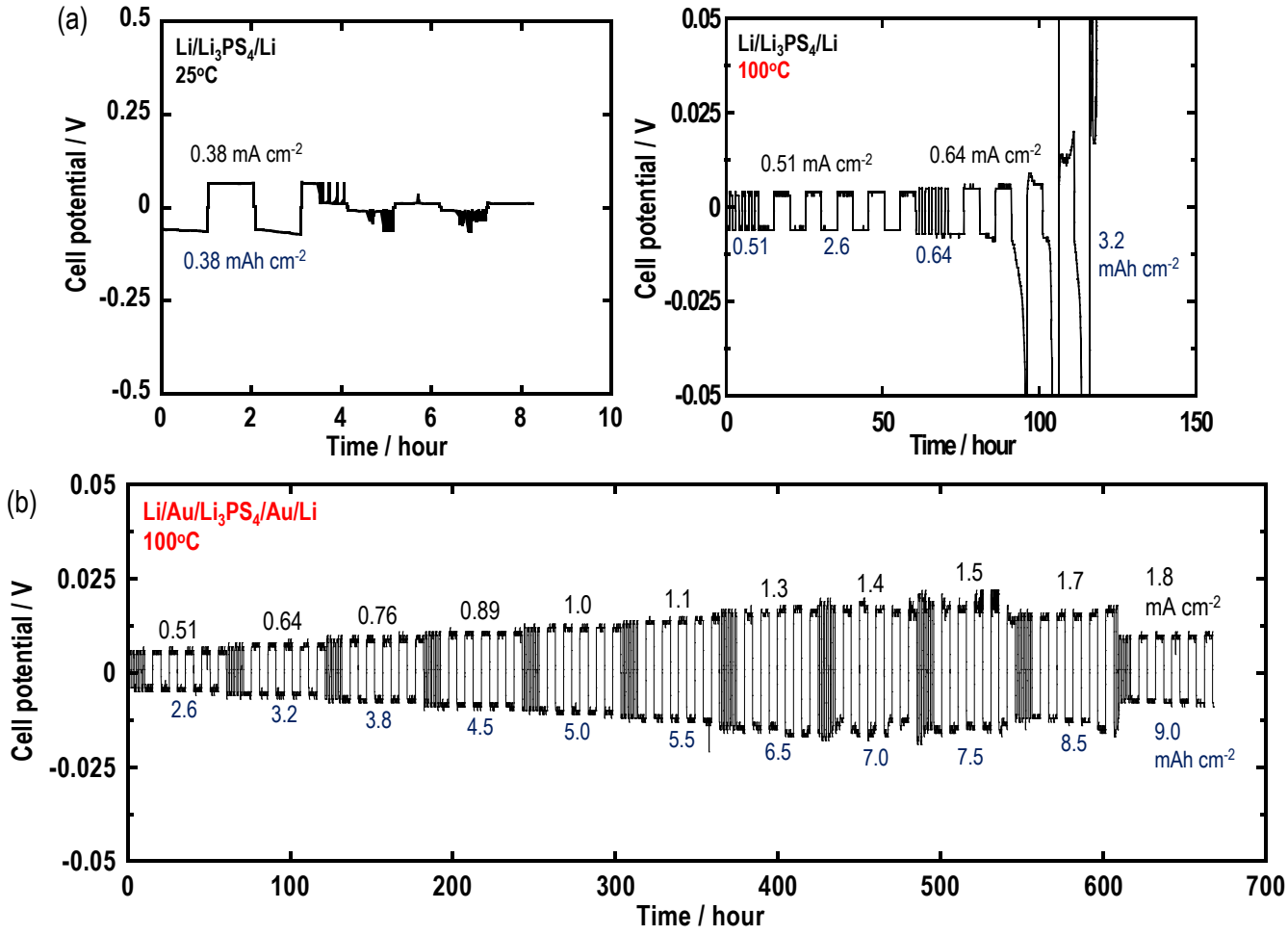

Fig. 3-3-14 (a) Galvanostatic cycling tests of $Li/Li_3PS_4/Li$ cells at 25°C and 100°C. (b) Galvanostatic cycling tests of $Li/Au/Li_3PS_4/Au/Li$ cells at 100°C. The applied current densities (black letters) and areal capacities (blue letters) are shown in the figure.

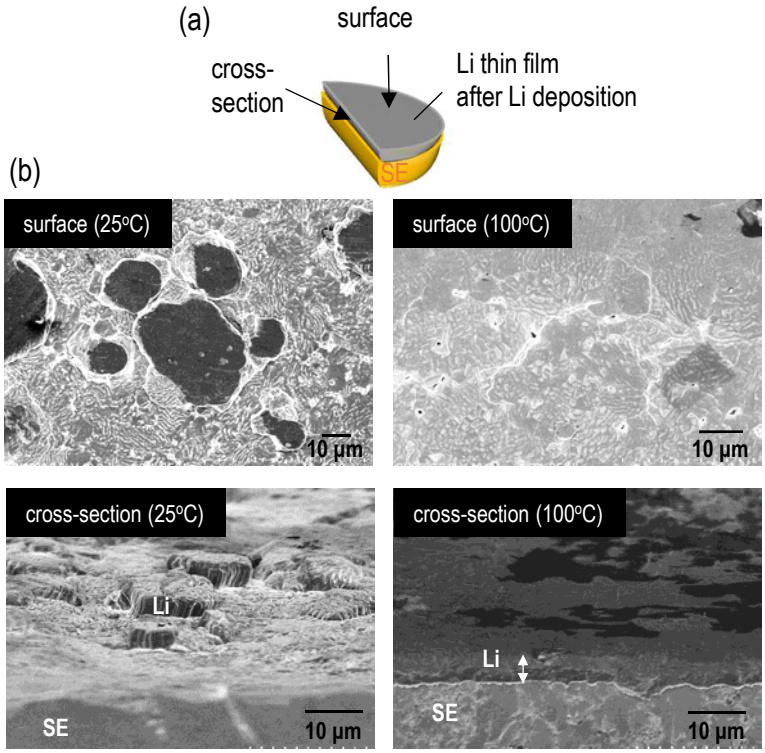

Fig. 3-3-15 Galvanostatic tests were performed for Li/Li_3PS_4/Li cells using Li thin films at 25°C and 100°C (0.064 mA cm^{-2}, 0.26 mAh cm^{-2}). The thickness of the Li thin films before the tests was about 3-4 μm. Morphology changes of Li metal were observed after Li deposition. (a) A schematic diagram of the cell for SEM observation. (b) SEM images of surface and cross-section of the cells after Li deposition.

thickness change of Li metal from the areal capacity is about 31 μm. Li dissolution/deposition performance at 100°C was significantly enhanced by inserting Au thin films between the Li metal and the Li_3PS_4 glass electrolytes. The electrochemical performance for the cell with Au thin films was compared with previous all-solid-state Li symmetric cells using sulfide and garnet-type solid electrolytes in Table 3-3-2 [4,6,8,10–12,14,33–49]. The symmetric cell using Li_3PS_4 glass with Au thin films operating at 100°C exhibited the highest current density with the largest areal capacity.

Figure 3-3-16 shows the cross-sectional back scattered electron image of the interface between the Li metal and the Li_3PS_4 electrolytes for the Li/Au/Li_3PS_4/Au/Li cells after the galvanostatic cycling test at 100°C. Although a partial area of the interface displayed the Au signal (Fig. 3-3-17), it was hardly observed in most of the area of the interface. One possible reason is that Au dissolved in Li metal at 100°C. The composition of Au is about 1 wt% calculated from the amounts of the Li foil and the Au thin film, which is probably a sufficiently low content of Au for it to dissolve in Li metal [22]. This assumption agrees with the disappearance of Au at the interface between Li metal and Li_3PS_4 electrolytes after the galvanostatic cycling test at 100°C in Fig. 3-3-15. Galvanostatic cycling tests were conducted at 25°C for two cells: one was the as-assembled Li/Au/Li_3PS_4/Au/Li cell after CIP and the other was the cell after storage at 100°C for one day (Fig. 3-3-18). The rapid increase of the cell potential was observed for the as-assembled cells. On the other hand, a stable cell potential was obtained for the cell after storage at 100°C. It is considered that Au-dissolved Li metal contributes to enhancing the Li dissolution/deposition performance.

A medium-dark region was observed between the Li metal and the Li_3PS_4 electrolytes in Fig. 3-3-16, which is probably attributable to an area of reduced electrolytes such as Li_2S and Li_3P [15]. The area of the reduced electrolytes may have a negative influence on the electrochemical performance of the cell. However, it is noted that the cell potential of Li/Au/Li_3PS_4/Au/Li cells at 100°C increased little over 400 h in Fig. 3-3-14 (b), suggesting that the influence of the reduction of Li_3PS_4 electrolytes on the cell resistance is small.

Very recently, Fu *et al.* have reported that Mg coating on garnet-type $Li_7La_3Zr_2O_{12}$

Table 3-3-2 Comparison of electrochemical performance of Li dissolution/deposition in all-solid-state Li symmetric cells using sulfide and garnet-type solid electrolytes

Electrolyte	Current density /mA cm^{-2}	Areal Capacity /mAh cm^{-2}	Cycle number	Temperature /°C	Ref.
Li_3PS_4 glass	0.2	0.1	15	25	[33]
$80Li_2S \cdot 20P_2S_5$ glass-ceramic	0.064	0.192	5	25	[4]
$75Li_2S \cdot 24P_2S_5 \cdot 1P_2O_5$ glass-ceramics	0.1	0.125	42	25	[34]
$60Li_2S \cdot 20P_2S_5 \cdot 20LiI$ glass ceramics	0.1	0.1	75	25	[35]
β-Li_3PS_4	0.1	0.2	20	25	[36]
β-Li_3PS_4	0.1	0.2	20	80	[36]
β-Li_3PS_4	0.75	1.5	24	r.t.	[37]
$Li_7P_2S_8I$	0.2	0.2	800	r.t.	[38]
β-Li_3PS_4+$Li_7La_3Zr_2O_{12}$ composite	0.1	0.2	>100	25	[39]
β-Li_3PS_4+$Li_6ZnNb_4O_{14}$ composite	0.1	0.1	400	r.t.	[40]
$Li_{3.334}Ge_{0.334}As_{0.666}S_4$+$LiBH_4$-LiI coating	0.1	0.1	10	25	[41]
$Li_{3.833}Sn_{0.833}As_{0.166}S_4$+$LiBH_4$-LiI coating	0.1	0.1	10	r.t.	[42]
$77.5Li_2S \cdot 22.5P_2S_5$ glass ceramics+polyimine composite	0.5	1	20	60	[43]
Li_3PS_4 glass+Au thin film	1.3	6.5	5	100	This work
$Li_7La_3Zr_2O_{12}$ (Al-substituted)	0.046	0.092	20	r.t.	[44]
$Li_7La_3Zr_2O_{12}$ (Al-substituted)	0.049	0.098	5	25	[45]
$Li_7La_3Zr_2O_{12}$ (Al-substituted)	0.2	0.4	100	r.t.	[46]
$Li_7La_3Zr_2O_{12}$ (Ta-substituted)	0.1	0.41	10	25	[14]
$Li_7La_3Zr_2O_{12}$ (Ta-substituted)	0.1	0.25	12	60	[47]
$Li_7La_3Zr_2O_{12}$ (Ta-substituted)	0.3	0.15	5	25	[48]
$Li_7La_3Zr_2O_{12}$ (Ta-substituted)	0.5	0.25	5	25	[49]
$Li_7La_3Zr_2O_{12}$ (Ta-substituted)+Au coating	0.08	0.16	35	25	[6]
$Li_7La_3Zr_2O_{12}$ (Ta-substituted)+Au coating	0.25	0.5	35	50	[6]
$Li_7La_3Zr_2O_{12}$ (Nb,Ca-substituted)+Si coating	0.2	0.017	75	r.t.	[8]
$Li_7La_3Zr_2O_{12}$ (Nb,Ca-substituted)+Al_2O_3 coating	0.2	0.1	90	r.t.	[11]
$Li_7La_3Zr_2O_{12}$ (Nb,Ca-substituted)+ZnO coating	0.1	0.017	140	r.t.	[12]
$Li_7La_3Zr_2O_{12}$ (Nb,Ca-substituted)+Al coating	0.2	0.017	42	r.t.	[10]

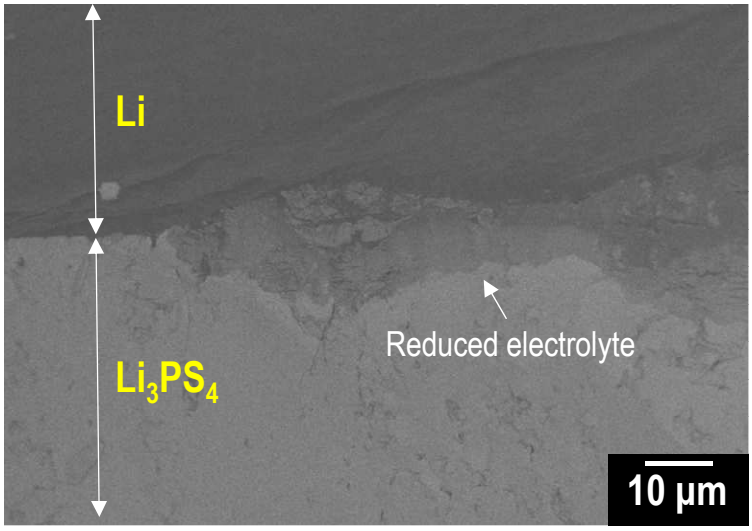

Fig. 3-3-16 Cross-sectional back scattered electron image of the interface between Li metal and Li_3PS_4 solid electrolytes for Li/Au/Li_3PS_4/Au/Li cells after the galvanostatic cycling test at 100°C.

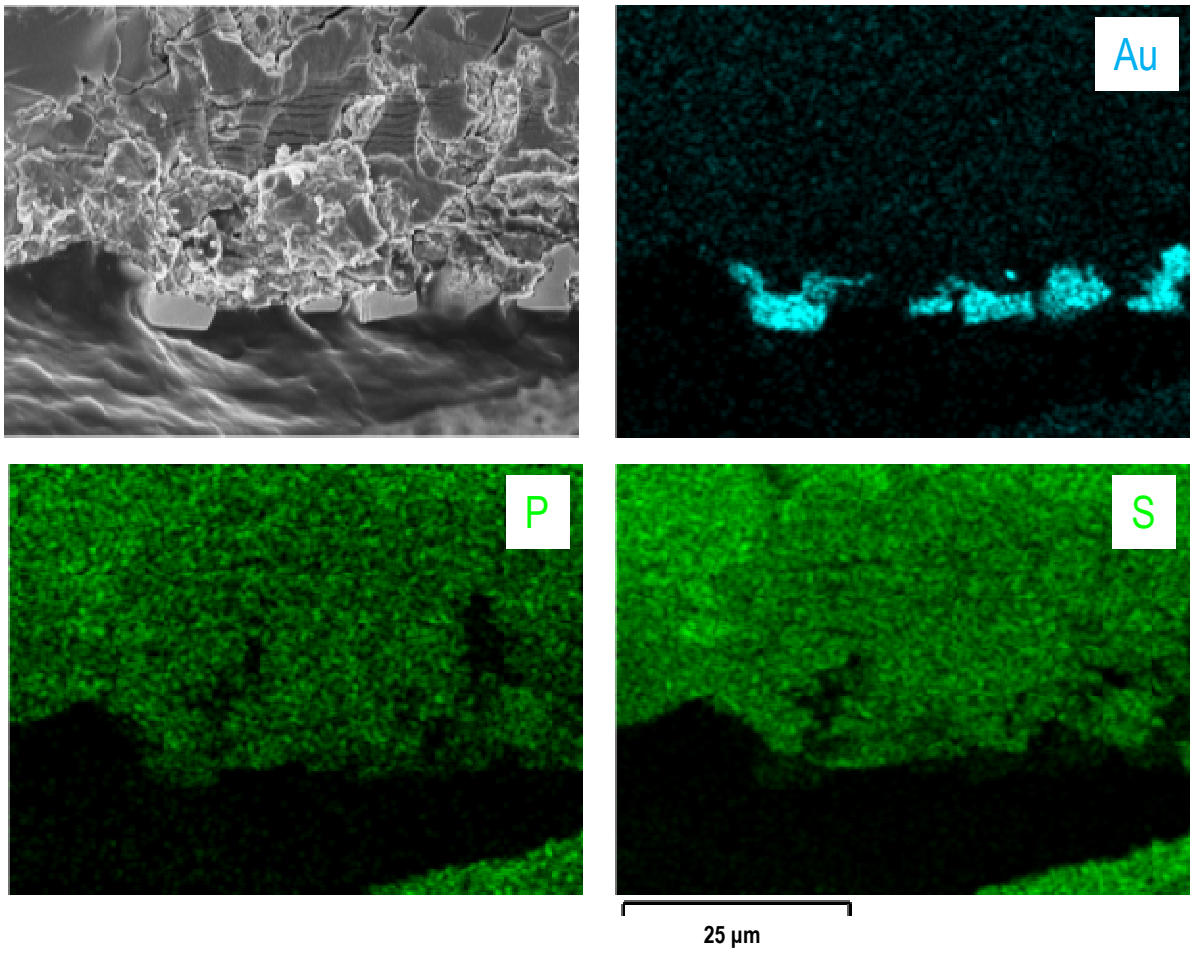

Fig. 3-3-17 Cross-sectional images and EDX mapping of the interface between Li metal and Li_3PS_4 solid electrolytes for Li/Au/Li_3PS_4/Au/Li cells after galvanostatic cycling tests at 100°C. The observation area is different from that shown in Fig. 3-3-15.

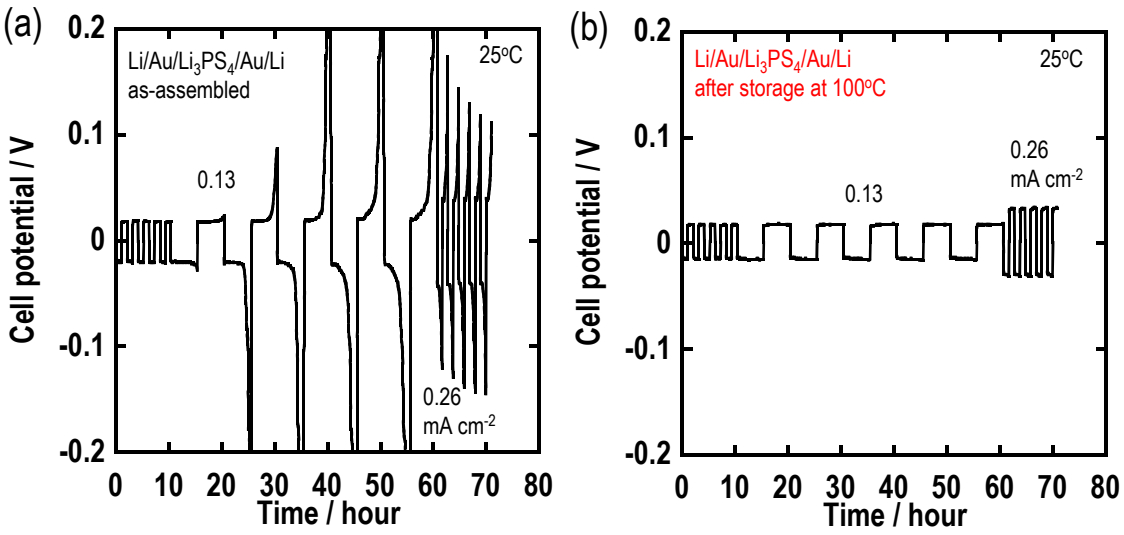

Fig. 3-3-18 Galvanostatic cycling tests of Li/Au/Li_3PS_4/Au/Li cells at 25°C (a) as-assembled and (b) after storage at 100°C for one day.

electrolytes causes dissolution and diffusion in Li metal when it comes into contact with molten Li, which in turn leads to a decrease in the interfacial resistance between Li metal and garnet-type solid electrolytes [32]. Figure 3-3-19 shows the impedance plots of Li/Au/Li_3PS_4/Au/Li cells after CIP and after storage at 100°C for one day. An impedance plot of the Au/Li_3PS_4/Au cell is also shown for comparison. After the attachment of Li foils by CIP, no interfacial resistance with a characteristic frequency about 100 kHz was observed. The impedance plot of the Li/Au/Li_3PS_4/Au/Li cells after CIP was almost similar to that of the cell without the insertion of Au thin films, as shown in Fig. 3-3-13 (a). In addition, the interfacial resistance did not change after storage at 100°C for one day, although the resistance of the separator layer with the higher characteristic frequency decreased slightly. These results indicated that the interfacial resistance between Li metal and Li_3PS_4 glass electrolytes hardly changes by the insertion of metal thin films, unlike the case of garnet-type $Li_7La_3Zr_2O_{12}$ electrolytes.

The author demonstrated the high-temperature performance of all-solid-state Li metal cells with the insertion of Au thin films by using $Li_{1/3}Ni_{1/3}Mn_{1/3}Co_{1/3}O$ (NMC) as a positive electrode. Figure 3-3-20 shows charge-discharge curves, rate performance, and cycle performance of Li/Li_3PS_4/NMC cells with and without Au insertion at 100°C. The loading of NMC in Fig. 3-3-20 is about 7 mg. The efficiency of the NMC cell without Au insertion was degraded at more than 1.9 mA cm^{-2}. On the other hand, the NMC cell with Au insertion exhibited higher rate performance up to 2.4 mA cm^{-2}. The cycle performance was evaluated for the cells after the rate performance tests. The NMC cell with Au insertion displayed excellent cycle performance over 200 cycles, at 1.3 mA cm^{-2}. The average coulomb efficiency was retained at >99% during cycling. In addition, the NMC cell with Au insertion was evaluated by increasing the loading of NMC. The loading of NMC is 45.5 mg, and the loading amounts of components in the cell are summarized in Table 3-3-3. Charge-discharge curves of the NMC cell at 0.13 mA cm^{-2} at 100°C are shown in Fig. 3-3-21. The obtained cell capacity is 7.5 mAh, and thus, the capacity per cell weight is 61 mAh g^{-1}. The capacity is normalized by the total weight of the composite positive electrode (65 mg), Li metal negative electrode

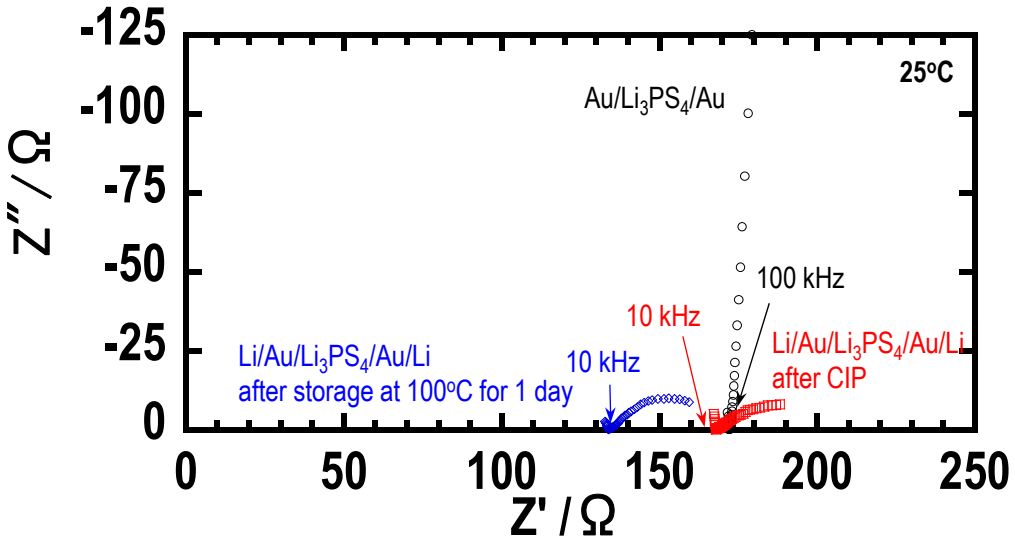

Fig. 3-3-19 Impedance plots of Li/Au/Li_3PS_4/Au/Li cells after CIP and after storage at 100°C for one day. The impedance plot of Au/Li_3PS_4/Au cell is shown for the comparison. All of the measurements were carried out at 25°C.

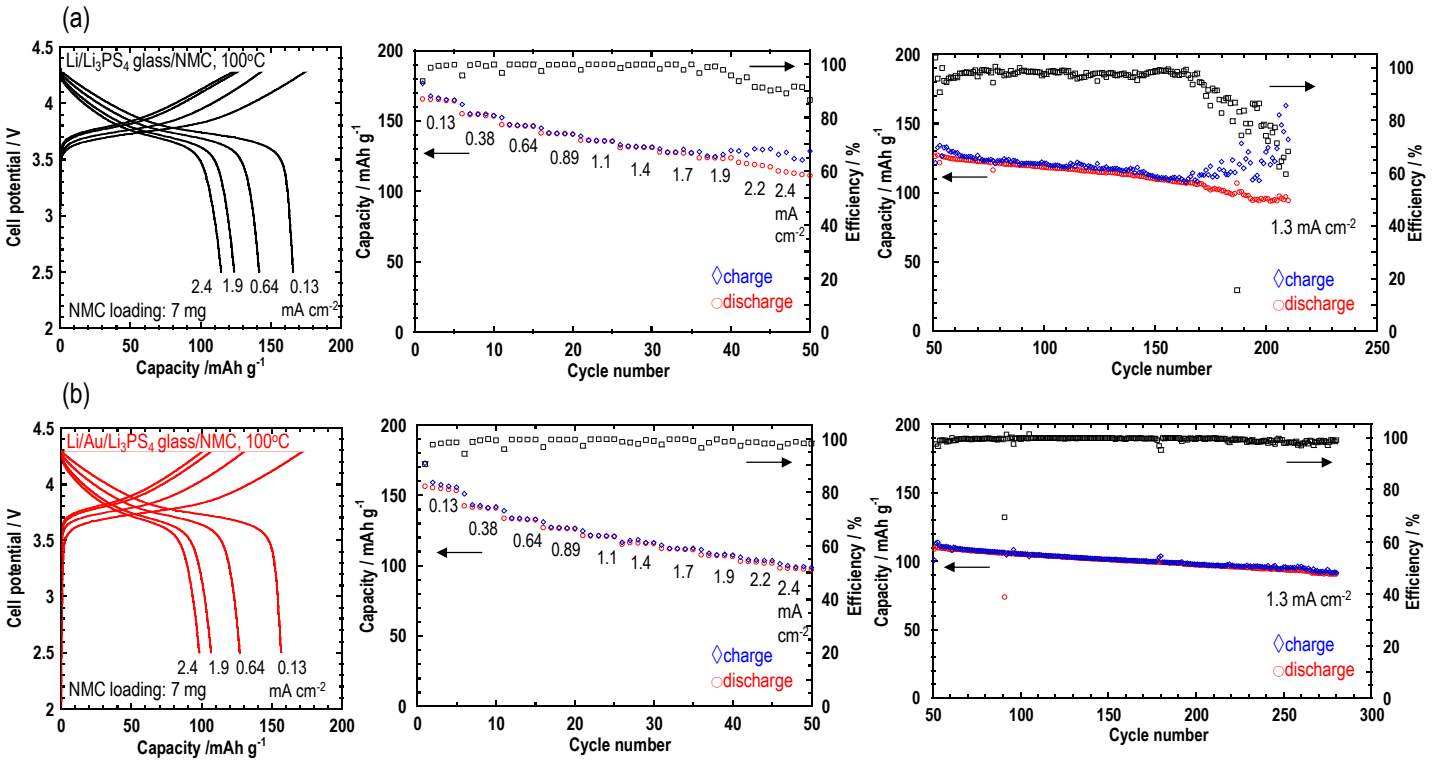

Fig. 3-3-20 Charge-discharge curves, rate performance, and cycle performance at 100°C of all-solid-state cells (a) $Li/Li_3PS_4/NMC$ and (b) $Li/Au/Li_3PS_4/NMC$ cells.

Table 3-3-3 Loading amounts of components in the Li/Au/Li_3PS_4/NMC cell with a large loading of NMC

	Total loading / mg	Material	Loading / mg	Specific capacity / mAh g^{-1}	Areal capacity / mAh cm^{-2}
Composite positive electrode	65	NMC	45.5	164	9.51
		SE(Li_3PS_4)	19.5	-	-
Separator layer	50	SE(Li_3PS_4)	50	-	-
Negative electrode	8.5	Li metal	8.5	3861	41.8

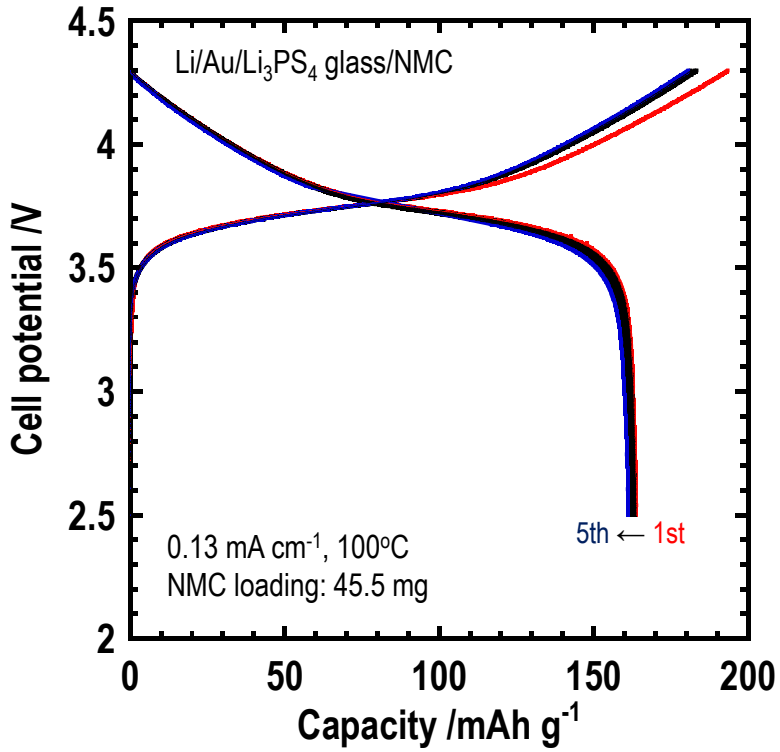

Fig. 3-3-21 Charge-discharge curves of $Li/Au/Li_3PS_4/NMC$ cells at 0.13 mA cm^{-2} at 100°C. The composite positive electrode (65 mg), Li metal negative electrode (8.5 mg), and a separator layer of solid electrolytes (50 mg) were used in the cell.

separator layer of solid electrolytes (50 mg) without a package and current collectors. The energy density is calculated to 226 Wh kg^{-1} based on the average cell potential of 3.7 V, which is comparable to present energy density of lithium-ion batteries. Note that the present energy density of lithium-ion batteries is calculated from the total weight with a package or current collectors. Although further improvements for the cell are needed for practical applications, this result shows a potential use of all-solid-state Li metal batteries. It is noteworthy that electrochemical performance of the all-solid-state Li metal is enhanced by optimizing the interface modification and operation temperatures.

2.4. Summary

In this chapter, interface formation between Li metal and Li_3PS_4 solid electrolytes was investigated for the design of the interfaces suppressing generation of Li dendrites. Bulk-type cells were fabricated using thin Li films prepared by vacuum-evaporation in order to evaluate ideal interfaces with a large contact area between Li metal and Li_3PS_4 solid electrolytes. Symmetric cells with only Li thin films showed a high utilization of Li metal (about 40%) at the initial cycle, though abrupt decrease of utilization was observed and the utilization was about 3% at the 5^{th} cycle. The effects of the insertion modification with Au thin films on Li dissolution and deposition properties were investigated. A high utilization of Li metal (about 25%) was retained for 5 cycles by inserting the Au thin film at the interface between Li metal and Li_3PS_4 solid electrolytes. XPS analysis and SEM observation for Li/Li_3PS_4 and Li/Au/Li_3PS_4 interfaces elucidated the differences with and without the Au film between Li metal and Li_3PS_4 electrolytes. The Au film at Li/Li_3PS_4 interface became Li-Au alloy. The Li-Au alloy layer partially reduced Li_3PS_4 electrolytes as almost the same with Li metal (cf. Li-Au alloy potential: 0.1- 0.3 V vs. Li^+/Li). The author also demonstrated that the reduced product layer has a low resistance and remarkable stability. Furthermore, the impedance measurements and the SEM observation of the interfaces revealed that the Li-Au alloy layer prevents void generation during Li dissolution and functions as the sites for Li deposition. It is suggested that the Li-Au alloy layer at the interface brought about more uniform morphology

change of Li metal and improves the reversibility of Li utilization.

The high-temperature performance of all-solid-state Li metal cells was investigated at 100°C. The resistance of symmetric cells with the Li/Li_3PS_4/Li configuration drastically decreased upon increasing the operating temperature from 25°C to 100°C. In addition, the Li dissolution/deposition performance was improved at 100°C. The effects of inserting a Au thin film between Li metal and Li_3PS_4 electrolytes was also investigated at 100°C. The symmetric cell with the Au thin film functioned without short-circuiting at a higher current density (1.3 mA cm^{-2}), with a larger areal capacity (6.5 mAh cm^{-2}), as compared to the all-solid-state Li metal cells reported so far. It is suggested that the Au-dissolved Li metal electrode contributed to an enhancement in the Li dissolution/deposition performance at 100°C. The Li/Li_3PS_4/$LiNi_{1/3}Mn_{1/3}Co_{1/3}O_2$ (NMC) cells with the Au thin film exhibited high rate performance at 2.4 mA cm^{-2} and stable cycle performance over 200 cycles. An energy density of 226 Wh kg^{-1} was also obtained for the NMC cell with Au insertion. Excellent high-temperature performance was achieved in all-solid-state Li metal batteries with sulfide solid electrolytes. These results indicate a potential use of all-solid-state Li metal batteries.

2.5. Reference

[1] M. Tatsumisago, A. Hayashi, *Int. J. Appl. Glas. Sci.* **5** (2014) 226–235.

[2] A. Manthiram, X. Yu, S. Wang, *Nat. Rev. Mater.* **2** (2017) 16103.

[3] K. Kerman, A. Luntz, V. Viswanathan, Y. M. Chiang, Z. Chen, *J. Electrochem. Soc.* **164** (2017) A1731–A1744.

[4] M. Nagao, A. Hayashi, M. Tatsumisago, *Electrochem. Commun.* **22** (2012) 177–180.

[5] M. Nagao, A. Hayashi, M. Tatsumisago, *Electrochemistry*. **80** (2012) 734–736.

[6] C. L. Tsai, V. Roddatis, C. V. Chandran, Q. Ma, S. Uhlenbruck, M. Bram, P. Heitjans, O. Guillon, *ACS Appl. Mater. Interfaces*. **8** (2016) 10617–10626.

[7] K. Park, B. C. Yu, J.W. Jung, Y. Li, W. Zhou, H. Gao, S. Son, J. B. Goodenough, *Chem. Mater.* **28** (2016) 8051–8059.

[8] W. Luo, Y. Gong, Y. Zhu, K. K. Fu, J. Dai, S. D. Lacey, C. Wang, B. Liu, X. Han, Y. Mo, E. D. Wachsman, L. Hu, *J. Am. Chem. Soc.* **138** (2016) 12258–12262.

[9] W. Luo, Y. Gong, Y. Zhu, Y. Li, Y. Yao, Y. Zhang, K. K. Fu, G. Pastel, C. F. Lin, Y. Mo, E. D. Wachsman, L. Hu, *Adv. Mater.* **29** (2017) 1–7.

[10] K. K. Fu, Y. Gong, B. Liu, Y. Zhu, S. Xu, Y. Yao, W. Luo, C. Wang, S. D. Lacey, J. Dai, Y. Chen, Y. Mo, E. Wachsman, L. Hu, *Sci. Adv.* **3** (2017) e1601659.

[11] X. Han, Y. Gong, K. K. Fu, X. He, G. T. Hitz, J. Dai, A. Pearse, B. Liu, H. Wang, G. Rubloff, Y. Mo, V. Thangadurai, E. D. Wachsman, L. Hu, *Nat. Mater.* **16** (2016) 572–579.

[12] C. Wang, Y. Gong, B. Liu, K. Fu, Y. Yao, E. Hitz, Y. Li, J. Dai, S. Xu, W. Luo, E. D. Wachsman, L. Hu, *Nano Lett.* **17** (2017) 565–571.

[13] A. Sharafi, H. M. Meyer, J. Nanda, J. Wolfenstine, J. Sakamoto, *J. Power Sources*. **302** (2016) 135–139.

[14] F. Yonemoto, A. Nishimura, M. Motoyama, N. Tsuchimine, S. Kobayashi, Y. Iriyama, *J. Power Sources*. **343** (2017) 207–215.

[15] Y. Zhu, X. He, Y. Mo, *ACS Appl. Mater. Interfaces*. **7** (2015) 23685–23693.

[16] A. Hayashi, S. Hama, H. Morimoto, M. Tatsumisago, T. Minami, *J. Am. Ceram. Soc.*

84 (2001) 477–479.

[17] Y. Wang, T. Matsuyama, M. Deguchi, A. Hayashi, A. Nakao, M. Tatsumisago, *J. Ceram. Soc. Japan*. **124** (2016) 597–601.

[18] B. Wang, J. B. Bates, F. X. Hart, B. C. Soles, R. A. Zuhr, J. D. Robertson, *J. Electrochem. Soc.* **143** (1996) 3203.

[19] J. B. Bates, G. R. Gruzalski, N. J. Dudney, C. F. Luck, X. Yu, *Solid State Ionics*. **70**–**71** (1994) 619–628.

[20] K. Kanehori, K. Matsumoto, K. Miyauchi, T. Kudo, *Solid State Ionics*. **9**–**10** (1983) 1445–1448.

[21] S. D. Jones, J. R. Akridge, **434** (1993) 505–513.

[22] A. D. Pelton, *Bull. Alloy Phase Diagrams*. **7** (1986) 228–231.

[23] M. Fantauzzi, B. Elsener, D. Atzei, A. Rigoldi, A. Rossi, *RSC Adv.* **5** (2015) 75953–75963.

[24] S. Wenzel, D.A. Weber, T. Leichtweiss, M. R. Busche, J. Sann, J. Janek, *Solid State Ionics*. **286** (2016) 24–33.

[25] S. Wenzel, S. Randau, T. Leichtweiß, D. A. Weber, J. Sann, W. G. Zeier, J. Janek, *Chem. Mater.* **28** (2016) 2400–2407.

[26] T. Hakari, A. Hayashi, M. Tatsumisago, *Chem. Lett.* **44** (2015) 1664–1666.

[27] G. Nazri, *Solid State Ionics*. **34** (1989) 97–102.

[28] A. N. Dey, *J. Electrochem. Soc.* **118** (1971) 1547.

[29] M. Hiratani, K. Miyauchi, T. Kudo, *Solid State Ionics*. **28**–**30** (1988) 1406–1410.

[30] Y. Li, B. Xu, H. Xu, H. Duan, X. Lü, S. Xin, W. Zhou, L. Xue, G. Fu, A. Manthiram, J.B. Goodenough, *Angew. Chemie - Int. Ed.* **56** (2017) 753–756.

[31] J. Wakasugi, H. Munakata, K. Kanamura, *J. Electrochem. Soc.* **164** (2017) A1022–A1025.

[32] K. K. Fu, Y. Gong, Z. Fu, H. Xie, Y. Yao, B. Liu, M. Carter, E. Wachsman, L. Hu, *Angew. Chemie - Int. Ed.* **56** (2017) 14942–14947.

[33] T. Yamada, S. Ito, R. Omoda, T. Watanabe, Y. Aihara, M. Agostini, U. Ulissi, J.

Hassoun, B. Scrosati, *J. Electrochem. Soc.* **162** (2015) A646–A651.

[34] Y. Tao, S. Chen, D. Liu, G. Peng, X. Yao, X. Xu, *J. Electrochem. Soc.* **163** (2016) A96–A101.

[35] S. Choi, S. Lee, J. Yu, C. H. Doh, Y. C. Ha, *ECS Trans.* **77** (2017) 65–70.

[36] Z. Liu, W. Fu, E. A. Payzant, X. Yu, Z. Wu, N. J. Dudney, J. Kiggans, K. Hong, A. J. Rondinone, C. Liang, *J. Am. Chem. Soc.* **135** (2013) 975–978.

[37] H. Wang, Z. D. Hood, Y. Xia, C. Liang, *J. Mater. Chem. A.* **4** (2016) 8091–8096.

[38] E. Rangasamy, Z. Liu, M. Gobet, K. Pilar, G. Sahu, W. Zhou, H. Wu, S. Greenbaum, C. Liang, *J. Am. Chem. Soc.* **137** (2015) 1384–1387.

[39] E. Rangasamy, G. Sahu, J. K. Keum, A. J. Rondinone, N. J. Dudney, C. Liang, *J. Mater. Chem. A.* **2** (2014) 4111–4116.

[40] Z. D. Hood, H. Wang, Y. Li, A. S. Pandian, M. Parans Paranthaman, C. Liang, *Solid State Ionics*. **283** (2015) 75–80.

[41] G. Sahu, E. Rangasamy, J. Li, Y. Chen, K. An, N. Dudney, C. Liang, *J. Mater. Chem. A.* **2** (2014) 10396.

[42] G. Sahu, Z. Lin, J. Li, Z. Liu, N. Dudney, C. Liang, *Energy Environ. Sci.* **7** (2014) 1053.

[43] J. M. Whiteley, S. Hafner, C. Zhu, W. Zhang, S. H. Lee, *J. Electrochem. Soc.* **164** (2017) A2962–A2966.

[44] L. Cheng, W. Chen, M. Kunz, K. Persson, N. Tamura, G. Chen, M. Doeff, *ACS Appl. Mater. Interfaces*. **7** (2015) 2073–2081.

[45] M. Botros, R. Djenadic, O. Clemens, M. Möller, H. Hahn, *J. Power Sources*. **309** (2016) 108–115.

[46] A. Sharafi, E. Kazyak, A.L. Davis, S. Yu, T. Thompson, D. J. Siegel, N. P. Dasgupta, J. Sakamoto, *Chem. Mater.* **29** (2017) 7961–7968.

[47] B. Xu, W. Li, H. Duan, H. Wang, Y. Guo, H. Li, H. Liu, *J. Power Sources*. **354** (2017) 68–73.

[48] R. H. Basappa, T. Ito, H. Yamada, *J. Electrochem. Soc.* **164** (2017) A666–A671.

[49] R. H. Basappa, T. Ito, T. Morimura, R. Bekarevich, K. Mitsuishi, H. Yamada, *J. Power Sources*. **363** (2017) 145–152.

4. General conclusions

This thesis focuses on two approaches for the development of all-solid-state Li metal batteries with high energy density. One is the research for solid electrolytes with the mechanical properties capable of preventing the growth of Li dendrites. The other is the design of interface formation between Li metal and solid electrolytes in order to suppress the generation of Li dendrites. This thesis mainly discussed Li_2S-P_2S_5-based sulfide glass electrolytes as a potential solid electrolyte for Li metal batteries.

The following results and considerations were obtained.

1. Elastic moduli and formability of Li_2S-P_2S_5 glasses were evaluated. Young's moduli of Li_2S-P_2S_5 glasses increased with an increase in the Li_2S content. Adding Li_2S transformed their local structure to an isolated structure by breaking P-S-P bonds in the glass network. It is suggested that the more isolated structure increased the ion packing density and led to an increase of the Young's moduli. In addition, $75Li_2S \cdot 25P_2S_5$ (mol%) glasses composed of Li^+ and PS_4^{3-} ions, which is the most isolated structure in Li_2S-P_2S_5 glasses, exhibited better densification by pressure.

2. Difference in formability between Li_2S-P_2S_5 glasses, glass-ceramics, and crystals synthesized by solid phase reactions were evaluated. The glasses showed higher densification with few grain boundaries than the crystalline ones because of the isotropic structure with the free volume. The few grain boundaries in the glass are critical for the use of Li metal negative electrodes because Li dendrites are likely to propagate through the grain boundaries.

3. Mechanical properties of Li_2S-P_2S_5-LiX (X = I, Br, and Cl) glass electrolytes were investigated. The Young's moduli of the glass electrolytes were found to decrease upon the addition of lithium halides. In particular, LiI addition to the $75Li_2S \cdot 25P_2S_5$ glass gradually

decreased its Young's modulus from 23 GPa to 19 GPa. The electrical conductivities of Li_2S-P_2S_5 glasses increased upon the addition of lithium halides. At the same time, both lower elastic moduli and higher ionic conductivities could be obtained. The performance of the all-solid-state cells using Si composite electrodes was compared with $75Li_2S \cdot 25P_2S_5$ and $70(0.50Li_2S \cdot 0.50P_2S_5) \cdot 30LiI$ glass electrolytes, which exhibited similar electrical conductivities but different Young's moduli. The cell with $70(0.50Li_2S \cdot 0.50P_2S_5) \cdot 30LiI$ glass electrolytes, which exhibited lower Young's moduli, exhibited larger capacities over 20 cycles. Therefore, it can be concluded that Li_2S-P_2S_5-LiI glasses with superior mechanical properties, such as lower Young's modulus and better formability, would exhibit better cell performance. Li metal negative electrodes also exhibited a large volume change during the dissolution and deposition reactions. It is expected to suppress the dendrite growth using the glass electrolytes with the lower elastic modulus.

4. Young's moduli of element substituted Li_2S-P_2S_5 glasses were evaluated and compared with oxide and other chalcogenide glasses. The Young's moduli of the Li_2S-P_2S_5 glasses increased when replacing the glass former of P_2S_5 with GeS_2 or SiS_2. The Young's moduli also increased by substituting S with O. In addition, the elastic moduli of Li_2S-P_2S_5 glasses where Li_2S is fully replaced by other sulfide-modifiers of Na_2S, Ag_2S, SnS, and MgS were investigated. The Young's moduli of these glasses increased with an increase in the content of each modifier. Young's moduli studied here were summarized from the viewpoint of the mean atomic volumes. A good correlation between Young's moduli and mean atomic volumes was found in the sulfide glasses as well as oxide and other chalcogenide glasses.

5. Formability of these sulfide glasses was investigated on the basis of the relative density of the powder-compressed pellets at 360 MPa. The formability of the Li_2S-P_2S_5 glasses is better than that of the Li_2S-SiS_2 and Li_2S-GeS_2 glasses. Moreover, it is suggested that the cation field strength of glass modifiers is related to the formability. Pugh's ratio

(*B*/*G*) was used to evaluate ductile-brittle properties of materials. The glass with a larger *B*/*G* ratio, meaning higher ductility, tended to display a higher relative density. It is noteworthy that plastic deformation affected the densification of sulfide glasses due to their lower bonding energy, larger free volume, and more isolated structure.

6. Bulk-type cells were fabricated using thin Li films prepared by vacuum-evaporation in order to evaluate ideal interfaces with a large contact area between Li metal and Li_3PS_4 solid electrolytes. Symmetric cells with only Li thin films showed a high utilization of Li metal (about 40%) at the initial cycle, though abrupt decrease of utilization was observed and the utilization is about 3% at the 5^{th} cycle. The effects of the insertion modification with Au thin films on Li dissolution and deposition properties were investigated. A high utilization of Li metal (about 25%) was retained for 5 cycles by inserting the Au thin film at the interface between Li metal and Li_3PS_4 solid electrolytes.

7. XPS analysis and SEM observation for Li/Li_3PS_4 and Li/Au/Li_3PS_4 interfaces elucidated the differences with and without the Au film between Li metal and Li_3PS_4 electrolytes. The Au film at Li/Li_3PS_4 interface became Li-Au alloy. The Li-Au alloy layer partially reduced Li_3PS_4 electrolytes as almost the same with Li metal (cf. Li-Au alloy potential: 0.1- 0.3 V vs. Li^+/Li). We also demonstrated that the reduced product layer had a low resistance and remarkable stability. Furthermore, the impedance measurements and the SEM observation of the interfaces revealed that the Li-Au alloy layer prevented void generation during Li dissolution and functioned as the sites for Li deposition. It is suggested that the Li-Au alloy layer at the interface brought about more uniform morphology change of Li metal and improved the reversibility of Li utilization.

8. The high-temperature performance of all-solid-state Li metal cells was investigated at 100°C. The resistance of symmetric cells with the Li/Li_3PS_4/Li configuration drastically decreased upon increasing the operating temperature from 25°C to 100°C. In addition, the

Li dissolution/deposition performance was improved at 100°C. The effects of inserting a Au thin film between Li metal and Li_3PS_4 electrolytes was also investigated at 100°C. The symmetric cell with the Au thin film functioned without short-circuiting at a higher current density (1.3 mA cm^{-2}), with a larger areal capacity (6.5 mAh cm^{-2}), as compared to the all-solid-state Li metal cells reported so far. It is suggested that the Au-dissolved Li metal electrode contributed to an enhancement in the Li dissolution/deposition performance at 100°C. The $Li/Li_3PS_4/LiNi_{1/3}Mn_{1/3}Co_{1/3}O_2$ (NMC) cells with the Au thin film exhibited high rate performance at 2.4 mA cm^{-2} and stable cycle performance over 200 cycles. An energy density of 226 Wh kg^{-1} was also obtained for the NMC cell with Au insertion. Excellent high-temperature performance was achieved in all-solid-state Li metal batteries with sulfide solid electrolytes. These results indicate a potential use of all-solid-state Li metal batteries.

Acknowledgements

I would like to show my greatest appreciation to Professor Masahiro Tatsumisago of Osaka Prefecture University for his useful direction, suggestion, discussion and continuous encouragement during the course of this work.

I would like to express my gratitude to Professor Hiroshi Inoue and Professor Akitoshi Hayashi for their valuable suggestion and helpful comments to this thesis. In particular, I am pleased that I could study under Professor Hayashi for six years.

I am immensely grateful for valuable suggestions, discussions and assistance from Assistant Professor Atsushi Sakuda of Osaka Prefecture University throughout the project. Furthermore, I am fortunate to have had valuable advices towards this research from Emeritus Professor Tsutomu Minami of Osaka Prefecture University, Professor Kiyoharu Tadanaga of Hokkaido University, Professor Nobuya Machida of Konan University, Professor Atsunori Matsuda of Toyohashi University of Technology, and Professor Yoshiyuki Kowada of Hyogo University of Teacher Education.

Furthermore, I am deeply grateful to thank all of undergraduate students, graduate students, and researchers in Laboratory of Inorganic Chemistry at Osaka Prefecture University, especially Dr. Motohiro Nagao, Dr. Keigo Aso, Dr. Takuya Matsuyama, Mr. Kousuke Noi, Dr. Yusuke Ito, Dr. Naoto Tanibata, Dr. Takashi Hakari, Mr. Ryohei Takano, Mr. Yoshiaki Hibi, Mr. Kosuke Tsuda, Ms. Mirai Yamamoto, Mr. Kenji Nagao, Mr. So Yubuchi, Mr. Masashi Nose, Ms. Misae Otoyama, Mr. Takamasa Asano, Ms. Fumika Tsuji, Mr. Masaaki Fujita, Mr. Motoshi Suyama, Mr. Takuya Kimura, Ms. Minako Deguchi, Ms. Hiroe Kowada, and Ms. Chie Hotehama for their useful discussion and support to this research.

Finally, I want to thank my parents. Without their long-term support and considerable encouragement, this thesis would not have been possible.

List of Publications

Original articles regarding this study are as follows:

1. "Evaluation of young's modulus of Li_2S-P_2S_5-P_2O_5 oxysulfide glass solid electrolytes"
   A. Kato, M. Nagao, A. Sakuda, A. Hayashi, and M. Tatsumisago,
   J. Ceram. Soc. Jpn., **122** (2014) 552-555. (Chapter 2)

2. "Evaluation of mechanical properties of Na_2S-P_2S_5 sulfide glass electrolytes"
   M. Nose, A. Kato, A. Sakuda, A. Hayashi, and M. Tatsumisago,
   J. Mater. Chem. A, **3** (2015) 22061-22065. (Chapter 2)

3. "Mechanical properties of Li_2S-P_2S_5 glasses with lithium halides and application in all-solid-state batteries"
   A. Kato, M. Yamamoto, A. Sakuda, A. Hayashi, and M. Tatsumisago,
   J. ACS Appl. Energy Mater., accepted. (Chapter 2)

4. "Mechanical properties of sulfide glasses in all-solid-state batteries"
   A. Kato, M. Nose, M. Yamamoto, A. Sakuda, A. Hayashi, and M. Tatsumisago,
   J. Ceram. Soc. Jpn., submitted. (Chapter 2)

5. "Enhancing utilization of lithium metal electrodes in all-solid-state batteries by interface modification with gold thin films"
   A. Kato, A. Hayashi, and M. Tatsumisago,
   J. Power Sources, **309** (2016) 27-32. (Chapter 3)

6. “XPS and SEM analysis between Li/Li_3PS_4 interface with Au thin film for all-solid-state lithium batteries”

   A. Kato, H. Kowada, M. Deguchi, C. Hotehama, A. Hayashi, and M. Tatsumisago,

   Solid State Ionics, submitted. (Chapter 3)

7. “High temperature performance of all-solid-state lithium metal batteries with Li/Li_3PS_4 interfaces modified by Au thin films”

   A. Kato, M. Suyama, H. Kowada, C. Hotehama, A. Sakuda, A. Hayashi,

   and M. Tatsumisago,

   J. Electrochem. Soc., submitted. (Chapter 3)